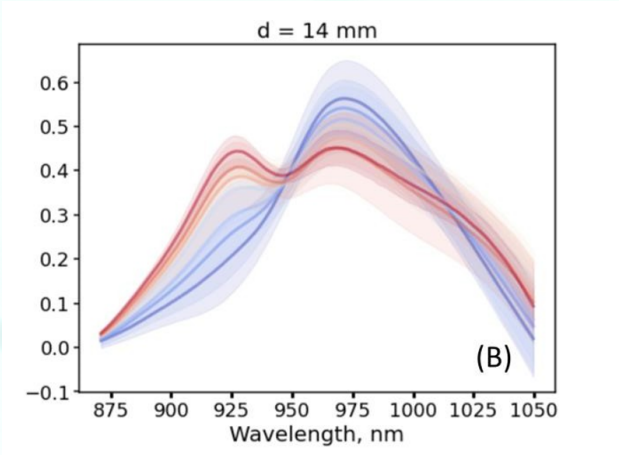
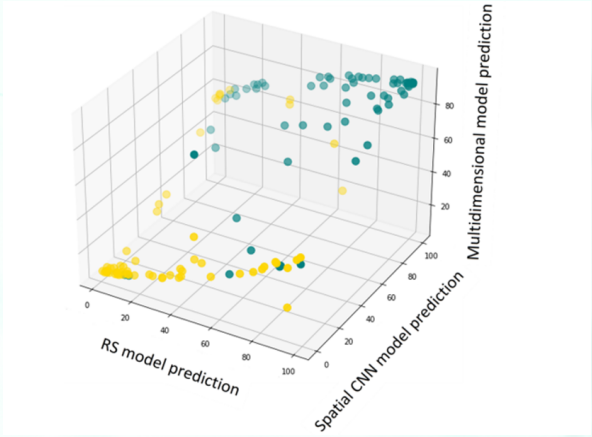
Volume 10 | Issue 1 |2024

Journal
of Biomedical Photonics & Engineering





Editor-In-Chief:
Valery Tuchin

©2024 J-BPE

Journal of Biomedical Photonics & Engineering

by Samara National Research University

Volume 10, Issue 1 (March 2024)

Editor-In-Chief

Valery V. Tuchin − Saratov National Research State University, Russian Federation;
Institute of Precision Mechanics and Control RAS, Russian Federation; a corr.-member of RAS

Deputy Editor-In-Chief

Valery P. Zakharov − Samara National Research University, Russian Federation

Postal address:
39B Lukacheva st., room #301
Samara 443086, Russian Federation

Used Figures from this issue on the Cover

Denis A. Davydov et al., Exploring the Relationship between Hypodermis Thickness and Diffuse Reflectance Spectra in Different Age and Gender Groups, 010303, Fig. 2(B).

Irina A. Matveeva et al., Multidimensional Analysis of Dermoscopic Images and Spectral Information for the Diagnosis of Skin Tumors, 010307, Fig. 6(a).

© 2024 J-BPE

Contents

Articles

Human blood plasma SERS analysis using silver nanoparticles for cardiovascular diseases detection 010301
Sahar Z. Al-Sammarraie, Lyudmila A. Bratchenko, Elena N. Tupikova, Maria A. Skuratova, Shuang Wang, Peter A. Lebedev, and Ivan A. Bratchenko

Exploring Convolutional Neural Networks for the Classification of Acute Lymphoblast Leukemia Blood Cell Images 010302
Andrey Trubnikov and Dmitry Savelyev

Exploring the Relationship between Hypodermis Thickness and Diffuse Reflectance Spectra in Different Age and Gender Groups 010303
Denis A. Davydov, Nikolay A. Fadeev, Ivan D. Filippov, and Gleb S. Budylin

Highly Accurate EEG Signal Classification Using Multiple Feature Extraction and LSTM Networks 010304
Deshmukh Deepika and Gillala Rekha

The Implications of Varying Batch-Size in the Classification of Patch-Based Lung Nodules Using Convolutional Neural Network Architecture on Computed Tomography Images 010305
Bushara A. R., Vinod Kumar R. S., and Kumar S. S.

Photobiomodulation at 660 nm Modifies Apoptosis Regulators Bcl-2 and Caspase-3 in Diabetic Wounded Cell Models in Vitro 010306
Sandy Winfield Jere and Nicolette Nadene Houreld

Multidimensional Analysis of Dermoscopic Images and Spectral Information for the Diagnosis of Skin Tumors 010307
Irina A. Matveeva, Andrey I. Komlev, Oleg I. Kaganov, Alexander A. Moryatov, and Valery P. Zakharov

Improving the Detection of Blood on Poultry Meat Based Colorimetry Using a Camera 010308
Koekoeh Santoso, Hadri Latif, La Jumadin, and Putri Gusfani Wida

The Assessment of Photo-Induced Toxicity of [$NaYF_4$:Yb^{3+}, Er^{3+}] Upconversion Nanoparticles on Model Normal and Cancer Cell Lines *in Vitro* 010309
Irina Yu. Yanina, Roman A. Verkhovskii, Nikita A. Navolokin, and Vyacheslav I. Kochubey

 © 2024 J-BPE

Human blood plasma SERS analysis using silver nanoparticles for cardiovascular diseases detection

Sahar Z. Al-Sammarraie[1*], Lyudmila A. Bratchenko[1], Elena N. Tupikova[1], Maria A. Skuratova[2], Shuang Wang[3], Peter A. Lebedev[4], and Ivan A. Bratchenko[1]

[1] Samara National Research University, 34 Moskovskoe Shosse, Samara 443086, Russia
[2] Samara City Clinical Hospital №1 named after N.I. Pirogov, 80 Polevaya str., Samara 443096, Russia
[3] Northwest University, #1 Xuefu Avenue, Xi'an 710127, Shaanxi, China
[4] Samara State Medical University, 159 Tashkentskaya str., Samara 443095, Russia

***e-mail:** saharzead@rocketmail.com

Abstract. In recent years, the use of Raman and surface enhanced Raman spectroscopy for disease detection has grown. The motives for their increased use have commonly been attributed to their well-known benefits, such as the creation of narrow spectral bands that are characteristic of the molecular components present, and high sensitivity and specificity that they can provide. The aim of this work is the analysis of spectral features of plasma in patients with cardiovascular diseases utilizing surface enhanced Raman spectroscopy to determine the presence or absence of the disease. The investigation revealed spectrum difference between the patient and healthy volunteers' groups at the observed Raman bands. 146 patients and 67 healthy subjects were analyzed. Classification of the patient group with cardiovascular diseases was made based on the projection on latent structures with 99% accuracy. Stability of the classifier was checked with the implementation of cross-validation and separation of analyzed data into training and test sets. The obtained results demonstrate that the proposed SERS technique is stable and has significant potential in clinical diagnostic applications. © 2024 Journal of Biomedical Photonics & Engineering.

Keywords: surface-enhanced Raman spectroscopy; Enhancement Factor; blood serum, blood plasma; silver nanoparticles; Raman band shift.

Paper #9010 received 20 Aug 2023; revised manuscript received 8 Nov 2023; accepted for publication 8 Nov 2023; published online 16 Jan 2024. doi: 10.18287/JBPE24.10.010301.

1 Introduction

Cardiovascular diseases (CVDs) are the leading cause of death worldwide, in 2019, cardiovascular disease, primarily coronary and cerebrovascular atherosclerosis still caused about 18 million deaths pear year worldwide (> 30% of all deaths). Coronary heart disease, cerebrovascular disease, rheumatic heart disease, and other illnesses are among the category of heart and blood vessel disorders known as CVDs [1–3]. A range of auxiliary examination methods, both invasive (such as selective coronary angiography) and non-invasive (such as nuclear scans, CT, stress tests, and blood biomarkers), allow assessment of cardiovascular disease risk and treatment targets. However, there is no simple blood biochemical index or biological target for the diagnosis of atherosclerosis at present; instead, more ultrasonographic screening or angiography are used [4, 5].

In latest years, surface-enhanced Raman scattering (SERS) spectroscopy has been increasingly used with the aim of developing diagnostic applications. SERS is a commonly used sensing technique in which inelastic light scattering by molecules is greatly enhanced when the molecules are absorbed onto corrugated metal surfaces. The high sensitivity, the ease of use and the increasing availability of relatively inexpensive portable Raman instruments, make SERS particularly attractive for the development of point-of-care and screening tests of biological samples, such as blood derivatives or tissues [6, 7]. The SERS effect is currently being debated

in the literature and two mechanisms have been identified: the electromagnetic mechanism and the chemical mechanism [8]. The first suggests the stimulation of localized surface plasmons on the metallic surface, whereas the second suggests a chemical process for the creation of charge-transfer complexes between the metallic surface and analyte species. Given their sensitivity in the examination of biological material, Raman spectroscopy and SERS have recently been employed as a useful tool in clinical diagnostics and biomedical research [8], including DNA (Pyrak et al., and Zhang et al. [9, 10]), RNA (Lee et al., Han et al. [11, 12]), cancer markers (Choi et al. [13]), bacteria (Andrei et al. [14]), viruses (Chen et al. [15]), genes (Vo-Dinh et al. [16]), drugs (Jaworska et al. [17]), pathological markers on cellular membranes and tissues (Wallace and Masson [18]), other biomolecules, ion concentrations, and redox potential in cells (Jaworska et al. [19]), and even *in vivo* SERS measurements on mice (Wen et al. [20]).

In the current study, a simple approach of SERS substrate implementation for blood plasma/ serum analysis is considered. Blood plasma and serum are biofluids that are widely utilized as diagnostic samples because they are rich in biochemical and biological information, are easily accessible, and may be obtained non-invasively. They are routinely preserved in biobanks for research purposes for the same reasons. Regardless of the potential diagnostic capabilities of SERS analysis of blood components, just a few researches have been conducted using it [6, 21].

In order to make SERS trustworthy for the investigation of biofluids, analytical procedures and spectrum interpretation still need to be established. The manufacture and development of SERS substrates that are repeatable, stable, effective, and fairly priced is another significant barrier to the reliable use of SERS in diagnostics [22, 23]. It was found that the cheapest and most efficient substrates were aqueous dispersion of Ag and Au nanoparticles (metal colloids) [24, 25]. Nanoparticle size, shape, and surface properties affect SERS properties in fact, Zeng et al. [26] recently employed aqueous Au and Ag colloids to evaluate the diagnostic potential of SERS spectroscopy of blood serum and plasma in relation to different diseases. Nanoparticle size, shape, and surface properties affect SERS properties for instance Jianqiang et al. [27] prepared starch-capped gold nanoparticles with hexagon and boot shapes through using a nontoxic and biologically benign aqueous-phase synthetic route. They found that different-shaped gold nanoparticles possess different SERS properties. Tian et al. [28] synthesized and characterized gold nanospheres and their aggregates, nanotriangles, and nanostars of similar dimensions according to their average size, zeta potential and UV/visible absorption and explored their relative efficiencies for SERS.

Despite the outstanding signal enhancements accomplished by metal colloids and their simple preparation and use, some substrates frequently struggle with a lack of consistency due to various preparing protocols, and depending on the preparation methods; the nanoparticles have various physico-chemical surface characteristics, resulting in different stability, SERS efficiency, and repeatability [29].

Thus, the main objective of our work is to develop a useful tool for early, stable and accurate diagnosis of CVDs patients based on SERS analysis of blood plasma. The implemented method utilizes a classification model based on projection on latent structures (PLS) to identify CVD patients, and determining the most informative SERS bands associated with differences between the CVD group and control group by variable importance in projection (VIP) distribution.

2 Materials and Methods

2.1 Colloidal Silver Nanoparticles Solution

Silver nitrate and trisodium citrate were used as starting materials for the preparation of (AgNPs). The silver colloid was prepared by using chemical reduction method. All solutions of reacting materials were prepared in distilled water. In typical experiment 20 ml of distilled water heated to boil. To this solution 3 ml of 1.8% AgNO3 of and 6 ml of 1% trisodium citrate (Na3C6H5O7) were added. The resulting solution was heated at 95 °C for 20 min until a yellow-green solution is formed. Then the solution was removed from the heating device and stirred until cooled to room temperature. The UV-Vis spectrum of the AgNPs solution was obtained by utilizing the Spectrophotometer (UNICO 1201, United Products & Instruments, USA) to track NPs characteristics. Detailed analysis of acquired AgNPs properties may be found elsewhere [30].

2.2 Serum/Plasma Samples Preparation

A standardized sampling was carried out from patients of the Samara Regional Clinical Hospital named after V. D. Seredavin. The study included patients with different cardiovascular diseases. Diagnosis of CVD for each patient was set by doctors in Samara Regional Clinical Hospital named after V. D. Seredavin after examination of patient based on physical test and results of a blood tests according to the guidelines of Russian Ministry of Health. The study protocols were approved by the ethical committee of Samara State Medical University. All the subjects who participated in this study gave their written informed consent at the beginning of the study. The blood plasma samples were collected from patients in fasting condition and placed in sealed containers, followed by freezing at a temperature of –16 °C. Immediately before the start of the analysis, the blood serum/plasma samples were defrosted at room temperature. Each blood plasma samples were dropped in a volume of 1.5 μl and dried for 30 min on aluminum foil with the layer of dried silver colloid for SERS analysis. we measured 1 to 2 specters for each healthy control subjects and 5 to 6 for each patient. The characteristics of the sample of subjects are presented in Table 1.

Table 1 Characteristics of analyzed samples.

Group	Number of patients	Mean age	Number of spectra
Control group	67	33–80 (62)	85
Patients with Cardiovascular Disease	146	40–75 (62)	778

2.3 Experimental Setup and Spectra Collection

The experimental setup for Raman analysis of human serum includes a spectrometric system (EnSpectr R785, Spektr-M, Chernogolovka, Moscow Region, Russia) and a microscope (ADF U300, ADF, China). Focusing the exciting radiation and collecting the scattered radiation were implemented using 50× Objective LMPlan. The stimulation of collected spectra was performed by the laser module with central wavelength 785 nm. The diameter of the laser spot at the focus on the sample surface was 5 μm. The laser power was 10 mW. Exposure time was 4 s. The resulting raw spectrum is an automatic sequential recording of four spectra with subsequent averaging. Thus, the recording time of the SERS raw spectrum is 16 s.

2.4 Spectra Processing

Preprocessing of raw SERS spectra of biofluids consisted of several successive stages: noise smoothing, removal of autofluorescent background, and normalization. Smoothing of the raw spectra was performed with a Savitzky-Golay filter with a filter window width of 15, the first order of the polynomial used for smoothing, and a zero-order derivative (no derivative). Then the smoothed spectra were subjected to the removal of the autofluorescent background by the polynomial method (15th degree polynomial) [31]. Spectral characteristics are normalized using the standard deviation of the method of normal variation (SNV) that consists in subtracting each spectrum by its own mean and dividing it by its own standard deviation. After SNV, each spectrum will have a mean of 0 and a standard deviation of 1.

Each sample of a biofluid corresponds to *a priori* information about belonging to a certain group. Therefore, the data was analyzed through supervised learning. To avoid overfitting, the analysis of the stability of the constructed models and the choice of optimal parameters were implemented using k-fold cross-validation (k = 7) [32]. After cross-validation and determination of the optimal parameters of the model, the complete data set was randomly divided: 80% of the subjects for training the model (training set) and 20% of the subjects for testing the model (testing set). It should be noted that when splitting the initial dataset into a training set and a verification set (both in cross-validation and in the final model construction), the split was performed by subjects in order to avoid allocating the spectral characteristics corresponding to one subject in different sets, which could lead to incorrect overestimation of the model characteristics. Thus, the proposed way of data splitting provides more stable classification models. When building models, the importance of predictors in solving the classification problem was estimated using the distribution of the importance of variables in the constructed model (VIP distribution). An analysis of the VIP distribution makes it possible to determine which spectral bands and related components of the biofluid are characterized by differences in the classification task performed.

Multivariate analysis was implemented using PLS-discriminant analysis (PLS-DA) based on the SIMPLS algorithm in the MDAtools package available in the R studio software.

3 Results and Discussion

Fig. 1 presents the mean plasma SERS spectra with standard deviation (SD) for the control group (healthy) and group of patients with CVD. Fig. 1 demonstrates that the differences between the mean serum spectra for the discriminated groups are visually observed in the intensity of individual spectral bands. Without utilizing multivariate analysis, we can see an increase in the intensity of the peaks at 715 cm^{-1} (C-H) Hypoxanthine, Phosphatidylserine, 856 cm^{-1} (C-O-H) Glutathione), 1003 (C-C) Phenylalanine), 1244 (amide III (proteins)carbohydrates C-O-C, N-H), 1390 cm^{-1} (C-N, C-H group, CH_3, CH_2 wagging (lipids)), can be identified as distinctive features in the spectral characteristics of the plasma of the patient's group against the control group (healthy), in addition it shows a decrease intensity at 494 and 640 cm^{-1} ((S-S) Phosphatidylserine, (C-S) L- tyrosine, lactose) for the patients' group [33, 34].

Spectral bands and SERS characteristics of the plasma obtained in the current study are similar to those reported in the studies. Huang et al. indicated (856, 1005, and 1244 cm^{-1}) among the informative spectral bands associated with the degree of Coronary artery disease (CAD) spectra showed Raman peaks appeared to originate from lipids and proteins which are the major contributors to Small Extracellular vesicles (sEV) surface. In another work Yang et al. indicated (1244 and 1389 cm^{-1}) as the informative spectral bands from patients with Coronary Heart Disease (CHD). However, it should be noted that Huang et al. and Yang et al. [35, 36] reported a SERS band at 1450 cm^{-1} which was very slightly observed in our study; this band was assigned to the CH_2 bending vibration of proteins and lipids.

The analyzed spectral data is characterized by multicollinearity property; thus, application of projection analysis methods can provide a statistically reliable result. The most common approach to solve such problems is the method of discriminant analysis with regression on latent structures – PLS-DA [37]. Discriminant analysis is a technique used to identify the unique features of groups or individuals. The technique assumes that there are common underlying structures in groups or individuals. These common underlying structures are represented by a set of latent variables.

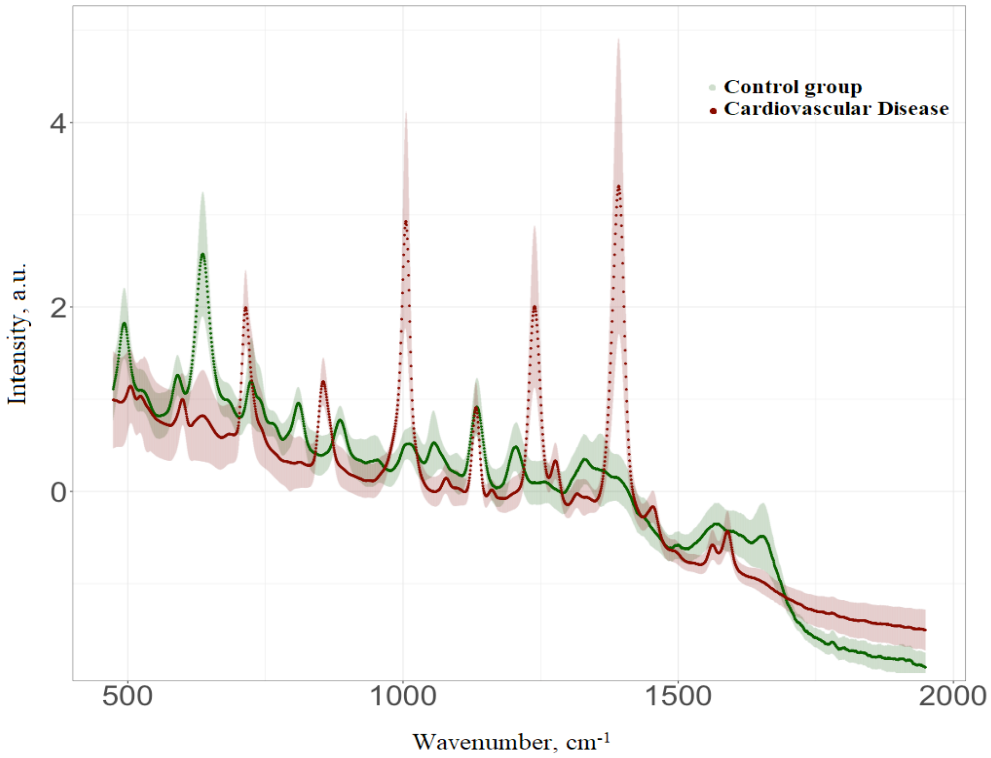


Fig. 1 Mean with standard deviation (SD) for SERS spectra of plasma for control group (healthy) and the patients with (cardiovascular diseases).

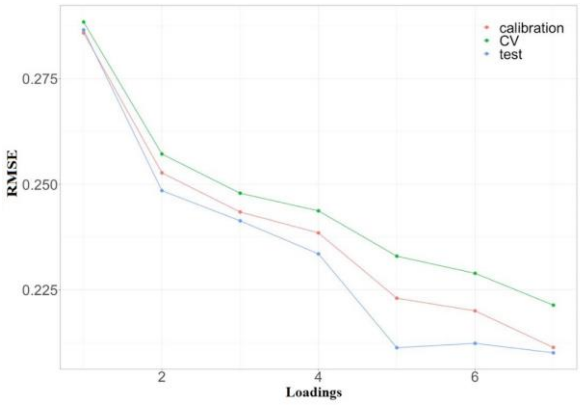


Fig. 2 The relationship between the number of LVs and the root mean square error (RMSE) for PLS-DA model.

To use the SIMPLS algorithm to implement the PLS and PLS portions of the PLS-DA approach [38, 39]. The number of loading vectors (LVs) in the PLS-DA model was determined using training data set through 7 split CV. According to Fig. 2, the RMSE value for the calibration set and CV algorithm is decreasing to 7 LVs. However, in test set RMSE is increasing after LV5, thus, only first 5 LVs were utilized in the analysis.

In order to assess the contribution of each LV we examined their structure. As shown in Fig. 3 LVs peaks show a close correlation with plasma Raman spectra bands at 727, 1003, 1240 and 1390 cm^{-1}, however in the shape of LV4 we observed a negative peak at 1240 and 1375 cm^{-1} but with lower intensity in comparison with the rest LVs. Table 2 demonstrates characteristics of the constructed classification models. Classifying plasma samples of CVD patients and healthy group is possible with the sensitivity, specificity, and accuracy of 100%, 95% and 0.99% respectively. Stability of the model was verified by CV.

Fig. 4 demonstrates the VIP distribution of the SERS matrix of plasma spectra when constructing discrimination models of control group (healthy donors), with patients with (cardiovascular diseases). The VIP distribution is represented by a gradient fill, where the purple color corresponds to the minimum information content, and the yellow – to the maximum information content. It shows the most informative spectral bands when constructing models coincide with the visible differences in the mean spectra of the discriminated groups. The model identified the following spectral bands as the most informative: 727, 1003, 1244, and 1390 cm^{-1}.

In order to evaluate the performance of a binary diagnostic classification method, a ROC curve was employed. It is, represented as a graph, that is used to evaluate the performance of a binary diagnostic classification method. The diagnostic test results need to be classified into one of the clearly defined dichotomous categories, such as the presence or absence of a disease. Higher the score, higher the distinction and lower the crossover of the predictions of the two classes [40]. Fig. 5 shows ROC AUC of CVD classification equaled to 0.99. This result suggests the model is successful to perform the correct classification of CVD.

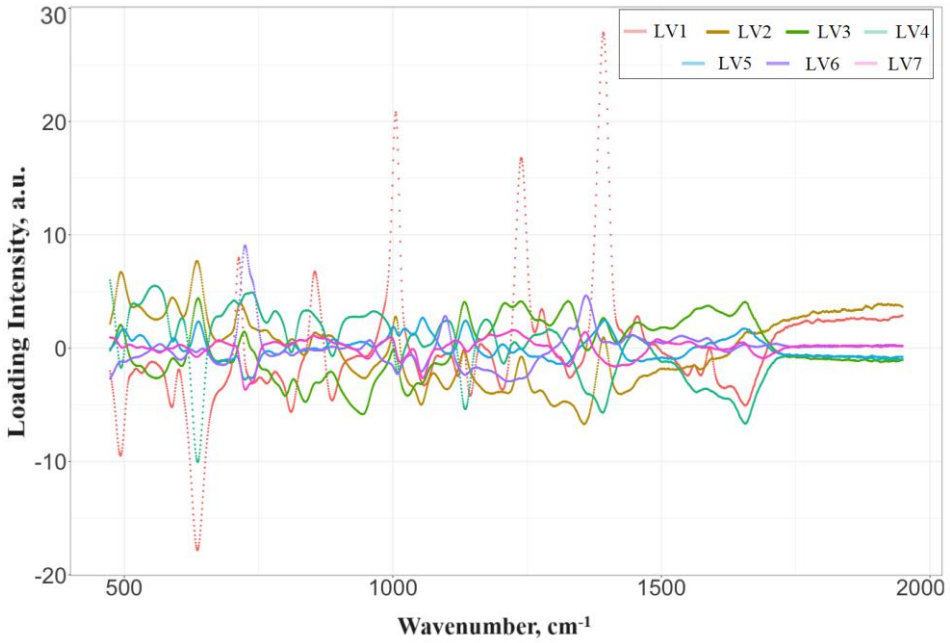


Fig. 3 Shape of the LV1−LV7 for the constructed PLS-DA model.

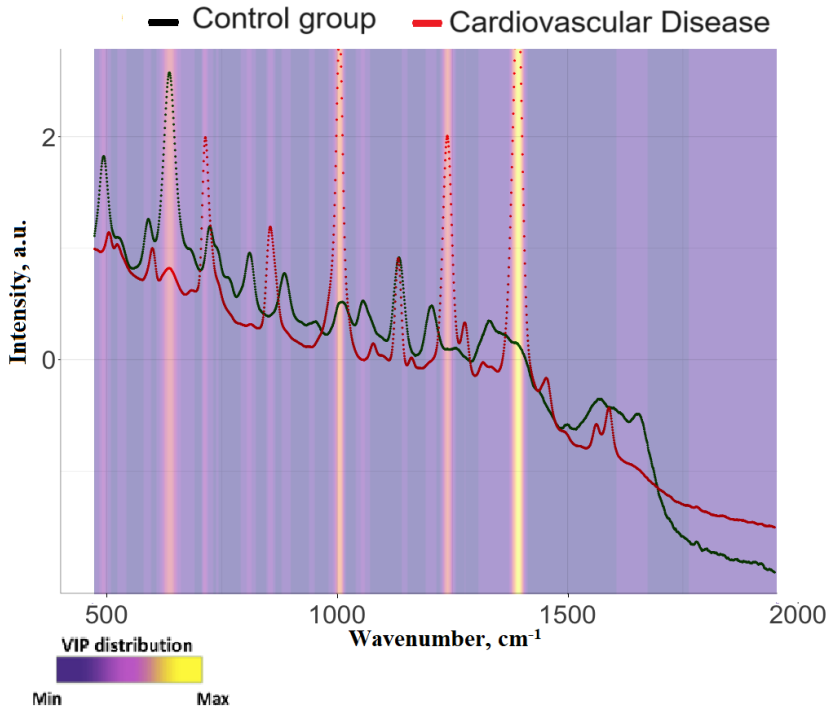


Fig. 4 The mean plasma spectra for the discriminated groups with the overlapping VIP distribution.

Table 3 represent the main informative Raman bands in the discrimination of plasma samples of the control group and the group of patients. One may see that the main contribution to the registered Raman bands with the proposed approach is associated with wide range of chemical groups which can hardly be assumed as markers of CVD. At the same time, it is quite challenging to find an exact biomarker of CVD and instead combinations of biomarkers may be utilized for the efficient detection of CVD [41]. In this regard proposed SERS analysis offers a simple and reliable way to analyze a "spectral landscape" of chemical components of blood (including biomarkers), and further evaluation of such spectral data gives an opportunity to create a classification model of CVD that involves data from multiple biomarkers together at the same time. However, further investigations are required to estimate possible contribution of exact components to classification of CVD. Such analysis may be performed with utilization of deep-learning and artificial intelligence models [42, 43].

Table 2 Characteristics of the PLS-DA Discrimination Model for the Control Group and the Cardiovascular Disease Group presented as "Mean (95% CI)".

Classification	Sensitivity			Specificity			Accuracy		
	train	cross-validation	test	train	cross-validation	test	train	cross-validation	test
Control group (Healthy)	1 (0.99–1)	1 (0.99–1)	1 (0.99–1)	0.95 (0.89–99)	0.96 (0.92–1)	0.95 (0.91–1)	0.95 (0.92–0.97)	0.97 (0.94–0.99)	0.99 (0.96–1)
Cardiovascular Disease group	0.89 (0.86–0.94)	0.89 (0.88–0.92)	0.95 (0.91–1)	1 (0.99–1)	1 (0.99–1)	1 (0.99–1)	0.96 (0.90–98)	0.96 (0.91–0.99)	0.99 (0.97 1)

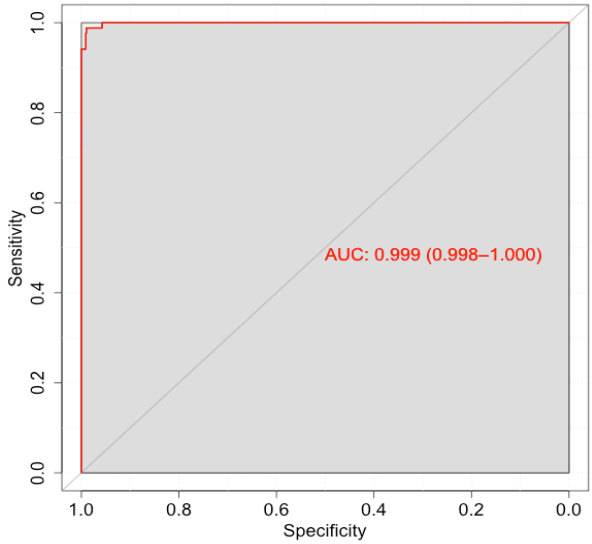


Fig. 5 ROC curves of the constructed models for the classification of "healthy" control group vs "patients" group on the verification dataset.

In contrary to the proposed approach it is possible to analyze exact biomarkers of CVD. As example, Cheng et al. [44] created a SERS-based platform for the ultrasensitive detection of cardiac troponin and creatine kinase-MB by combining a novel SERS nanoprobe with a monoclonal antibody immobilized gold-patterned chip. This SERS platform offers a limit of detection of 8.9 pg/mL and 9.7 pg/mL. Another rapid, cost-effective SERS immunoassay approach developed by Chon et al. [45]. This method was effective in the detection of 42.5 pg/mL and 33.7 pg/mL of creatinine kinase and troponin respectively and the fitted regression line was within the 95% CI. In similar approaches Hu et al. [46] used a magnetic immunoassay technique based on SERS to create a SERS immunoprobe to detect heart-type fatty acid-binding protein and cardiac troponin. The concentration of the biomarkers was determined by observing the distinctive Raman peak intensities of the two Raman reporter molecules. The minimal detection limits of H-FABP and cTnI at the optimal conditions were 0.6396 and 0.0044 ng/mL, respectively. Fu et al. [47] studied the usage of graphene oxide-gold nanoparticle combination for effective signal amplification for troponin detection in another promising SERS lateral immunoassay. As compared to immunoassays lacking graphene oxide, this test was able to detect troponin quantitatively across a much wider range (5 pg/mL to 1000 ng/mL). Application of discussed SERS platforms is effective for exact biomarkers detection (as troponin), but further investigations are required to estimate exact accuracy of CVD detection in clinical settings. In addition to, the discussed approaches are more complex, expensive, and complicated to manufacture in comparison to the proposed technique.

Moreover, we achieved a high diagnostic classification result in comparison to other studies. For instance, in our previous work we analyzed the spectral features of the serum in hemodialysis patients with end-stage chronic kidney disease using a combination of SERS and machine learning methods. The specificity was found to be 0.95, 0.92 sensitivity, and 0.94 accuracy [48]. Huang et al. [35] demonstrated a study for early diagnosis of coronary artery disease detection by isolated small extracellular vesicles analysis from the human plasma samples. The achieved sensitivity, specificity, and accuracy of 97%, 95%, and 92.3% respectively. Yanga et al. [36] measured and analyzed urine samples from congenital heart disease patients, including those who had and had not undergone percutaneous coronary intervention. The authors showed that the two patient groups had classification sensitivity and specificity of 90% and 78.9%, respectively.

Lin et al. [49] studied the variability of different tumor stages in nasopharyngeal cancer in blood plasma using SERS. High diagnostic sensitivities of 84% and 92%, specificities of 83.3% and 95% and accuracies of 83.5% and 93.3%, respectively, were achieved for classification of cancer and normal blood groups. Feng et al. [50] analyzed blood plasma samples from healthy control subjects and patients diagnosed with adenomas and colorectal cancer. The corresponding diagnostic sensitivity, specificity and accuracy were 0.938, 0.869 and 0.945 respectively. Tahir et al. [51] used SERS for analysis of serum samples of late acute stage of typhoid in comparison with healthy samples, accuracy, sensitivity and specificity were 91%, 89%, and 97 %, respectively.

Table 3 Major Raman peak positions and their characteristic assignments [33−36].

Raman shift (cm^{-1})	Peak assignment
641	(C–S) L-tyrosine, lactose
727	(C–H) Hypoxanthine, Phosphatidylserine, amide III
1003	(C–C) Phenylalanine
1244	amide III (proteins)carbohydrates C-O-C, N-H
1390	C-N, C-H group, CH3, CH2 wagging (lipids), Tyrosine (proteins), and nucleic acid, lipoproteins

In general, the presented data shows that the proposed approach of human blood plasma analysis and spectra classification is stable for the detection of patients with CVD. This method offers an opportunity to achieve 99% accuracy and 0.99 ROC AUC of CVD detection, however, further clinical trials are required to ensure that the proposed approach may provide high specificity of CVD detection among other diseases.

4 Conclusions

This study shows that plasma SERS spectra can be a useful resource of information for the noninvasive diagnosis of CVD. In this investigation, 67 plasma samples from healthy volunteers and 146 plasma samples from patients with CVD were analyzed using the 785 nm laser excitation. The investigation revealed spectrum difference between the patient and healthy volunteer groups at the characteristic Raman bands, which can be linked to biochemical changes in blood during CVD progression. The achieved classification accuracy was 99%. SERS substrate based on AgNPs is a useful platform for the intensification of Raman signals of blood plasma, allowing to observe significant differences between analyzed groups.

In comparison to standard diagnostic procedures, the results imply that the proposed approach of blood plasma analysis with SERS has the benefit of being less invasive, fast, and simple to use. Thus, the proposed SERS platform has the potential to be a useful diagnostic tool suitable for clinical detection and monitoring of CVD severity. However, further investigations with the proposed SERS platform are required for better understanding of spectral contributions of chemical components of plasma in patients with CVD. Moreover, combination of SERS serum analysis and skin optical biopsy [52] may be tested in future.

Acknowledgments

This work was funded by the Russian Science Foundation Project No. 21-75-10097, https://rscf.ru/project/21-75-10097/.

Disclosures

The authors declare that they have no conflict of interest.

References

1. R. V. John, T. Devasia, N. Mithun, J. Lukose, and S. Chidangil, "Micro-Raman spectroscopy study of blood samples from myocardial infarction patients," Lasers in Medical Science 37(9), 3451–3460 (2022).
2. R. Ross, "The pathogenesis of atherosclerosis," Nature 362(6423), 801–809 (1993).
3. R. A. Hegele, "The genetic basis of atherosclerosis," International Journal of Clinical and Laboratory Research 27, 2–13 (1997).
4. D. Bennett, R. V. Krishnamurthi, S. Barker-Collo, M. H. Forouzanfar, M. Naghavi, M. Connor, C. M.M. Lawes, A. E. Moran, L. M. Anderson, G. A. Roth, G. A. Mensah, M. Ezzati, C. J. L. Murray, and V. L. Feigin, "The global burden of ischemic stroke: findings of the GBD 2010 study," Global Heart 9(1), 107–112 (2014).
5. A. E. Moran, M. H. Forouzanfar, Gregory A. Roth, George A. Mensah, M. Ezzati, Christopher, J. L. Murray and M. Naghavi, "Temporal trends in ischemic heart disease mortality in 21 world regions, 1980 to 2010: the Global Burden of Disease 2010 study," Circulation 129(14), 1483–1492 (2014).
6. Y. Khristoforova, L. Bratchenko, and I. Bratchenko, "Raman-Based Techniques in Medical Applications for Diagnostic Tasks: A Review," International Journal of Molecular Sciences 24(21), 15605 (2023).
7. Y. Zhang, X. Mi, X. Tan, and R. Xiang, "Recent progress on liquid biopsy analysis using surface-enhanced Raman spectroscopy," Theranostics 9(2), 491(2019).
8. N. Guillot, M. L. de la Chapelle, "The electromagnetic effect in surface enhanced Raman scattering: Enhancement optimization using precisely controlled nanostructures," Journal of Quantitative Spectroscopy and Radiative Transfer 113(18), 2321–2333 (2012).
9. E. Pyrak, J. Krajczewski, A. Kowalik, A. Kudelski, and A. Jaworska, "Surface enhanced Raman spectroscopy for DNA biosensors—How far are we?" Molecules 24(24), 4423 (2019).

10. J. Zhang, Y. Dong, W. Zhu, D. Xie, Y. Zhao, D. Yang, and M. Li, "Ultrasensitive detection of circulating tumor DNA of lung cancer via an enzymatically amplified SERS-based frequency shift assay," ACS Applied Materials & Interfaces 11(20), 18145–18152 (2019).
11. J. U. Lee, W. H. Kim, H. S. Lee, K. H. Park, and S. J. Sim, "Quantitative and specific detection of exosomal miRNAs for accurate diagnosis of breast cancer using a surface-enhanced Raman scattering sensor based on plasmonic head-flocked gold nanopillars," Small 15(17), 1804968 (2019).
12. Y. Han, L. Qiang, Y. Gao, J. Gao, Q. He, H. Liu, L. Han, and Y. Zhang, "Large-area surface-enhanced Raman spectroscopy substrate by hybrid porous GaN with Au/Ag for breast cancer miRNA detection," Applied Surface Science 541, 148456 (2021).
13. N. Choi, H. Dang, A. Das, M. S. Sim, I. Y. Chung, and J. Choo, "SERS biosensors for ultrasensitive detection of multiple biomarkers expressed in cancer cells," Biosensors and Bioelectronics 164, 112326 (2020).
14. C. C. Andrei, A. Moraillon, E. Larquet, M. Potara, S. Astilean, E. Jakab, J. Bouckaert, L. Rosselle, N. Skandrani, R. Boukherroub, F. Ozanam, S. Szunerits and A. C. Gouget-Laemmel, "SERS characterization of aggregated and isolated bacteria deposited on silver-based substrates," Analytical and Bioanalytical Chemistry 413, 1417–1428 (2021).
15. H. Chen, A. Das, L. Bi, N. Choi, J. Moon, Y. Wu, S. Park, and J. Choo, "Recent advances in surface-enhanced Raman scattering-based microdevices for point-of-care diagnosis of viruses and bacteria," Nanoscale 12(42), 21560–21570 (2020).
16. M. B. Wabuyele, M. E. Martin, F. Yan, D. L. Stokes, J. Mobley, B. M. Cullum, A. Wintenberg, R. Lenarduzzi, and T. Vo-Dinh, "Portable Raman device for detection of chemical and biological warfare agents," Proceedings of SPIE 5692, 330−336 (2005).
17. A. Jaworska, S. Fornasaro, V. Sergo, and A. Bonifacio, "Potential of surface enhanced Raman spectroscopy (SERS) in therapeutic drug monitoring (TDM). A critical review," Biosensors 6(3), 47 (2016).
18. G. Q. Wallace, J. F. Masson, "From single cells to complex tissues in applications of surface-enhanced Raman scattering," Analyst 145 (22), 7162–7185 (2020).
19. A. Jaworska, K. Malek, and A. Kudelski, "Intracellular pH–Advantages and pitfalls of surface-enhanced Raman scattering and fluorescence microscopy–A review," Spectrochimica Acta Part A: Molecular and Biomolecular Spectroscopy 251, 119410 (2021).
20. C. Wen, H. Chen, X. Guo, Z. Lin, S. Zhang, X. C. Shen, and H. Liang, "Lysosome-targeted gold nanotheranostics for in situ SERS monitoring pH and multimodal imaging-guided phototherapy," Langmuir 37(1), 569-577 (2020).
21. E. Critselis, H. L. Heerspink, "Utility of the CKD273 peptide classifier in predicting chronic kidney disease progression," Nephrology Dialysis Transplantation 31(2), 249−254 (2015).
22. A. Bonifacio, S. D. Marta, R. Spizzo, S. Cervo, A. Steffan, A. Colombatti, and V. Sergo, "Surface-enhanced Raman spectroscopy of blood plasma and serum using Ag and Au nanoparticles: a systematic study," Analytical and Bioanalytical Chemistry 406, 2355–2365 (2014).
23. V. V. Volkov, J. McMaster, J. Aizenberg, and C. C. Perry, "Mapping blood biochemistry by Raman spectroscopy at the cellular level," Chemical Science 13(1), 133–140 (2022).
24. E. J. Want, I. D. Wilson, H. Gika, G. Theodoridis, R. S. Plumb, J. Shockcor, E. Holmes, and J. K. Nicholson, "Global metabolic profiling procedures for urine using UPLC–MS," Nature Protocols 5(6), 1005–1018 (2010).
25. F. Selimoğlu, M. E. Ayhan, "Silver nanoparticle decorated graphene-based SERS electrode towards procalcitonin detection," Vibrational Spectroscopy 126, 103539 (2023).
26. S. Feng, R. Chen, J. Lin, J. Pan, G. Chen, Y. Li, M. Cheng, Z. Huang, J. Chen, and H. Zeng, "Nasopharyngeal cancer detection based on blood plasma surface-enhanced Raman spectroscopy and multivariate analysis," Biosensors and Bioelectronics 25(11), 2414–2419 (2010).
27. Z. Hu, B. J. Deibert, and J. Li, "Luminescent metal–organic frameworks for chemical sensing and explosive detection," Chemical Society Reviews 43(16), 5815–5840 (2014).
28. F. Tian, F. Bonnier, A. Casey, A. E. Shanahan, and H. J. Byrne, "Surface enhanced Raman scattering with gold nanoparticles: effect of particle shape," Analytical Methods 6(22), 9116–9123 (2014).
29. V. Moisoiu, S. D. Iancu, A. Stefancu, T. Moisoiu, B. Pardini, M. P. Dragomir, N. Crisan, L. Avram, D. Crisan, I. Andras, and D. Fodor, "SERS liquid biopsy: An emerging tool for medical diagnosis," Colloids and Surfaces B: Biointerfaces 208, 112064 (2021).
30. S. Z. Al-Sammarraie, L. A. Bratchenko, E. N. Typikova, P. A. Lebedev, V. P. Zakharov, and I. A. Bratchenko, "Silver nanoparticles-based substrate for blood serum analysis under 785 nm laser excitation," Journal of Biomedical Photonics & Engineering 8(1), 010301 (2022).
31. J. Zhao, H. Lui, D. I. McLean, and H. Zeng, "Automated autofluorescence background subtraction algorithm for biomedical Raman spectroscopy," Applied Spectroscopy 61(11), 1225–1232 (2007).
32. P. Refaeilzadeh, L. Tang, H. Liu, L. Liu, and M. T. Özsu, "Encyclopedia of database systems," Cross-validation 5, 532–538 (2009).
33. J. Guo, Z. Rong, Y. Li, S. Wang, W. Zhang, and R. Xiao, "Diagnosis of chronic kidney diseases based on surface-enhanced Raman spectroscopy and multivariate analysis," Laser Physics 28(7), 075603 (2018).

34. A. Bonifacio, S. D. Marta, R. Spizzo, S. Cervo, A. Steffan, A. Colombatti, and V. Sergo, "Surface-enhanced Raman spectroscopy of blood plasma and serum using Ag and Au nanoparticles: a systematic study," Analytical and Bioanalytical Chemistry 406, 2355–2365 (2014).
35. X. Huang, B. Liu, S. Guo, W. Guo, K. Liao, G. Hu, W. Shi, M. Kuss, M. J. Duryee, D. R. Anderson, Y. Lu, and B. Duan, "SERS spectroscopy with machine learning to analyze human plasma derived sEVs for coronary artery disease diagnosis and prognosis," Bioengineering & Translational Medicine 8(2), e10420 (2023).
36. H. Yang, C. Zhao, R. Li, C. Shen, X. Cai, L Sun, C. Luo, and Y. Yin, "Noninvasive and prospective diagnosis of coronary heart disease with urine using surface-enhanced Raman spectroscopy," Analyst 143(10), 2235–2242 (2018).
37. S. Kucheryavskiy, "mdatools — R package for chemometrics," Chemometrics and Intelligent Laboratory Systems 198, 103937 (2020).
38. H. J. Koster, A. Guillen-Perez, J. S. Gomez-Diaz, M. Navas-Moreno, A. C. Birkeland, and R. P. Carney, "Fused Raman spectroscopic analysis of blood and saliva delivers high accuracy for head and neck cancer diagnostics," Scientific Reports 12(1), 18464 (2022).
39. F. S. Nahm, "Receiver operating characteristic curve: overview and practical use for clinicians," Korean Journal of Anesthesiology 75(1), 25–36 (2022).
40. Z. Wang, Y. Liu, W. Lu, Y. V. Fu, and Z. Zhou, "Blood identification at the single-cell level based on a combination of laser tweezers Raman spectroscopy and machine learning," Biomedical Optics Express 12(12), 7568–7581 (2021).
41. C. Polonschii, M. Potara, M. Iancu, S. David, R. M. Banciu, A. Vasilescu, and S. Astilean, "Progress in the Optical Sensing of Cardiac Biomarkers," Biosensors 13(6), 632 (2023).
42. L. A. Bratchenko, S. Z. Al-Sammarraie, E. N. Tupikova, D. Y. Konovalova, P. A. Lebedev, V. P. Zakharov, and I. A. Bratchenko, "Analyzing the serum of hemodialysis patients with end-stage chronic kidney disease by means of the combination of SERS and machine learning," Biomedical Optics Express 13(9), 4926–4938 (2022).
43. I. A. Bratchenko, L. A. Bratchenko, Y. A. Khristoforova, A. A. Moryatov, S. V. Kozlov, and V. P. Zakharov, "Classification of skin cancer using convolutional neural networks analysis of Raman spectra," Computer Methods and Programs in Biomedicine 219, 106755 (2022).
44. Z. Cheng, R. Wang, Y. Xing, L. Zhao, J. Choo, and F. Yu, "SERS-based immunoassay using gold-patterned array chips for rapid and sensitive detection of dual cardiac biomarkers," Analyst 144(22), 6533–6540 (2019).
45. H. Chon, S. Lee, S. Y. Yoon, E. K. Lee, S. I. Chang, and J. Choo, "SERS-based competitive immunoassay of troponin I and CK-MB markers for early diagnosis of acute myocardial infarction," Chemical Communications 50(9), 1058–1060 (2014).
46. C. Hu, L. Ma, M. Guan, F. Mi, F. Peng, C. Guo, S. Sun, X. Wang, T. Liu, and J. Li, "SERS-based magnetic immunoassay for simultaneous detection of cTnI and H-FABP using core–shell nanotags," Analytical Methods 12(45), 5442–5449 (2020).
47. X. Fu, Y. Wang, Y. Liu, H. Liu, L. Fu, J. Wen, J. Li, P. Wei, and L. Chen, "A graphene oxide/gold nanoparticle-based amplification method for SERS immunoassay of cardiac troponin I," Analyst 144(5), 1582–1589 (2019).
48. J. H. Lin, RA Patil, R. S. Devan, Z. A. Liu, Y. P. Wang, C. H. Ho, Y. Liou, and Y. R. Ma, "Photoluminescence mechanisms of metallic Zn nanospheres, semiconducting ZnO nanoballoons and metal-semiconductor Zn/ZnO nanospheres," Scientific Reports 4(1), 6967(2014).
49. S. Feng, W. Wang, I. T. Tai, G. Chen, R. Chen, and H. Zeng, "Label-free surface-enhanced Raman spectroscopy for detection of colorectal cancer and precursor lesions using blood plasma," Biomedical Optics Express 6(9), 3494–3502 (2015).
50. M. Tahira, H. Nawaz, M. I. Majeed, N. Rashid, S. Tabbasum, M. Abubakar, S. Ahmad, S. Akbar, S. Bashir, M. Kashif, S. Ali, and H. Hyat, "Surface-enhanced Raman spectroscopy analysis of serum samples of typhoid patients of different stages," Photodiagnosis and Photodynamic Therapy 34, 102329 (2021).
51. L. A. Bratchenko, I. A. Bratchenko, A. A. Lykina, M. V. Komarova, D. N. Artemyev, O. O. Myakinin, A. A. Moryatov, I. L. Davydkin, S. V. Kozlov, and V. P. Zakharov, "Comparative study of multivariative analysis methods of blood Raman spectra classification," Journal of Raman Spectroscopy 51(2), 279–292 (2020).
52. Y. A. Khristoforova, L. A. Bratchenko, M. A. Skuratova, E. A. Lebedeva, P. A. Lebedev, and I. A. Bratchenko, "Raman spectroscopy in chronic heart failure diagnosis based on human skin analysis," Journal of Biophotonics 16(7), e202300016 (2023).

Exploring Convolutional Neural Networks for the Classification of Acute Lymphoblast Leukemia Blood Cell Images

Andrey Trubnikov[1*] and Dmitry Savelyev[1,2]

[1] Samara National Research University, 34 Moskovskoye shosse, Samara 443086, Russia

[2] Image Processing Systems Institute, NRC "Kurchatov Institute", 151 Molodogvardeyskaya str.,Samara 443001, Russia

***e-mail:** anteii3mer@gmail.com

Abstract. This paper introduces a novel approach to blood cell classification using convolutional neural networks (CNNs). Our emphasis lies in methodological insights derived from comparative analyses across various CNN architectures, implemented in Python with PyTorch such as ResNet152V2, Xception, EfficientNetB5, and EfficientNetV2M. In exploring model capabilities and limitations, we observe that the simple and shallow architectures is not sufficient to learn patterns compared to more complex networks. During research we have discovered that EfficientNetV2M demonstrate stable results with mean F_1=0.891 score, which is higher compare to other models. Saliency maps are applied to reveal significant regions within or near cells, offering nuanced insights into morphological influences like cell shape. Extensive data augmentation allows one effectively mitigate overfitting, aligning train learning curves with validation and test splits. Our study is methodologically rich, comprising a meticulous data-specific overview, a robustness analysis through multiple model training, a systematic architecture comparison, and an in-depth examination using saliency maps. © 2024 Journal of Biomedical Photonics & Engineering.

Keywords: deep learning; acute lymphoblastic leukemia; convolutional neural network; blood cell classification; saliency maps; Python.

Paper #9045 received 15 Dec 2023; revised manuscript received 20 Dec 2023; accepted for publication 26 Dec 2023; published online 20 Feb 2024. doi: 10.18287/JBPE24.10.010302.

1 Introduction

Acute lymphoblastic leukemia (ALL) is a malignant disease of the hematopoietic system, which is caused by extensively proliferating lymphoblasts (immature lymphocytes). It is part of a large group of leukemias [1]. Unlike other leukemias, it is a rapidly progressive disease and in the absence of appropriate and timely treatment, it can lead to death in a few months [1]. About 85% of all cases are among children and adolescents under age 15 [2].

Literally there are several organs in the human body producing blood cells: bone marrow, lymph nodes, and spleen. ALL starts in the bone marrow, which, in case of dysfunction, can release immature leukocytes into the blood, which can sometimes affect other human organs (liver, spleen, brain, and others). The process of formation and maturation of lymphocytes is called lymphocytopoiesis and is shown in Fig. 1.

A distinctive feature of ALL is a strong morphological similarity between normal lymphoid cells and abnormalities [3]. Early diagnostic methods were based on morphological examination of peripheral blood smears, but now, cytogenetic examination, bone marrow biopsy, and lumbar puncture have become the main diagnostic tools [2]. Such approaches require highly qualified doctors and pathologists, special conditions and equipment. Therefore, such tests are usually not available to everyone.

The use of neural networks makes it possible to build automatic classification systems for digital images of blood cells without an expert knowledge. The possibilities of using machine learning are widely studied in related fields including this particular problem [4, 5].

This paper was presented at the IX International Conference on Information Technology and Nanotechnology (ITNT-2023), Samara, Russia, April 17–21, 2023.

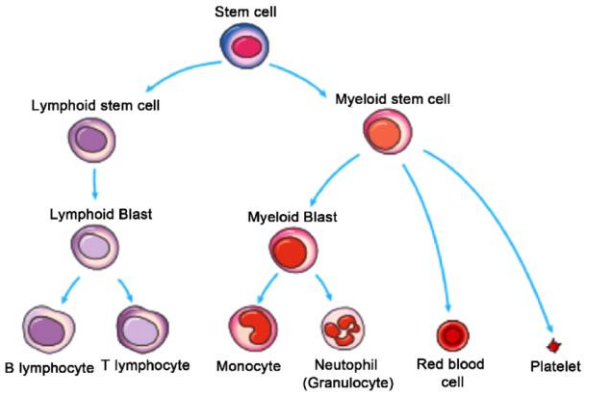


Fig. 1 Hematopoietic stem cell differentiation [2].

The purpose of this study is to analyze blood cell data with respect to its specifics and to conduct a comparative study of various neural network architectures.

The scientific novelty of this study lies in the fact that during the work, the distinctive features of cellular images were taken into account and the results of the trained models were interpreted, which was not carried out in similar works [6].

2 Methods

2.1 Microscopic Images

Data exploration is the first stage of classification pipeline, it includes calculations of numerical characteristics and revealing distinctive features that can be used in the future. When working with cellular images, it is worth paying attention to several features:

- small amount of available data,
- dataset imbalance,
- specific errors and noise,
- pre-segmentation,
- requires deep domain knowledge to manually construct features,
- high intra-class variability,
- variation among subjects.

2.1.1 Data Availability

Usually, medical data falls under the category of personal data, so some preliminary administrative work is required to work with them. Therefore, medical data is usually collected only for a specific and pre-approved purpose, which greatly affects their overall availability. Nevertheless, medical slowly become more and more available [7].

2.1.2 Dataset Imbalance

The main sources of medical data are various diagnostic procedures and tests, such as ECG, CT, Echo, biochemical blood tests, and others. The purpose of diagnosis is to identify the disease. All this leads to a high percentage of healthy subjects in the total sample [8].

2.1.3 Specific Errors

Depending on the subject area, the data may contain specific errors. For example, radiographic images inevitably contain impulse noise, which can be effectively eliminated by a median filter [9]. When working with digital images of microscopic photographs of cells, several sources of noise can be identified [10−12]:

- lightning,
- the optical system of the microscope and camera,
- staining.

There are many ways to eliminate the errors introduced by these factors [13]. In the analyzed data, lighting and coloring errors were minimized by applying a special color normalization method.

2.1.4 Preliminary Segmentation

Often digital microscopic photographs require prior processing in the form of segmentation. This step is required due to the fact that initially the whole cells ensembles are presented in the images, from which it is necessary to isolate individual cells. The error introduced by this procedure depends on whether manual segmentation is performed (then the error depends on the qualifications and expertise of the person conducting it) or automatic (in this case, the error value will depend on the specific algorithm) segmentation [14, 15]. Typical pre-segmentation errors include: the presence of more than one cell in the resulting image, violation of cell integrity, selection of an empty area.

2.1.5 High Level of Required Qualifications

Manually constructing features from microscopic photographs of cells will require one or even several specialists with knowledge of the subject area (e.g., an oncologist and a cytologist).

2.1.6 High Intra-Class Variability

Depending on many factors (the developmental process, the etiology of the disease, anomalies, etc.), cell characteristics for every class may vary (for example, morphological features such as size, shape, color, granularity, cytoplasmic volume, etc.) [16].

2.1.7 Variation Among Subjects

Given the original format of most medical samples (the presence of patient's id feature), this factor deserves special attention. The values of cell features within the same class can also vary significantly for two separate subjects due to the individual distinctions of the organism [3].

2.2 Data Augmentation

There are many different approaches to augmenting cellular data [17, 18], but most of them are based on utilization data specific features. So, in addition to the

features listed above that are important for building an adequate model, we can highlight characteristics of images, through the use of which it is possible to increase the size of the training set. Main feature of cells is their axial and point symmetry (in this regard). Thus, there is an invariance of the image class to the use of random rotation and mirror reflection.

In addition, to increase the resistance of the classifier to random noise and for regularization, a random error can be introduced into the training data [19].

When using image augmentation techniques, it is also worth to consider the ratio of sizes of the final and initial samples and the amplitude values of the characteristics used.

Data distinctive features (class invariance to image rotation and introduction of small noises) can be used for their augmentation (rotation by a random angle, introduction of random noise). This approach will partially overcome the initial limitation associated with the availability of data. These values should be selected empirically so as not to make significant changes to the distribution of original features.

2.3 Training Parameters

The data set consists of 10,581 digital photographs of lymphoid blood cells, among which two classes are represented: normal cells and abnormal ones (lymphoblasts) [20]. The files have a .bmp extension and a resolution of 600 × 600.

Different machine learning or deep learning tools can be used for cells classification. Previous studies have compared various machine learning models with convolutional neural networks and found out that deep learning methods achieve better results [9].

Also, a big advantage of deep learning methods is the absence of the need for manual feature engineering, which, as mentioned above, is a significantly difficult when working with cell images.

Several architectures of convolutional neural networks were selected for the further experiments. All of them represent different approaches to building deep networks: VGG16 (wide networks), ResNet152V2 (deep networks), EfficientNetB5 (result of NAS), EfficientNetV2M (second iteration, also result of NAS) [21, 22]. Also, a hypothesis was formulated and tested that a relatively narrow and shallow network, without preliminary training, would not able to learn from the initial data and carry out a successful classification for the test set.

As all of selected models were pretrained, suitable strategy for changing the learning rate parameter was chosen [23].

Each model was trained 6 times with different random seeds to further estimate how stochastic nature of the training process affect results.

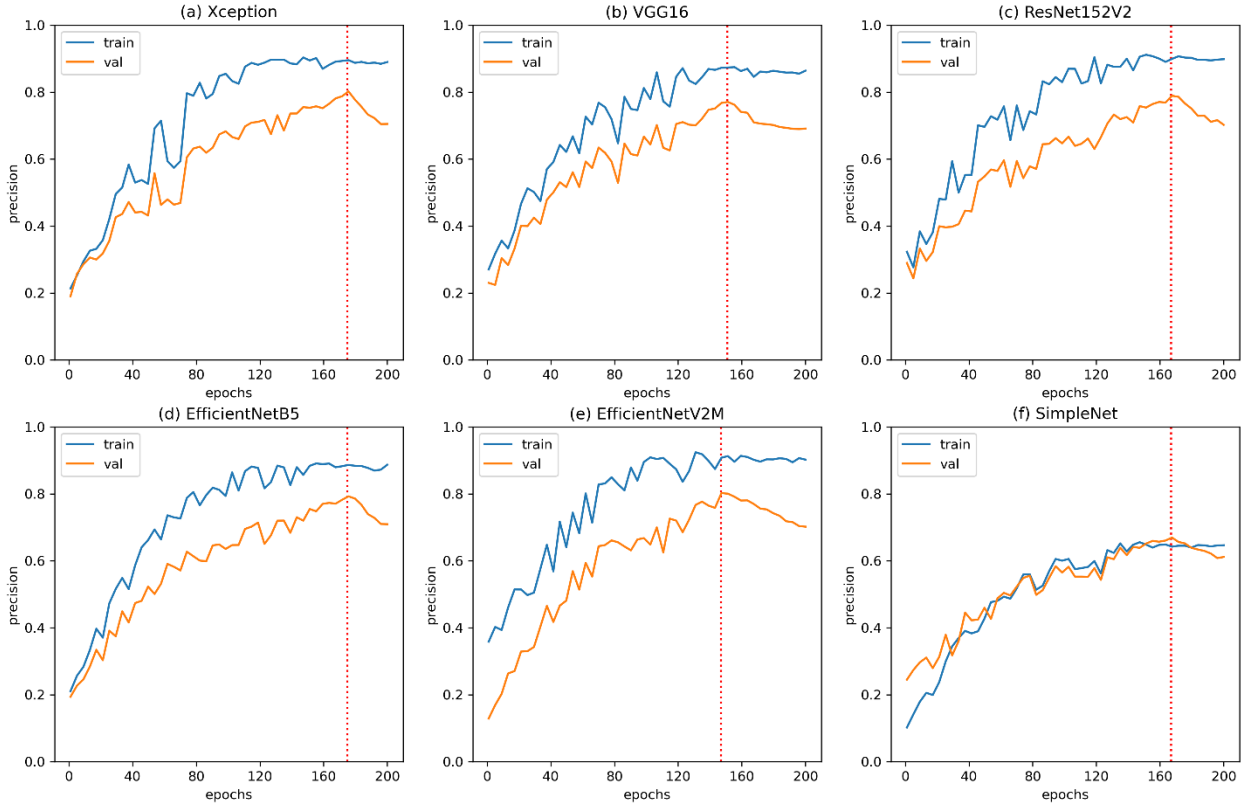


Fig. 2 Precision curves for selected models: (a) Xception, (b) VGG16, (c) ResNet152V2, (d) EfficientNetB5, (e) EfficientNetV2M, and (f) SimpleNet.

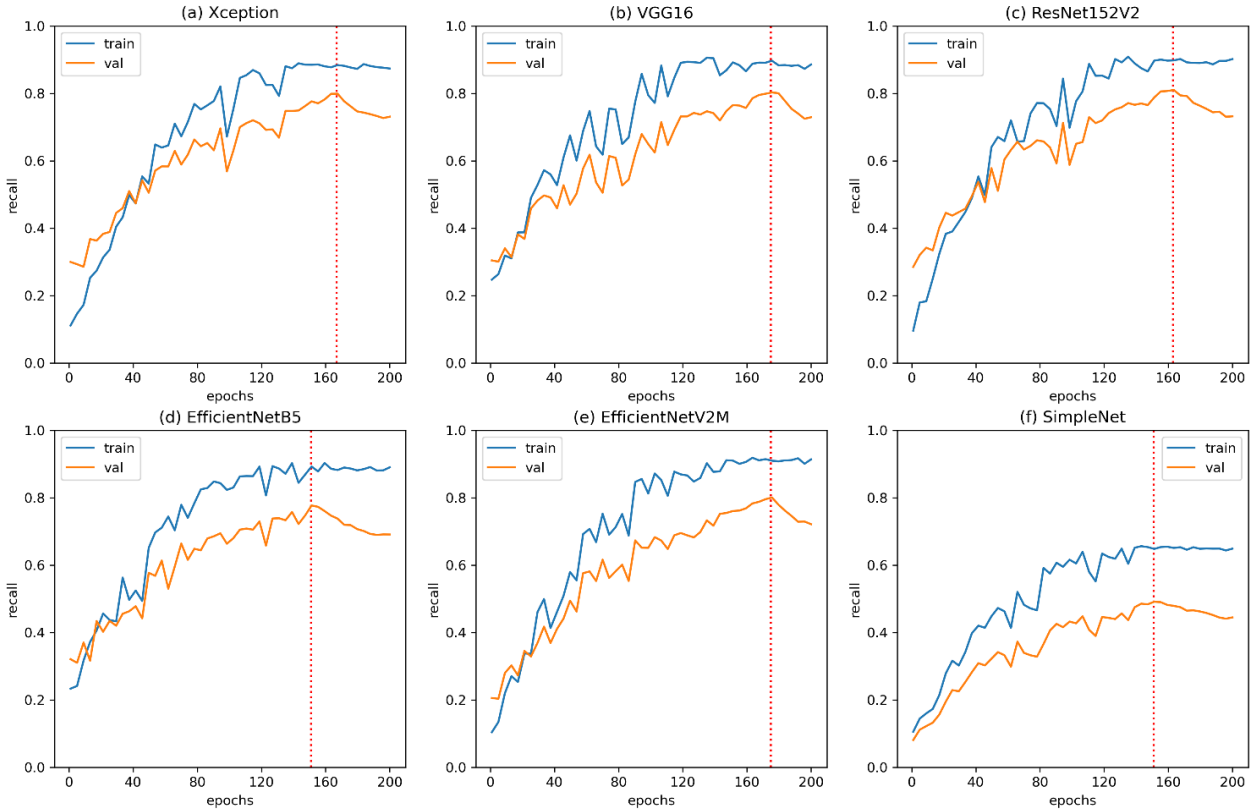


Fig. 3 Recall curves for selected models: (a) Xception, (b) VGG16, (c) ResNet152V2, (d) EfficientNetB5, (e) EfficientNetV2M, and (f) SimpleNet.

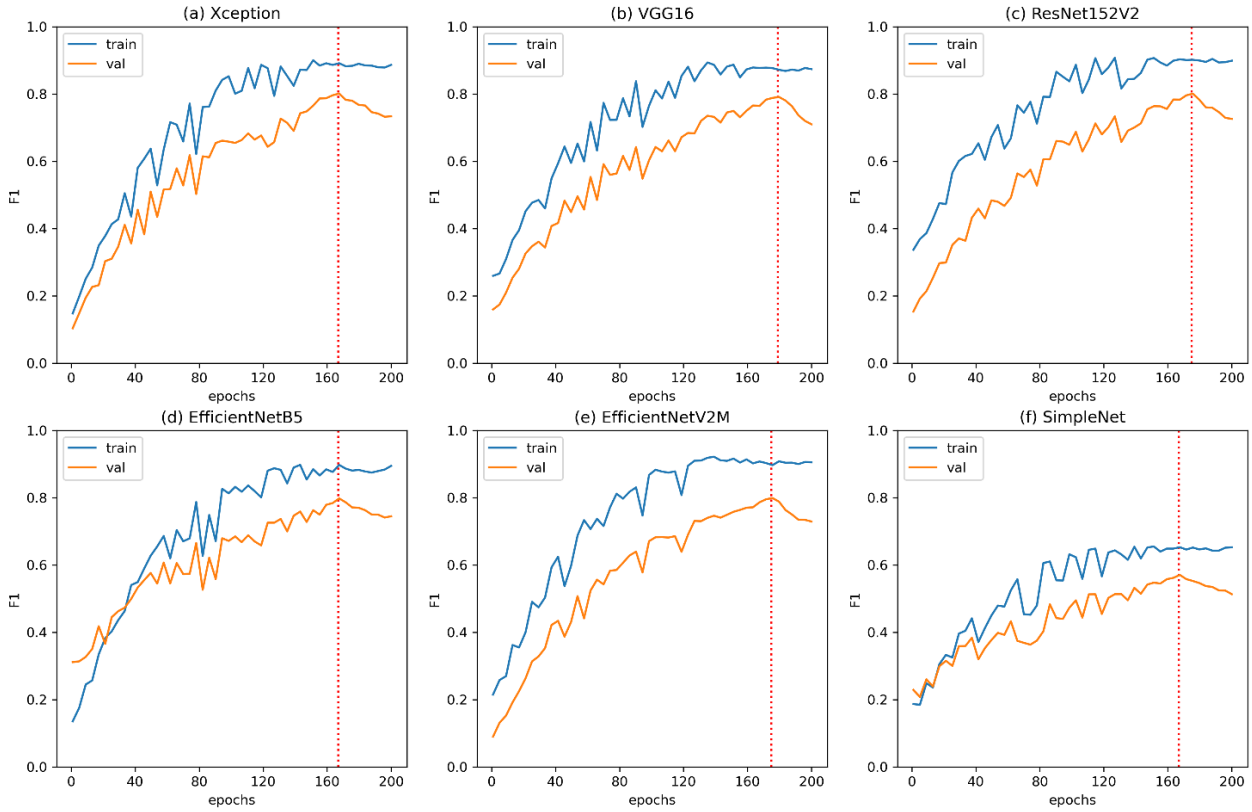


Fig. 4 F_1 score curves for selected models: (a) Xception, (b) VGG16, (c) ResNet152V2, (d) EfficientNetB5, (e) EfficientNetV2M, and (f) SimpleNet.

The original dataset was split in a ratio of 90:5:5 (training, validation, and test sets). The partitioning was performed with respect to the fact that cell properties, in particular morphological properties, can vary greatly among subjects. Thus, data splits have no intersection by subjects (patients).

Several metrics were chosen for evaluation by the following Eqs. (1−3):

$$precision = \frac{TP}{TP+FP}, \quad (1)$$

$$recall = \frac{TP}{TP+FN}, \quad (2)$$

$$F_1 = \frac{2*precision*recall}{precision+recall}. \quad (3)$$

Since the original dataset is not balanced, an *adequate* and *interpretable* estimate can be obtained based only on all three values.

At the same time, saliency maps were used to interpret the results of the model operation [24−27].

3 Results and Discussion

Each model was trained 6 times for 200 epochs. Learning curves for different metrics presented in Figs. 2−4.

Vertical red line on each plot depicted epoch with best F_1 value. For each plot it is can be seen that models start gradually decline or stagnate after reaching their best F_1 value across all epochs. For further studies weights from these epochs will be taken.

Results of models evaluation on training, validation, and test splits are presented in Tables 1–3. Metric values presented in the following format: mean ± std.

It is easy to observe plateau on the right side of each plot in Figs. 2−4. This is because, each model has same initial learning rate and scheduler (exponential decay), according to this approximate value of learning rate after 150 epochs is 4.55e−9 (therefore plateau is to be expected).

Table 1 Results of models evaluation on the training set.

Model	Time, s	Precision	Recall	F_1	dF_1, %
Xception	417 ± 7	0.891 ± 0.009	0.88 ± 0.004	0.886 ± 0.005	4.186
VGG16	557 ± 6	0.864 ± 0.008	0.888 ± 0.014	0.875 ± 0.008	2.974
ResNet152V2	550 ± 12	0.901 ± 0.012	0.897 ± 0.009	0.899 ± 0.008	5.738
EfficientNetB5	777 ± 12	0.885 ± 0.009	0.887 ± 0.008	0.886 ± 0.006	4.221
EfficientNetV2M	671 ± 13	0.904 ± 0.006	0.911 ± 0.009	0.907 ± 0.006	6.727
SimpleNet	402 ± 9	0.645 ± 0.008	0.65 ± 0.014	0.647 ± 0.009	−23.846

Table 2 Results of models evaluation on the validation set.

Model	Time, s	Precision	Recall	F_1	dF_1, %
Xception	408 ± 6	0.847 ± 0.009	0.848 ± 0.007	0.847 ± 0.007	5.057
VGG16	561 ± 5	0.824 ± 0.008	0.862 ± 0.009	0.843 ± 0.004	4.474
ResNet152V2	542 ± 9	0.843 ± 0.011	0.863 ± 0.005	0.851 ± 0.004	5.528
EfficientNetB5	779 ± 8	0.847 ± 0.008	0.833 ± 0.012	0.842 ± 0.007	4.152
EfficientNetV2M	646 ± 8	0.855 ± 0.01	0.852 ± 0.009	0.854 ± 0.007	5.825
SimpleNet	439 ± 4	0.716 ± 0.012	0.524 ± 0.008	0.605 ± 0.008	−25.036

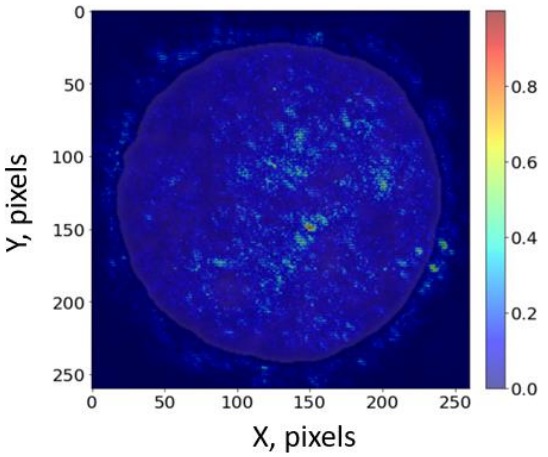
Table 3 Results of models evaluation on the test set.

Model	Time, s	Precision	Recall	F_1	dF_1, %
Xception	403 ± 4	0.805 ± 0.012	0.882 ± 0.011	0.841 ± 0.009	1.122
VGG16	562 ± 15	0.833 ± 0.004	0.86 ± 0.008	0.846 ± 0.005	1.723
ResNet152V2	550 ± 15	0.832 ± 0.01	0.88 ± 0.012	0.854 ± 0.005	2.685
EfficientNetB5	797 ± 7	0.847 ± 0.009	0.915 ± 0.007	0.881 ± 0.006	5.932
EfficientNetV2M	633 ± 9	0.868 ± 0.011	0.911 ± 0.013	0.891 ± 0.006	6.774
SimpleNet	430 ± 3	0.692 ± 0.110	0.669 ± 0.165	0.680 ± 0.098	−18.236

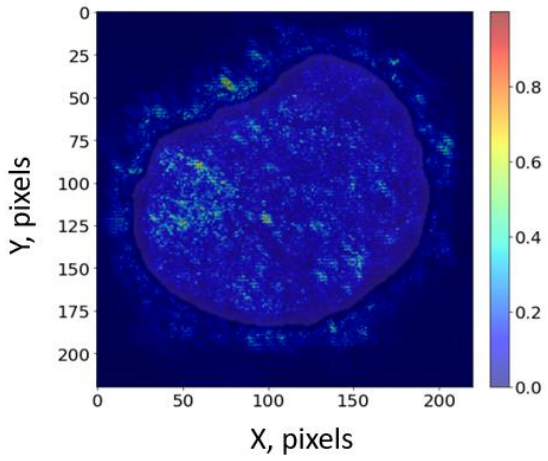
All models were trained 6 times to estimate variance created by stochastic nature of the training process (with different random seeds). Kruskal-Wallis test was performed to determine whether there is significant difference between model's results. With significance level of 0.05 null-hypothesis was rejected indicating that there is statistical difference in results.

The EfficientNetV2M showed the best results, while its infernce time differs little from other models (86.5 ms more than the average). The SimpleNet showed worst results and demonstrated the impossibility of applying small and primitive architectures on the given dataset.

Saliency maps depicted in Fig. 5 contains two examples: a normal cell and an anomaly. It can be seen that the attention of the model is distributed unevenly over the area of the cell (points outside the boundary are acceptable, since the used method for constructing saliency maps is quite noisy [24]). This means that some parts of the cell had a greater influence on the process of making decision by the model than others, so the information presented in these parts of the image may be used in a decision support system for a medical specialist.



(a)



(b)

Fig. 5 Saliency maps for EfficientNetV2M: a) normal cell, b) abnormal cell.

As we can see, examined simple model (SimpleNet) clearly does not have ability to learn patter from our data comparable with bigger and complex networks.

Exploring saliency maps for the best model (EfficientNetB5) also gives some insight. All important regions bounded are located within a cell or its vicinity, therefore we can conclude, that model has learned patterns possessed by a cell itself. Important regions are located both inside and on the border of a cell indicating that learned patterns influenced by some morphological cell features such as its shape.

One more observation can be made. Extensive usage of data augmentation techniques allowed us to overcome overfitting problem, lowering train learning curves and make it closer to those for validation and test splits.

While our study has provided valuable insights into the performance and interpretability of different neural network architectures for blood cell classification, it is essential to highlight the distinct contributions and differences of our work compared to existing literature.

In contrast with other researches we started our research from analyzing data and it is specific [28, 29]. We developed set of techniques to artificially increase sample size based on determined data characteristics and existing studies [30, 31].

Our investigation goes beyond model accuracy and includes a comprehensive analysis of model robustness what is absent in some existing works [30, 32]. By training each model multiple times with different random seeds, we aimed to estimate the variance introduced by the stochastic nature of the training process [33, 34]. This nuanced approach enhances the reliability of our findings and provides a more comprehensive understanding of the models' behavior.

We systematically compared the performance of multiple architectures, including EfficientNetV2M, SimpleNet, and EfficientNetB5. The use of both ANOVA and Kruskal-Wallis tests allowed us to rigorously assess the statistical differences among these models, providing a robust foundation for our conclusions [35].

The inclusion of saliency maps in our analysis adds an interpretability dimension to our study. We not only present model predictions but also explore where the models focus their attention. This qualitative analysis sheds light on the features influencing the decision-making process, offering potential applications in decision support systems for medical specialists [36−38].

In the future, it is planned to study the possibility of using auxiliary information to address intraclass and interclass variability [39−40]. It is also planned to extend comparison list of models and include transformer-based architectures (ViT-based models) [41].

4 Conclusion

The COVID-19 epidemic had a great impact on the development of information technologies in medicine and showed the importance of a developed information infrastructure. The emergence of models that provide an acceptable level of accuracy will make it possible to build

a large number of innovative systems: diagnostic systems, decision systems or decision support systems. In addition, it will be possible to centrally process the results of medical diagnostics, without being tied to the specific medical facilities.

In the course of the work, the features of the analysis of cellular images were identified, the data were augmented and divided into training and test sets, taking into account the distribution of subjects, experiments were carried out and model's outputs were interpreted. It was found that the best results on the given dataset were shown by the EfficientNetV2M architecture (the value of the target metric F_1 is 6.8% higher than the average among the architectures under consideration, while the difference between the worst and best value of the F_1 metric is 0.208).

Acknowledgements

This work was funded by the government project of the NRC "Kurchatov Institute".

Disclosures

The authors declare no conflict of interest.

References

1. I. Milevsky, Acute leukemias – history, causes, MedUniver, 18 March 2021 (accessed 23 May 2022). [https://meduniver.com/Medical/gematologia/ostrie_leikozi.html].
2. Overview Acute lymphoblastic leukaemia, UK (accessed 15 September 2022). [https://www.nhs.uk/conditions/acute-lymphoblastic-leukaemia].
3. W. Ladines-Castro, G. Barragan-Ibanez, M. Luna-Perez, A. Santoyo-Sánchez, J. Collazo-Jaloma, E. Mendoza-García, and C.O. Ramos-Peñafiel, "Morphology of leukaemias," Revista Médica del Hospital General de México 79(2), 107–113 (2018).
4. Y. Gu, A. Chen, X. Zhang, C. Fan, K. Li, and J. Shen, "Deep Learning based Cell Classification in Imaging FlowCytometer," ASP Transactions on Pattern Recognition and Intelligent Systems 1(2), 18–27 (2021).
5. S. Shafique, S. Tehsin, "Acute lymphoblastic leukemia detection and classification of its subtypes using pretrained deep convolutional neural networks," Technology in Cancer Research & Treatment 17, 153303381880278 (2018).
6. T. Pansombut, S. Wikaisuksakul, K. Khongkraphan, and A. Phon-On "Convolutional Neural Networks for Recognition of Lymphoblast Cell Images," Computational Intelligence and Neuroscience 2019, 7519603 (2019).
7. R. Cuocolo, M. Caruso, T. Perillo, L. Ugga, and M. Petretta, "Machine learning in oncology: a clinical appraisal," Cancer Letters 481, 55–62 (2020).
8. M. Khushi, K. Shaukat, T. M. Alam, I. A. Hameed, S. Uddin, S. Luo, X. Yang, and M. C. Reyes, "A comparative performance analysis of data resampling methods on imbalance medical data," IEEE Access 9, 109960–109975 (2021).
9. C. Lu, M. Chen, J. Shen, L. L. Wang, and C. C. Hsu "Removal of salt-and-pepper noise for X-ray bio-images using pixel-variation gain factors," Computers & Electrical Engineering 71, 862–876 (2018).
10. N. J. Everall, "Confocal Raman microscopy: common errors and artefacts," Analyst 135(10), 2512–2522 (2010).
11. J. Ludzik, C. Lee, A. Witkowski, and J. Hetts, "Minimizing sampling error using a unique ink–stained reflectance confocal microscopy-guided biopsy technique to diagnose a large lentigo maligna," JAAD Case Reports 24, 118–120 (2022).
12. W. Yu, W. K. Dodds, M. K. Banks, J. Skalsky, and E. A. Strauss, "Optimal staining and sample storage time for direct microscopic enumeration of total and active bacteria in soil with two fluorescent dyes," Applied and Environmental Microbiology 61(9), 3367–3372 (1995).
13. R. Laine, G. Jacquemet, and A. Krull, "Imaging in focus: An introduction to denoising bioimages in the era of deep learning," The International Journal of Biochemistry & Cell Biology 140, 106077 (2021).
14. T. Parag, A. Chakraborty, S. Plaza, and L. Scheffer, "A context-aware delayed agglomeration framework for electron microscopy segmentation," PloS One 10(5), e0125825 (2015).
15. S. U. Akram, J. Kannala, L. Eklund, and J. Heikkilä, "Cell segmentation proposal network for microscopy image analysis," in Deep Learning and Data Labeling for Medical Applications, G. Carneiro, D. Mateus, L. Peter, A. Bradley, J. M. R. S. Tavares, V. Belagiannis, J. P. Papa, J. C. Nascimento, M. Loog, Z. Lu, J. S. Cardoso, and J. Cornebise (Eds.), Springer International Publishing, 10008, 21–29 (2016).
16. A. Venkataramanan, M. Laviale, C. Figus, P. Usseglio–Polatera, and C. Pradalier, "Tackling inter-class similarity and intra–class variance for microscopic image-based classification," in Computer Vision Systems, M. Vincze, T. Patten, H. I. Christensen, L. Nalpantidis, and M. Liu (Eds.), Springer International Publishing, 12899, 93–103. (2021).
17. H. Rizk, A. Shokry, and M. Youssef, "Effectiveness of data augmentation in cellular-based localization using deep learning," in IEEE Wireless Communications and Networking Conference, 1–6 (2019).

18. S. Yu, S. Zhang, B. Wang, H. Dun, L. Xu, X. Huang, and X. Feng, "Generative adversarial network based data augmentation to improve cervical cell classification model," Mathematical Biosciences and Engineering 18, 1740–1752 (2021).
19. M. Momeny, A. M. Latif, M. A. Sarram, R. Sheikhpour, and Y. D. Zhang "A noise robust convolutional neural network for image classification," Results in Engineering 10, 100225 (2021).
20. "Leukemia Classification," US (accessed 16 Febrary 2024) [https://www.kaggle.com/datasets/andrewmvd/leukemia-classification].
21. M. Tan, Q. V. Le, "EfficientNet: rethinking model scaling for convolutional neural networks," International Conference on Machine Learning 10, 6105–6114 (2019).
22. G. Kyriakides, K. Margaritis, "An introduction to neural architecture search for convolutional networks," arXiv preprint arXiv:2005.11074v1 (2020).
23. X. Yin, W. Chen, X. Wu, and H Yue, "Fine-tuning and visualization of convolutional neural networks," 12th IEEE Conference on Industrial Electronics and Applications (ICIEA), 1310–1315 (2017).
24. G. Chelnlei, L. Zhang, "A Novel Multiresolution Spatiotemporal Saliency Detection Model and Its Applications in Image and Video Compression," IEEE Transactions on Image Processing 19(1), 185–198 (2010)
25. R. Monroy, S. Lutz, T. Chalasani, and V. Smolic, "Salnet360: Saliency maps for omni-directional images with CNN," Signal Processing: Image Communication 69, 26–34 (2018).
26. K. Nagasubramanian, S. Jones, A. K. Singh, B. Ganapathysubramanian, and S. Sarkar "Explaining hyperspectral imaging based plant disease identification: 3D CNN and saliency maps," arXiv preprint arXiv:1804.08831 (2018).
27. A. Alqaraawi, M. Schuessler, P. Weiß, E. Costanza, and N. Berthouze, "Evaluating saliency map explanations for convolutional neural networks: a user study," Proceedings of the 25th International Conference on Intelligent User Interfaces, 275–285 (2020).
28. A. Rehman, N. Abbas, T. Saba, S. I. Rahman, Z. Mehmood, and H. Kolivand, "Classification of acute lymphoblastic leukemia using deep learning," Microscopy Research and Technique 81(11), 1310–1317 (2018).
29. A. Genovese, M. S. Hosseini, V. Piuri, K. N. Plataniotis, and F. Scotti, "Acute lymphoblastic leukemia detection based on adaptive unsharpening and deep learning," in ICASSP 2021–2021 IEEE International Conference on Acoustics, Speech and Signal Processing (ICASSP), 1205–1209 (2021).
30. P. Chlap, H. Min, N. Vandenberg, J. Dowling, L. Holloway, and A. Haworth, "A review of medical image data augmentation techniques for deep learning applications," Journal of Medical Imaging and Radiation Oncology 65(5), 545–563 (2021).
31. F. Garcea, A. Serra, F. Lamberti, and L. Morra, "Data augmentation for medical imaging: A systematic literature review," Computers in Biology and Medicine 152, 106391 (2023).
32. L. H. S. Vogado, R. M. S. Veras, F. H. D. Araujo, R. R.V. Silva, and K. R.T. Aires, "Leukemia diagnosis in blood slides using transfer learning in CNNs and SVM for classification," Engineering Applications of Artificial Intelligence 72, 415–422 (2018).
33. D. Picard, "Torch. manual_seed (3407) is all you need: On the influence of random seeds in deep learning architectures for computer vision," arXiv preprint arXiv:2109.08203 (2021).
34. P. Madhyastha, R. Jain, "On model stability as a function of random seed," arXiv preprint arXiv:1909.10447 (2019).
35. J. Luengo, S. García, and F. Herrera, "A study on the use of statistical tests for experimentation with neural networks: Analysis of parametric test conditions and non-parametric tests," Expert Systems with Applications 36(4), 7798–7808 (2009).
36. N. Arun, N. Gaw, P. Singh, K. Chang, M. Aggarwal, B. Chen, K. Hoebel, S. Gupta, J. Patel, M. Gidwani, J. Adebayo, M. D. Li, and J. Kalpathy-Cramer, "Assessing the trustworthiness of saliency maps for localizing abnormalities in medical imaging," Radiology: Artificial Intelligence 3(6), e200267 (2021).
37. N. T. Arun, N. Gaw, P. Singh, K. Chang, K. V. Hoebel, J. Patel, M. Gidwani, and J. Kalpathy-Cramer, "Assessing the validity of saliency maps for abnormality localization in medical imaging," arXiv preprint arXiv:2006.00063 (2020).
38. M. Aggarwal, N. Arun, S. Gupta, A. Vaswani, B. Chen, M. Li, K. Chang, J. Patel, K. Hoebel, M. Gidwani, J. Kalpathy-Cramer, and P. Singh, "Towards trainable saliency maps in medical imaging," arXiv preprint arXiv:2011.07482 (2020).
39. C. Andreou, D. Rogge, and R. Müller, "A New Approach for Endmember Extraction and Clustering Addressing Inter– and Intra–Class Variability via Multiscaled–Band Partitioning," in IEEE Journal of Selected Topics in Applied Earth Observations and Remote Sensing 9(9), 4215–4231 (2016).
40. D. Lee, K. Kim, "Improved Noise–filtering Algorithm for AdaBoost Using the Inter–and Intra–class Variability of Imbalanced Datasets," Journal of Intelligent & Fuzzy Systems 43(4), 5035–5051 (2022).
41. Y. Liu, Y. Zhang, Y. Wang, F. Hou, J. Yuan, J. Tian, Y. Zhang, Z. Shi, J. Fan, and Z. He, "A survey of visual transformers," IEEE Transactions on Neural Networks and Learning Systems (2023).

Exploring the Relationship between Hypodermis Thickness and Diffuse Reflectance Spectra in Different Age and Gender Groups

Denis A. Davydov[1,2,3], Nikolay A. Fadeev[1], Ivan D. Filippov[1], and Gleb S. Budylin[2,4*]

[1] Faculty of Physics, M. V. Lomonosov Moscow State University, 1-2 Leninskie Gory, Moscow 119991, Russia

[2] Laboratory of Clinical Biophotonics, Biomedical Science and Technology Park, Sechenov First Moscow State Medical University, 8 Trubetskaya str., Moscow 119048, Russia

[3] Medical research and Educational Center, Lomonosov Moscow State University, 27-10 Lomonosovsky pr., Moscow 119991, Russia

[4] Institute of Spectroscopy of the Russian Academy of Sciences, 5 Physicheskaya str., Troitsk 108840, Russia

***e-mail:** budylin_g_s@staff.sechenov.ru

Abstract. This study explores the use of spatially-resolved diffuse reflectance spectroscopy for non-invasive method for measuring subcutaneous fat layer thickness. We investigated the relationship between spectroscopic measurements and hypodermis thickness, particularly focusing on lipid absorption amplitudes at varying source-detector distances. Our results reveal that lipid absorption amplitude is directly proportional to hypodermis thickness for layers between 1 and 4 mm at a source-detector fiber distance of 14 mm. The lipid absorption amplitude plateaued beyond a thickness of 4 mm, limiting sensitivity for the thicker hypodermis layer. An exponential function was revealed to describe lipid absorption amplitude dependence on the fat thickness across different source-detector distances. Physiological factors, namely sex, was found to significantly influence absorption amplitudes, while age-related differences were not identified. A predictive model was developed, yielding moderate accuracy (RMSE = 1.56 mm) in estimating hypodermis thickness, which is limited by the reference method. The study concludes that spatially-resolved diffuse reflectance spectroscopy is a promising method for assessing subcutaneous fat thickness, benefiting from its non-invasive nature and immediate results. However, accuracy is influenced by physiological characteristics, including sex and age, thus requiring personalized calibration. Future research should aim to refine predictive models and assess the technique's applicability across various body sites and a wider range of hypodermis thicknesses. © 2024 Journal of Biomedical Photonics & Engineering.

Keywords: spatially-resolved diffuse reflectance spectroscopy; hypodermis thickness; lipid absorption amplitude; physiological parameters; non-invasive assessment technique.

Paper #9044 received 5 Dec 2023; revised manuscript received 14 Feb 2023; accepted for publication 19 Feb 2023; published online 28 Feb 2024. doi: 10.18287/JBPE24.10.010303.

1 Introduction

Measuring the thickness of the subcutaneous adipose layer is a critical aspect of medical practice and research related to human health [1]. The subcutaneous fat layer serves as a key element in regulating body temperature, protecting organs from injury, and acting as a significant source of energy [1, 2]. The thickness of subcutaneous fat

can vary considerably among individuals and is influenced by a multitude of factors, including genetics, lifestyle, diet, and level of physical activity [3]. This variability underscores the importance of accurate assessment techniques for the subcutaneous adipose layer, which have implications for diagnosing and managing various health conditions.

Various approaches have been developed and are currently used in practice to assess the thickness of subcutaneous fat. Among the most common methods are those based on ultrasonography (US) [4–7], magnetic resonance imaging (MRI) [8–11], various types of biopsy [12], and a range of optical methods [13–15]. High-frequency ultrasound [4] is widely used to determine the thickness of the skin layers, underlying subcutaneous fat and muscles [5–7]. However, accurate and reproducible results require a high level of skill from the person interpreting US images. The MRI has also gained widespread acceptance as a comprehensive method for examining the human body. The resolution of modern equipment is about 0.1 mm [8], which allows MRI to be successfully applied in studying the structure of the skin [9–11]. However, the main disadvantages of this method are its relatively high cost and equipment size, which hinders its widespread use in clinical settings. Biopsy is currently considered the "gold standard" for analyzing skin structure in medicine. Its main drawback lies in the invasiveness of the method and the need for time-consuming laboratory investigations. Moreover, there are indications that biopsy-based measurements may have significant discrepancies compared to *in vivo* methods due to the loss of elasticity of the hypodermis after excision and prolonged storage of the skin sample, as well as potential distortion of the sample during procedures conducted for laboratory studies.

Diffuse reflectance spectroscopy (DRS) is often used to analyze the composition [16, 17] and thickness of biological tissues [18, 19] due to its relative simplicity, non-invasiveness and high measurement speed. In particular, the use of DRS may offer a promising solution to the problem of determining the thickness of the subcutaneous layer [13–15]. The main absorber in the dermis in the near-infrared (NIR) range is water, while lipids are the absorbers in the subcutaneous fat. Consequently, due to the different absorption spectra shapes of these layers (Fig. 1 (C)), depth scanning of the reflected signal would allow for the determination of hypodermis thickness (Fig. 1 (E)). Choi et al. (2008) [13] developed a non-invasive system for measuring the thickness of subcutaneous fat layer using DRS in the spectral range from 1000 to 1700 nm. Their results showed a high coefficient of determination (R^2 = 0.9954) between the measured and actual thickness of the subcutaneous fat layer in *ex vivo* tissue samples. In a study [14], the optical response around 930 nm, associated with lipid absorption, was investigated and compared with ultrasound images, MRI, and caliper measurements for assessing subcutaneous fat thickness. The results showed that optical methods can be an effective way to assess the thickness of subcutaneous fat with an average determination error of 1.2 and 0.8 mm, when using caliper and ultrasonic examination as the reference method respectively. The use of ultrasound as a reference method for measuring subcutaneous fat thickness has shown a high coefficient of determination when compared with DRS data, achieving an R^2 value of 0.9. This indicates a strong correlation and potential for accurate assessment of body tissue characteristics, such as the thickness of the subcutaneous fat layer. In study [15], the authors proposed the application of diffuse optical spectroscopy with temporal resolution within the same spectral range to evaluate body tissue composition with similar accuracy. However, a limitation of these studies is the small sample size of volunteers, which restricts the ability to discern correlations between the optical response and physiological attributes, including age and gender of the participants. This underscores the need for further research with larger and more diverse populations to better understand the implications of optical measurements in the context of varying human physiological characteristics.

In this study, we assessed the thickness of the subcutaneous fat layer using spatially-resolved DRS on a group of 247 volunteers. The caliper measurement method was used for comparison in the creation of a method for determining the thickness of the hypodermis based on DRS data. The research included an analysis of the relationship between lipid absorption amplitude and the thickness of the subcutaneous fat layer, as determined by both DRS and caliper measurements. The impact of varying distances between the light source and the detector on this correlation was also explored. Additionally, machine learning methods were utilized to evaluate the impact of physiological parameters, such as gender and age, on the optical response of the skin. Statistically significant differences in relationships for subjects of different genders were identified, demonstrating the influence of these parameters on the accuracy of the predictive model. Furthermore, data from DRS were used to solve the inverse problem of estimating the thickness of the subcutaneous fat layer, achieving a determination accuracy within an error margin of 1.5 mm.

2 Materials and Methods

2.1 Cohort Description

A total of 247 subjects (97 males and 150 females) participated in a simultaneous caliper skin fold readings and near-infrared DRS study ((Fig. 1 (C), (E), (F)). The age of the participant was 25 ± 13 years spanning from 4 to 71 (Fig. 1(D)). The skin of the inner side of the forearm at a distance of approximately 5-10 cm from the elbow without visible vessels was used as a measurement site.

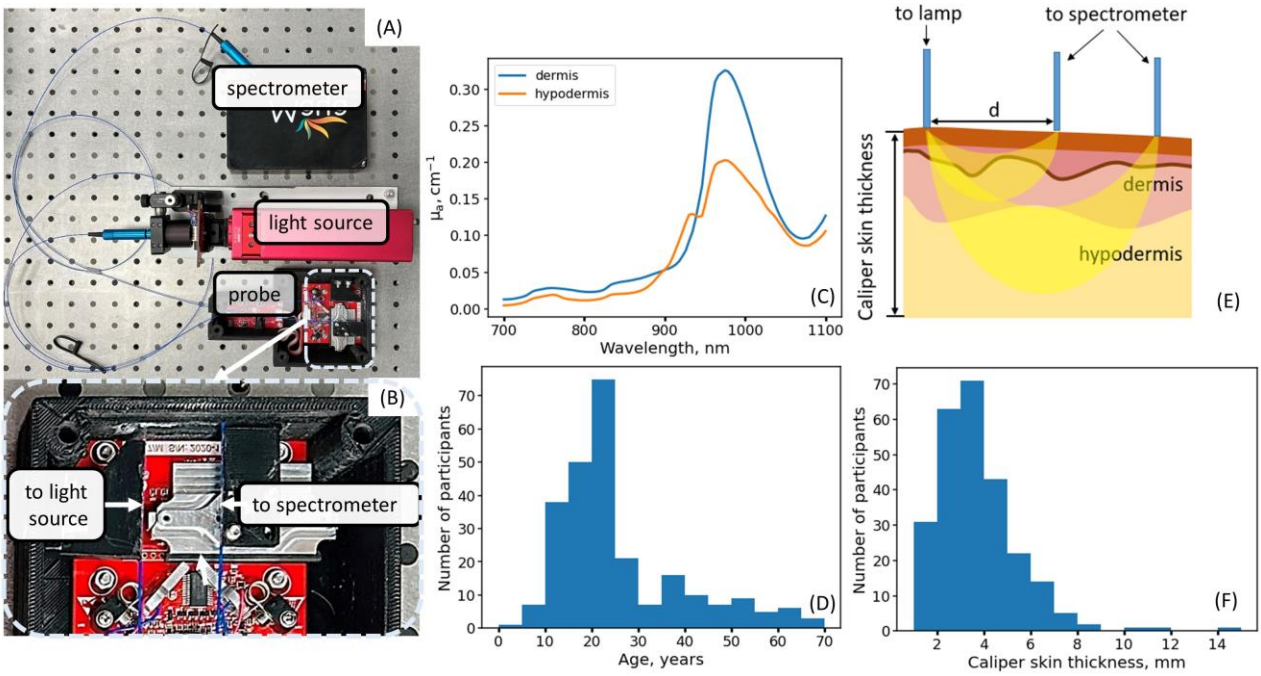


Fig. 1 (A) Photo of the experimental setup implementing diffuse reflectance spectroscopy. (B) Photo of the fiber optic probe used for measuring diffuse reflectance spectra at various distances between the source and detector. (C) Absorption spectra of the dermis and hypodermis. (D) Age distribution histogram of participants in the experiment. (E) Illustration of photon trajectories emitted from the source fiber, reaching the detector fiber at various distances between the source and detector. (F) Caliper skin thickness distribution histogram of participants in the experiment.

2.2 Diffuse Reflectance Spectra Measurements

The device used to measure spatially resolved diffuse reflectance spectra is described in detail in Ref. [20]. Briefly, the measurement component of the device featured a probe composed of two optical fibers, each with a core diameter of 550 μm. This probe was designed to detect diffuse reflection signals from the skin, functioning at various distances between the source and detector across a spectral range of 800–1100 nm (Fig. 1 (A), (B)). This probe allows the measurement of diffuse reflectance spectra at distances between the source and detector fibers, denoted as *d*, ranging from 0 to 14 mm with a step of 1 mm. A halogen lamp, SLS201 (Thorlabs, USA), was used as the light source and a Maya Pro 2000 spectrometer (Ocean Optics, USA) was used as the detector.

Diffuse reflectance spectra were calculated as follows:

$$R(\lambda) = \frac{I_{skin}(\lambda) - I_{dark}(\lambda)}{I_{ref}(\lambda) - I_{dark}(\lambda)}, \quad (1)$$

where $I_{skin}(\lambda)$ is the measured intensity of the reflected signal from the skin, $I_{dark}(\lambda)$ represents background signal, and $I_{ref}(\lambda)$ is the measured intensity from the standard (R = 99%, LabSphere, USA).

We calculated the effective optical density as follows [10]:

$$OD(\lambda) = -\log_{10}(R(\lambda)). \quad (2)$$

The absorption amplitude of lipid, denoted as Lipid Index (*LI*), was calculated from the effective optical density spectra using the following Eq. (3):

$$LI = OD(930\ \text{nm}) - OD(860\ \text{nm}). \quad (3)$$

The absorption amplitude of water, denoted as Water Index (*WI*), was calculated from the effective optical density spectra using the following Eq. (4):

$$WI = OD(970\ \text{nm}) - OD(860\ \text{nm}) \quad (4)$$

The possibility of assessing lipid and water content by these ratios was discussed in detail in our previous studies [20, 21].

In this study, to assess changes in parameters characteristic of different groups, the model proposed in Ref. [14] was used as one of the options. For this the dependency of the lipid absorption amplitude *LI* in the measured diffuse reflectance spectrum on the thickness of the hypodermis $d_{hypodermis}$, as measured using a caliper, was approximated for each distance between the source and detector fibers using the following exponential relationship:

$$LI = A\left(1 - e^{-B * d_{hypodermis}}\right), \quad (5)$$

where $A > 0$ and $B > 0$.

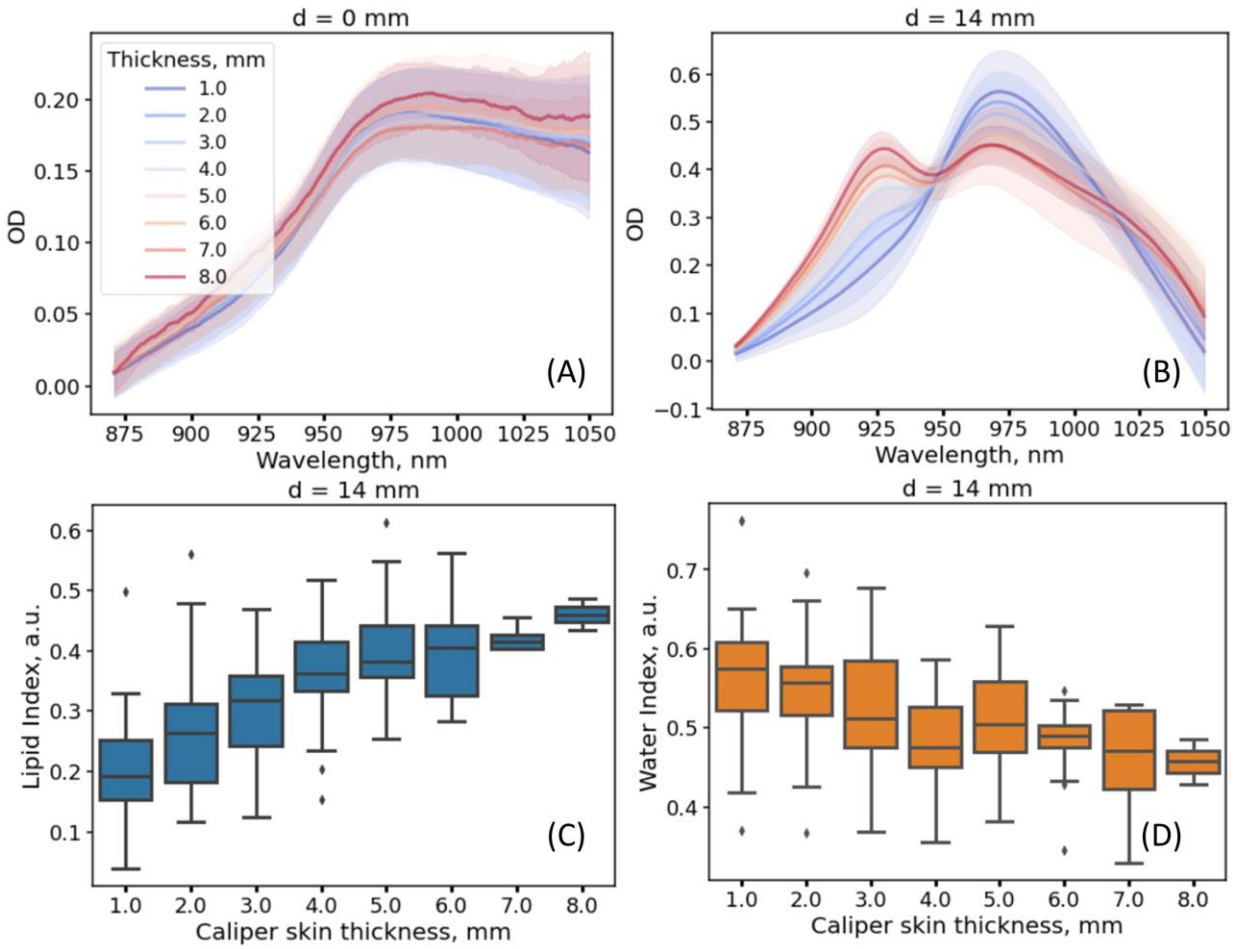


Fig. 2 Diffuse reflectance spectra measured at distances between the source and detector of d = 0 mm (A) and d = 14 mm (B) on the arms of volunteers with varying thicknesses of subcutaneous fat layer. (C) Dependence of lipid absorption amplitude, estimated from diffuse reflectance spectra at a 14 mm distance, on skin thickness measured by caliper (Eq. (3)). (D) Dependence of water absorption amplitude (Eq. (4)), estimated from diffuse reflectance spectra at a 14 mm distance, on skin thickness measured by caliper.

2.3 Assessment of the Significance of Physiological Parameters

As a second approach to assess changes in response, machine learning models were developed to determine the *LI* for various sets of physiological features, including gender and age. These models were subsequently compared. The entire sample was divided into a training set (80% of dataset), used for model training and validation, and a test set (20% of dataset), used to assess the quality of the resulting models with features such as gender and age. This division was made once. The relationship between the *LI* and the thickness of the hypodermis is nonlinear (refer to Eq. (5)). Therefore, to construct a baseline model from hypodermis thickness, linear regression with polynomial transformation of this parameter was employed. The optimal polynomial degree was determined through cross-validation. Cross-validation was done on the training set by randomly dividing the dataset into 5 folds. Prior to training the models, all features were standardized using the following algorithm: the median value of each feature was subtracted and then divided by the interquartile range of that feature. Gender was encoded as a binary numerical feature: 0 for female and 1 for male. The quality of the resulting machine learning models was evaluated by the coefficient of determination (R^2) and the root mean square error (RMSE), estimated on the test set.

3 Results and Discussion

Fig. 2 (A) and (B) depict the diffuse reflectance spectra measured at distances of 0 and 14 mm between the source and detector on volunteers with varying thicknesses of the subcutaneous fat layer on the arm. The spectra exhibit a local absorption maximum for water around 970 nm and for lipids around 930 nm.

The spectra measured at a small distance (d = 0 mm, Fig. 2(A)), showed only slight variations for different thicknesses of the subcutaneous fat layer. At greater distances between the source and detector, a significant increase in lipid absorption amplitude and a decrease in water absorption amplitude were observed (Fig. 2(B)).

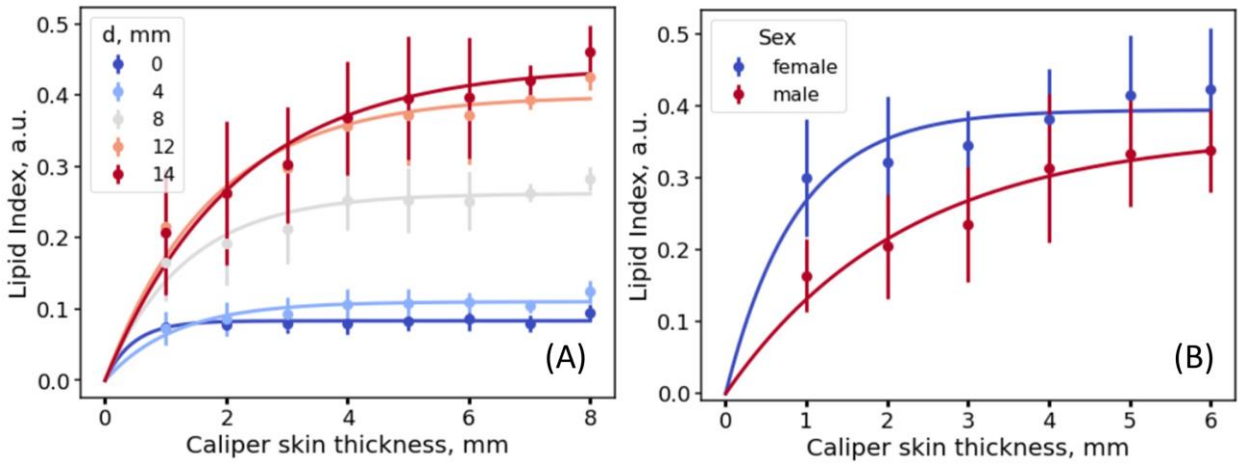


Fig. 3 (A) Dependence of lipid absorption amplitude (Lipid Index), estimated from diffuse reflectance spectra at various distances between the source and detector, on hypodermis thickness. Different distances between the source and detector are color-coded. (B) Dependence of lipid absorption amplitude, estimated from diffuse reflectance spectra at a distance of 14 mm between the source and detector, on hypodermis thickness. The gender of volunteers participating in the study is color-coded. On all panels, points indicate the mean value of Lipid Index and corresponding standard deviation for groups with fixed hypodermis thickness. Solid curves represent data approximation according to Eq. (5).

A direct proportionality between the measured lipid absorption amplitude and the thickness of the hypodermis, as measured by calipers, within a thickness range of 1 to 4 mm was observed (Fig. 1 (C)). Negative correlation was also observed between the water absorption amplitude and the thickness of the hypodermis (Fig. 2 (D)) within the same range of thicknesses. However, for thicknesses greater than 4 mm, the amplitudes of water and lipid absorption did not change significantly (Fig. 2 (C) and (D)).

Utilizing the spectra measured at various distances between the source and detector, we constructed relationships between the *LI* and the thickness of the hypodermis, as measured by calipers (Fig. 3 (A)). It is evident that the greater the distance between the source and detector, the larger the difference between the maximum and minimum values of the *LI* for the given caliper measurements.

The relationships presented in Fig. 3 were approximated by an exponential function (Eq. (4)). It was found that the maximum amplitude value A = 0.44 ±0.02 occurs at the greatest distance between the source and detector. The amplitude value A may differ from the value presented in Ref. [14], as it is contingent upon the method of assessing the contribution of lipids to the reflected signal, the distance between the source and detector fibers, and the diameters of the optical fibers.

As can be seen from Fig. 3 (A), for *LI* values averaged over groups with the same skin thickness, the dependence on skin thickness can be considered exponential. However, the standard deviation for each value of hypodermal thickness was high, which may be due to physiological parameters such as age and gender. To compare the observed contribution of lipids to the skin diffuse reflectance for different sexes, similar dependences and approximations were obtained using data divided into subsamples by sex (Fig. 3 (B)). Statistically significant differences were observed between these relationships for individuals of different sexes: A = 0.39 ± 0.02 for females, A = 0.36 ± 0.03 for males.

The difference in dependencies presented in Fig. 3 (B) is most likely due to the fact that the thickness of the dermis for women is on average less than that for men, and when measuring fold thickness using a caliper, the sum of the thicknesses of the dermis and hypodermis is measured. Thus, with equal caliper readings, the thickness of the hypodermis in women is higher, which is reflected in the DRS response and higher values of the calculated *LI*.

Next, using the obtained data, an inverse problem was solved. That is, using DRS data, the thickness of the hypodermis measured by calipers was determined. From the relationship presented in Fig. 3 (A) and approximation in Eq. (4), the hypodermis thickness in the range from 1 to 4 mm was expressed from the lipid absorption amplitude *LI*. As a result, the predicted model determines the thickness of the hypodermis with an accuracy of $R^2 = 0.24$ and RMSE = 1.56 mm. The obtained error is comparable to results achieved in work [14].

Due to the limited number of samples for some skin thicknesses, it was difficult to further divide the sample into groups by age to compare the parameters of the approximating dependencies for different age groups. Therefore, we assessed the influence of ageon the lipid absorption amplitude using machine learning approach. To this end, models were constructed to determine the *LI* for different sets of physiological features, as described in Table 1. Linear regression with polynomial transformation was used asthe base model for dependency on hypodermis thickness. Cross-validation revealed that the optimal degree of polynomial transformation is 3.

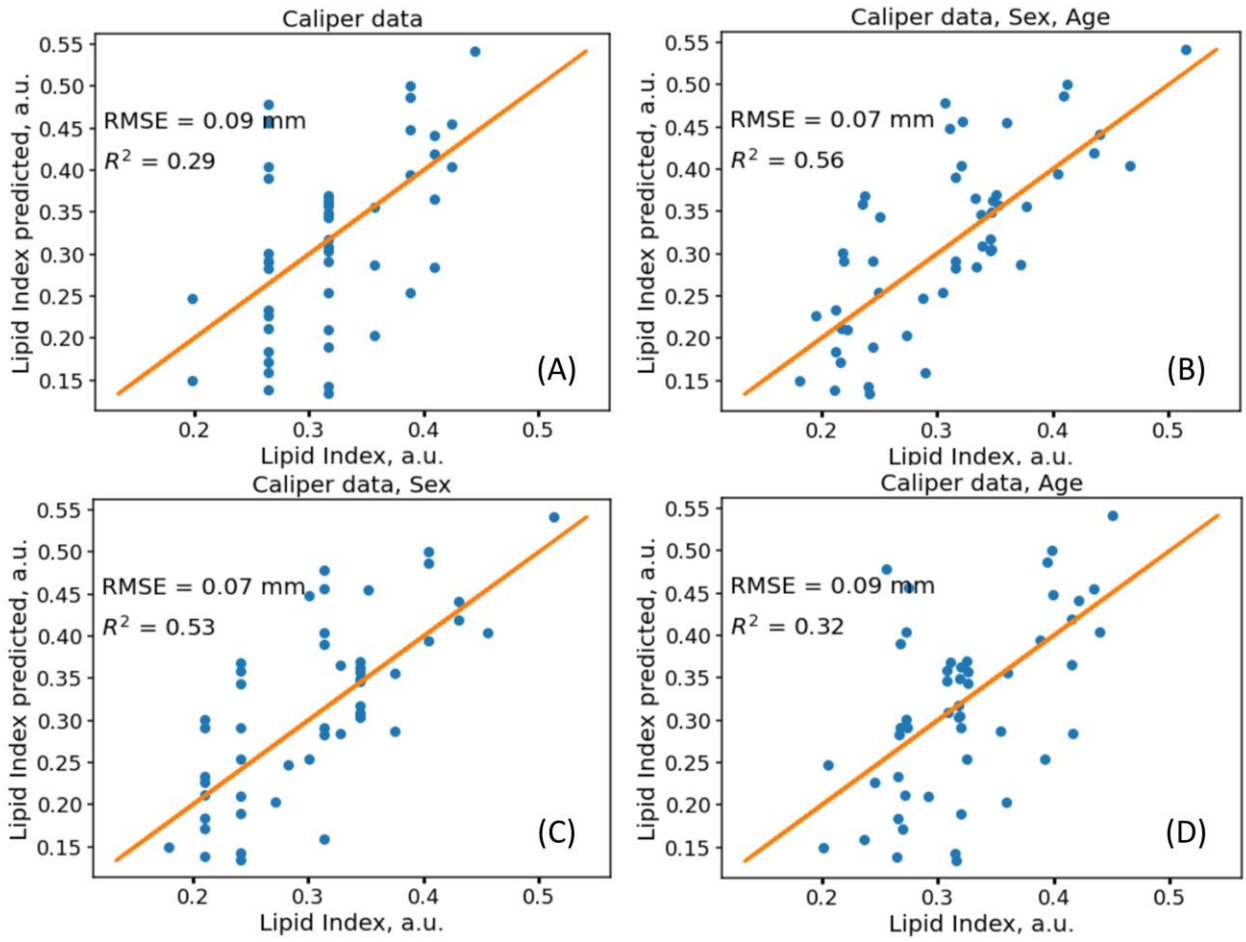


Fig. 4 Dependence of predicted Lipid Index values on measured cases when various feature sets were used: (A) caliper data, (B) caliper data, gender, age, (C) caliper data and gender, (D) caliper data and age.

Table 1 Feature sets for estimating water absorption amplitude using machine learning methods and corresponding coefficients of determination and standard deviation for the obtained models in determining lipid absorption amplitude *LI*.

№	Feature sets	R^2	RMSE
1	Caliper data, Sex, Age	0.56	0.07
2	Caliper data, Sex	0.53	0.07
3	Caliper data, Age	0.32	0.09
4	Caliper data	0.29	0.09

It was found that adding a binary feature defining the sex of the volunteer significantly increased the prediction accuracy on the test sample (R^2 = 0.53, RMSE = 0.07, Fig. 4 (C)), compared to the base model considering only caliper data (R^2 = 0.29, RMSE = 0.09, Fig. 4 (A)). This result is consistent with results obtained using the exponential approximation. Further addition of a feature defining the volunteer's age lead to slightly improved accuracy of the model (R^2 = 0.53, RMSE = 0.07, Fig. 4 (B)), however, this increase was not statistically significant. Similarly, no improvement in RMSE metrics was observed when comparing the base model with the model based on caliper data and age (Fig. 4 (A, D), Table 1, № 3,4).

Thus, both methods indicate the influence of sex on the dependence of the *LI* on the thickness of the hypodermis. In the sample considered, there was no significant effect of age on the shape of this dependence.

4 Conclusion

This study successfully demonstrated the application of spatially-resolved DRS as a non-invasive method for measuring the thickness of the subcutaneous fat layer. Our findings indicate that, while small distances between the source and detector do not provide significant variations in spectroscopic measurements, increasing this distance reveals a clear relationship between lipid and

water absorption amplitudes and the thickness of the hypodermis. The lipid absorption amplitude showed a direct proportionality to the hypodermis thickness for layers between 1 to 4 mm, as corroborated by traditional caliper measurements. Conversely, the water absorption amplitude exhibited negative correlation within the same thickness range. However, beyond a 4 mm thickness, these relationships plateaued, suggesting a limit to the method's sensitivity for thicker fat layers for a given source-detector distance. By establishing a *LI* and relating it to caliper measurements across different source-detector distances, we derived an exponential function that describes this relationship, with the function's maximum amplitude occurring at the largest distance. Notably, sex was identified as significant physiological factor influencing the absorption amplitudes, highlighting the importance of considering physiological factors in optical measurements. The predictive model developed from our data was able to estimate hypodermis thickness with moderate accuracy (RMSE = 1.56 mm), which is limited by the reference method. In conclusion, spatially-resolved DRS offers a promising alternative for assessing subcutaneous fat layer thickness. The method has a number of advantages, such as non-invasiveness, the ability to obtain immediate results, and, most importantly, the molecular specificity of the signal, allowing for a more detailed analysis of tissue composition. Unlike calipers, which do not account for the thickness of the dermis, our approach enables the analysis of a broader spectrum of tissue characteristics. In certain situations, measuring with calipers can be difficult due to curved surfaces, such as when measuring facial skin. In these cases, optical methods may be more appropriate. This makes our method particularly valuable for determining the characteristics of subcutaneous layers of bio-tissues and body composition. However, its accuracy is influenced by physiological characteristics, underscoring the need for personalized adjustment when using this technique in clinical or research settings. Future work should focus on refining the predictive models and exploring the utility of this method for different body sites and a broader range of hypodermis thicknesses.

Acknowledgments

This research was supported by the academic leadership program Priority 2030 proposed by Federal State Autonomous Educational Institution of Higher Education I. M. Sechenov First Moscow State Medical University of the Ministry of Health of the Russian Federation (Sechenov University). The work was supported by the Russian Science Foundation (Grant No. 21-79-10325).

Disclosures

The authors state no conflict of interest.

References

1. P. Trayhurn, J. H. Beattie, "Physiological role of adipose tissue: white adipose tissue as an endocrine and secretory organ," Proceedings of the Nutrition Society 60(3), 329–339 (2001).
2. E. D. Rosen, B. M. Spiegelman, "Adipocytes as regulators of energy balance and glucose homeostasis," Nature 444(7121), 847–853 (2006).
3. C. E. Elks, M. Den Hoed, J. H. Zhao, S. J. Sharp, N. J. Wareham, R. J. F. Loos, and K. K. Ong, "Variability in the heritability of body mass index: a systematic review and meta–regression," Frontiers in Endocrinology 3, 29 (2012).
4. H. Alexander, A. D. Miller, "Determining skin thickness with pulsed ultra sound," Journal of Investigative Dermatology 72(1), 17–19 (1979).
5. L. O. Olsen, H. Takiwaki, and J. Serup, "High-frequency ultrasound characterization of normal skin. Skin thickness and echographic density of 22 anatomical sites," Skin Research and Technology 1(2), 74–80 (1995).
6. C. Eisenbeiss, J. Welzel, W. Eichler, and K. Klotz, "Influence of body water distribution on skin thickness: measurements using high-frequency ultrasound," British Journal of Dermatology 144(5), 947–951 (2001).
7. K. Hoffmann, M. Stuücker, T. Dirschka, S. Goörtz, S. El-Gammal, K. Dirting, A. Hoffmann, and P. Altmeyer, "Twenty MHz B-scan sonography for visualization and skin thickness measurement of human skin," Journal of the European Academy of Dermatology and Venereology 3(3), 302–313 (1994).
8. J. Stefanowska, D. Zakowiecki, and K. Cal, "Magnetic resonance imaging of the skin," Journal of the European Academy of Dermatology and Venereology 24(8), 875–880 (2010).
9. S. Aubry, C. Casile, P. Humbert, J. Jehl, C. Vidal, and B. Kastler, "Feasibility study of 3-T MR imaging of the skin," European Radiology 19, 1595–1603 (2009).
10. J. Bittoun, H. Saint–Jalmes, B. G. Querleux, L. Darrasse, O. Jolivet, I. Idy-Peretti, M. Wartski, S. B. Richard, and J. L. Leveque, "In vivo high–resolution MR imaging of the skin in a whole–body system at 1.5 T.," Radiology 176(2), 457–460 (1990).
11. I. Idy-Peretti, J. Bittoun, F. A. Alliot, R. V. Cluzan, S. B. Richard, and B. G. Querleux, "Lymphedematous skin and subcutis: in vivo high resolution magnetic resonance imaging evaluation," Journal of Investigative Dermatology 110(5), 782–787 (1998).
12. C. Y. Tan, B. Statham, R. Marks, and P. A. Payne, "Skin thickness measurement by pulsed ultrasound; its reproducibility, validation and variability," British Journal of Dermatology 106(6), 657–667 (1982).

13. Y. S. Choi, H. K. Hong, B. J. Kim, M. N. Kim, and H. D. Park, "Development of a non-invasive measurement system to the thickness of the subcutaneous adipose tissue layer," Experimental Dermatology 17(6), 537–541 (2008).
14. D. Geraskin, H. Boeth, and M. Kohl-Bareis, "Optical measurement of adipose tissue thickness and comparison with ultrasound, magnetic resonance imging, and callipers," Journal of Biomedical Optics 14(4), 044017 (2009).
15. R. V. Warren, R. Bar–Yoseph, B. Hill, D. Reilly, A. Chiu, S. Radom–Aizik, D. M. Cooper, and B. J. Tromberg, "Diffuse optical spectroscopic method for tissue and body composition assessment," Journal of Biomedical Optics 27(6), 065002 (2022).
16. S. Inga, Z. Aleksejs, Z. Ilona, K. Janis, and S. Janis, "Comparison of a near-infrared reflectance spectroscopy system and skin conductance measurements for in vivo estimation of skin hydration: a clinical study," Journal of Biomedical Photonics & Engineering 3(1), 010310 (2017).
17. I. Fredriksson, M. Larsson, and T. Strömberg, "Machine learning for direct oxygen saturation and hemoglobin concentration assessment using diffuse reflectance spectroscopy," Journal of Biomedical Optics 25(11), 112905 (2020).
18. F. Geldof, B. Dashtbozorg, B. H. Hendriks, H. J. Sterenborg, and T. J. Ruers, "Layer thickness prediction and tissue classification in two–layered tissue structures using diffuse reflectance spectroscopy," Scientific Reports 12(1), 1698 (2022).
19. E. E. Nikonova, G. S. Budylin, A. S. Kochmareva, A. Y. Turkina, P. S. Timashev, and E. A. Shirshin, "Dental pulp location and dentin thickness assessment in situ with diffuse reflectance spectroscopy," Journal of Biomedical Photonics & Engineering 8(4), 040507 (2022).
20. D. A. Davydov, G. S. Budylin, A. V. Baev, D. V. Vaypan, E. M. Seredenina, S. T. Matskeplishvili, S. A. Evlashin, A. A. Kamalov, and E. A. Shirshin, "Monitoring the skin structure during edema in vivo with spatially resolved diffuse reflectance spectroscopy," Journal of Biomedical Optics 28(5), 057002 (2023).
21. G. S. Budylin, D. A. Davydov, N. V. Zlobina, A. V. Baev, V. G. Artyushenko, B. P. Yakimov, and E. A. Shirshin, "In vivo sensing of cutaneous edema: A comparative study of diffuse reflectance, Raman spectroscopy and multispectral imaging," Journal of Biophotonics 15(1), e202100268 (2022).

Highly Accurate EEG Signal Classification Using Multiple Feature Extraction and LSTM Networks

Deshmukh Deepika[1,2*] and Gillala Rekha[1]

[1] Department of Computer Science and Engineering, Koneru Lakshmaiah Education Foundation, Aziz Nagar, Hyderabad, Telangana 500075, India

[2] Department of Computer Science and Engineering, Mahatma Gandhi Institute of Technology, Hyderabad, Telangana 500075, India

***e-mail:** deshmukhdeepika@gmail.com

Abstract. Brain-computer interface (BCI) was first only thought of as a control channel for end users with simple disabilities, like those locked in a room. Nevertheless, the spectrum of BCI applications has significantly increased due to the multidisciplinary advancements made over the past ten years. Today's BCI technology can combine this artificial output with muscle-based natural products, directly translating brain impulses into control signals. Therefore, combining several biological signals for in-the-moment communication can benefit a far bigger population than first anticipated. New generations of assistive devices could aid individuals with preserved residual functions. Electroencephalography (EEG) signals can effectively perform BCI with maximum accuracy. This work will implement a new multiple-feature extraction-based BCI with a deep convolutional neural network to progress accuracy and reduce system complexity. The EEG signal is extracted from a database and then preprocessed using de-noising and smoothing techniques. Extracting features from the signal, then concatenating the features that have been extracted. After that, the Long Short-Term Memory (LSTM) network is used to train the signals. A proper preprocessing technique will remove the artefacts from the captured EEG signal. Sensitivity evaluation metrics, such as sensitivity, specificity, accuracy, etc., will be evaluated to validate the training and testing performance. This work achieves 99.35% accuracy, 96.38% sensitivity, 99.18% specificity, and 99.21% precision. By combining a range of feature extraction methods, we have effectively harnessed the complementary strengths of these techniques, resulting in a more holistic representation of the underlying neural activities. © 2024 Journal of Biomedical Photonics & Engineering.

Keywords: brain-computer interfaces; electroencephalography (EEG); deep convolutional neural networks; multiple feature extraction; sensitivity evaluation.

Paper #9029 received 21 Oct 2023; revised manuscript received 22 Jan 2024; accepted for publication 23 Jan 2024; published online 3 Mar 2024. doi: 10.18287/JBPE24.10.010304.

1 Introduction

The electroencephalography (EEG) records electrical impulses that exit the brain and makes it possible to retrieve valuable data about how the brain works. EEG-based brain-computer interface (BCI) is employed in many biological and medical procedures, such as detecting and treating central nervous diseases, assessing mental workload, and diagnosing brain tumors. In particular, BCI can assist in communicating brain instructions for those with motor neuron disease, forebrain stroke, brain trauma injury, palsy,

musculoskeletal problems, or other diseases affecting the control and response system between the brain and muscles and facilitate the authority of prosthetic joints [1].

The procedure provides control settings that may be utilised by healthy or disabled people to construct a new brain-computer connection. Either Event-Related Potentials (ERPs), which are time-locked reactions to an external event, or Event-Related Oscillatory Changes (EROCs), internally caused modulations in the continuing EEG, can typically be utilized as input to a BCI. One particularly well-liked and frequently employed mental technique is the imagination of movements. Electrodes affixed to the top of the head record the brain's electrical activity as EEG signals. The implementation of EEG signal analysis is based on curves, a graphical representation of collected data. The visual evaluation of these curves allows doctors to diagnose neural disorders [2].

Even when dealing with inexperienced doctors, relying solely on visual assessment might prove insufficient. The analysis of EEG signals holds significant importance, requiring algorithms to not only gather information from the recorded EEG signals but also process it effectively to predict and classify various brain states [3]. A notable challenge in EEG data processing lies in identifying epilepsy events. Research has indicated that by employing machine learning techniques to analyze the dynamics of task-related Independent Components (ICs), the performance of BCIs in predicting human patients' cognitive functions can be notably improved. To illustrate, ICs located in the temporoparietal region can aid in comprehending intended movement directions, while those in the posterior brain area can simulate individual performance, and sensorimotor ICs can serve as crucial markers for categorizing EEG patterns [4].

BCIs were once thought to be the only control channel whose intended end-users were people with severe impairments, such as those locked in. However, these initial objectives have been greatly expanded due to the transdisciplinary development made over the past ten years. Today's modern BCI technologies can translate brain signals directly into fresh output and mix this kind of synthetic production with a muscle-based prolactin level. Therefore, integrating numerous biochemical signals for real-time interaction has the opportunity to boost a much wider population than initially thought, from end users with maintained residue left features who can benefit from new assistive devices centuries to healthy individuals who could enhance their musculoskeletal achievement further than their normal capabilities [5].

In earlier investigations, factors like emotions, psychopathology, and focus were predictors of classification and impacted EEG data. In contrast, focus, attention level, relaxation, mood, and hand-grasping imagination are often the EEG signal variables translated in BCI. In most cases, the categorization method in the investigations only used one characteristic variable. In earlier research, BCI was utilized to operate computer applications, move characters in arcade games, and drive robotic wheelchairs via focus feedback. After feature extraction in pattern recognition, the classification system is used [6]. Several strategies have already been put forth to achieve BCI. The main issues with BCI are memory usage and computational complexity.

With limited and abundant samples of EEG training data focused on motor and mental imagery, Muhammad et al. introduced a novel automated framework based on pretrained convolutional neural networks (CNNs). This framework aims to enhance the robustness of BCI systems. Fifty-four individuals who performed MI on two separate days submitted the results of 21600 trials for the MI task to the database. It is composed of spectral-spatial insight, which embeds this same diversity. To evaluate the robustness of the features in two classes, an observation model based on information theory must first consider the discriminative frequency bands. This model uses spectral-spatial inputs. Spectrum-spatial inputs with the distinct features of brain signal patterns are produced from discriminative frequency bands and then converted into a covariance matrix. Spectral-spatial inputs are independently trained using a CNN during the feature representation phase, and they are then joined using a concatenation fusion technique [7].

Han et al. [8] proposed that compared to single-image EEG- and NIRS-based brain changes, a hybrid EEG/NIRS switch's performance was better. The fictional online research's findings typically showed the same overarching trend as those of the offline study. There was no noticeable difference in performance indicators between the disconnected and pseudo-online analytic methodologies when the quantity of keeping fit data was similar [8]. Zhang et al. [9] proposed a sparse Bayesian method for EEG classification by exploiting Laplace. Within a Bayesian evidence framework, a sparse discriminant vector undergoes hierarchical training with a Laplace prior. Comprehensive comparisons between the SBLaplace algorithm and various competing techniques are conducted using two EEG datasets [9].

Gupta et al. [10] proposed a unique feature-creation method for categorizing multi-mental tasks. The suggested approach extracts characteristics in two stages. The EEG signal is first broken down using the wavelet transform. Each feature component acquired in the second step is compactly expressed using eight parameters. The Optimal Decision Tree-Based Support Vector Machine (ODT-SVM) classifier is utilized for categorizing several mental tasks [10].

The motivation of this work is to enhance the accuracy and effectiveness of EEG signal classification, which can lead to a better understanding and utilization of brain signals for various applications, ranging from medical diagnoses to brain-controlled technologies.

The main objectives of the paper are

- to investigate brain activity throughout sensory perception and hand movement phases, ensuring EEG data matches neurological function.

- to enhance the classification performance of the BCI process for several classes while dealing with enormous datasets.

2 Proposed Method

The process begins by obtaining EEG signals from a database, which are subsequently subjected to preprocessing involving techniques like noise reduction and signal smoothing. Once the signals are refined, meaningful features are extracted from them. These extracted features are then combined by concatenation, forming comprehensive feature vectors. Subsequently, a CNN is employed to train the processed EEG signals. This involves feeding the concatenated feature vectors into the LSTM architecture, where convolutional layers identify intricate patterns, pooling layers aid in downsampling and feature selection, and fully connected layers make final predictions or classifications. The network is trained using labeled data, with optimization techniques refining its weights and parameters to minimize the difference between predicted outcomes and actual labels. This comprehensive process amalgamates signal preprocessing, feature extraction, concatenation, and LSTM-based training for a range of applications like medical diagnosis and cognitive analysis. Fig. 1 shows the block diagram of the proposed method.

2.1 Dataset

This dataset consists of a comprehensive collection of over 1500 EEG recordings, ranging from one to two minutes in length, and involving 109 individuals as participants. The EEG data was recorded using a 64-channel EEG setup facilitated by the BCI2000 system (https://archive.physionet.org/pn4/eegmmidb/).

During the recording sessions, the participants were involved in a variety of tasks. Each participant completed a total of 14 testing rounds, which included two initial one-minute baseline runs and three successive runs for each of the four distinct tasks. The dataset is fully explained in Table 1.

Table 1 Description of the dataset.

Sl. No	Task	Description
1	B-1	Eyes open
2	B-2	Eyes closed
3	Task 1	Make a left or right fist, and then shut it
4	Task 2	Imagine making a fist with your left hand and then closing it as well
5	Task 3	The two fists or both feet may be opened and closed
6	Task 4	Imagine opening and closing both fists or both feet
7	Task 1	Perform alternating open and close movements with either the left or right fist
8	Task 2	Mentally visualize the act of opening and closing either the left or right fist
9	Task 3	Execute alternating open and close movements with both fists or both feet
10	Task 4	Visualise opening and closing both fists or feet

2.2 Signal Preprocessing

Signal averaging is a time-domain signal processing method used to boost a signal's intensity compared to noise obscuring it [11]. The signal-to-noise ratio (SNR), ideally proportional to the square root of the number of measurements, will be improved by averaging a set of replicate measurements [12].

In order to smooth out signals using the time-fractional diffusion equation, it is necessary to search for a solution to Eq. (1) that is able to fulfil the starting requirements that have been specified. In other words, $u(x, 0)$ is a noisy signal, and $u(x, T)$ is the smoothed signal.

$$\begin{cases} \dfrac{\partial^{\alpha} u(x,t)}{\partial t^{\alpha}} = g(x,t,u)\dfrac{\partial^{2} u(x,t)}{\partial x^{2}}, \alpha \in (0,1), 0 < x < L, 0 < t < T, \\ u(x,0) = f(x), 0 < x < L, \\ u(0,t) = u(L,t) = 0, 0 < t < T. \end{cases} \quad (1)$$

where $g(x,t) = \exp[-(|\frac{d^2U(x,t)}{\lambda dx^2}|)^2]$ is a diffusion function. In general, $g(x, t)$ is a smooth decreasing function with $g(0, t) = 1$, $g(x, t) \geq 0$ and $g(x, t)$.

Normalization is the alteration of the indicator to a scale relative to a known and repeatable worth. The values in all four columns of the datasets span from positive immensity to negative immensity [13]. Min-max normalization is used in this study to restrict the values to those between 0 and 1 [14]. The linear transformation of the characteristics is maintained by min-max normalization. The Eq. (2) represents the min-max normalization. The min_i is the attribute's smallest value. The max_i is its maximum value.

$$N = \frac{n_i - min_i}{max_i - min_i}. \quad (2)$$

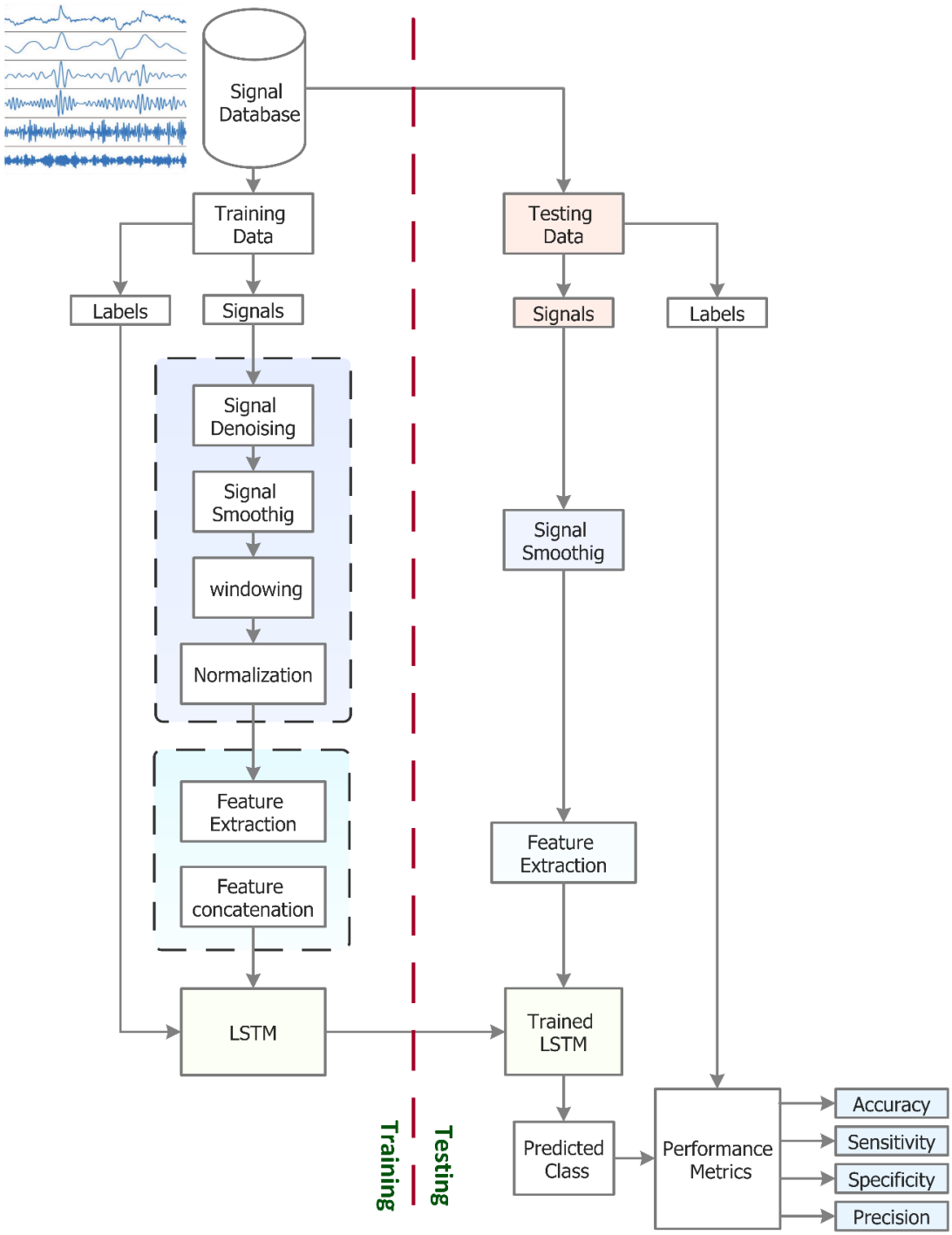


Fig. 1 Block diagram of the proposed method.

2.3 Feature Extraction

Mean

The mean value is the sum divided by the signal values. A relative measure of signal intensity could be how bright the signal appears compared to another [15].

$$\bar{x} = \frac{1}{n} \left(\sum_{i=1}^{n} x_i\right) = \frac{x_1 + x_2 + \cdots + x_n}{n}. \qquad (3)$$

Standard Deviation (SD)

The degree of dispersion of the data from the mean is expressed as a standard deviation. Using the following Eq. (3), the EEG signal's standard deviation can be determined as following [16]:

$$s = \sqrt{\frac{1}{N-1} \sum_{i=1}^{N} (x_i - \bar{x})^2}. \qquad (4)$$

Kurtosis

Kurtosis data sets with a high skewness value are more likely to have large tails or severe outliers [17]. Exceptions are usually absent, or the tails are light in data sets with moderate skewness values (Ieracitano).

$$Kurtosis[X] = \mathrm{E}\left[\left(\frac{X-\mu}{\sigma}\right)^4\right] = \frac{E[(X-\mu)^4]}{(E[(X-\mu)^2])^2} = \frac{\mu_4}{\sigma^4}. \quad (5)$$

Skewness

A measure reflecting a distribution's imbalance is skewness [18]. A distribution is said to be asymmetric when its left and right sides are devoid of signal [19].

$$\tilde{\mu}_3 = E\left[\left(\frac{X-\mu}{\sigma}\right)^3\right] = \frac{\mu_3}{\sigma^3} = \frac{E[(X-\mu)^3]}{(E[(X-\mu)^2])^{3/2}} = \frac{k_3}{k_2^{3/2}}. \quad (6)$$

Moment

The Moment invariant feature extraction approach is applied to extract the global features for form recognition and identification analysis [20]. Since its introduction, several varieties of the moment invariants approach have existed [21].

$$\mu_n = \int_{-\infty}^{\infty}(x-c)^n f(x)\ dx. \quad (7)$$

Energy

The energy refers to the likelihood (normalized histogram) of the brightness at the point [22]:

$$EG = \sum_i^{N_G}\sum_j^{N_G}\{p(i,j)\}^2. \quad (8)$$

Entropy (EN)

The Entropy (*EN*), a metric of unpredictableness, has the lowest value for an erratic matrix [23]. The following Eq. (9) defines this coefficient:

$$EN = -\sum_i^{N_G}\sum_j^{N_G} p(i,j)\log\big(p(i,j)\big). \quad (9)$$

Inertia (IN)

The Inertia (*IN*) also called the Contrast feature, measures the signal's contrast or any local fluctuations to show its quality [24]. This parameter is specified by the Eq. (10) below:

$$IN = -\sum_i^{N_G}\sum_j^{N_G}(i-j)^2\, p(i,j). \quad (10)$$

Correlation (CO)

The term correlation (*CO*) adjective assesses the linear relationships between the co-occurrence matrix's rows and columns. This parameter's definition is given by the Eq. (11) below:

$$CO = \frac{\sum_i^{N_G}\sum_j^{N_G}(i-\mu_x)(j-\mu_y)\ p(i,j)}{\sigma_x\sigma_y}, \quad (11)$$

where $\mu_x, \mu_y, \sigma_x, and\ \sigma_y$ are the means and standard deviations of $p_x p_y$.

Inverse Difference Moment (IDM)

The intensity of the spread of the items in the co-occurrence matrix and the components in its diagonal is measured by homogeneity, commonly known as the inverted differential second.

$$idm = \sum_i^{N_G}\sum_j^{N_G}\frac{1}{1+(i-j)^2}\ p(i,j). \quad (12)$$

Difference Entropy (DE)

Discrete entropy, used in signal processing, measures the number of bits needed to encode signal data. The signal will become more precise with the greater magnitude of entropy.

$$DE = -\sum_{K=0}^{N_G-1} P_{x-y}(k) log_2\, P_{x-y}(k). \quad (13)$$

2.4 Frequency Features

The Short-Time Fourier Transform (STFT), also referred to as the short-term Fourier transform, is a versatile and powerful tool in audio signal processing. It provides a time-frequency distribution that represents complex amplitude as a function of both time and frequency for a given signal. While it shares similarities with the Fourier transform in its use of fixed basis functions, the STFT differs by employing fixed-size time-shifted window functions to transform the signal, or *w(n)*.

$$X(k,m) = \sum_{n=0}^{N-1} x(n+m)w(n)W_N^{nk}, \quad k,m = 0,1,\ldots,N-1, \quad (14)$$

where *m* is the amount of shift. When compared to the Fourier transform, the STFT offers superior capability in terms of temporal and spectrum localised information. The produced characteristics, on the other hand, are unable to swiftly localise time and frequency because of the unending combination of temporal and frequency precision that is induced by the traditional Heisenberg's uncertainty principle. Furthermore, due to the fact that it has a constant time window and fixed basis functions, the STFT is still unable to detect events that have varying durations or when the signal is composed of quick events.

2.5 LSTM

Deep learning and intelligent systems use a Short-Term Long Memory (LSTM) deep neural network. In addition to analyzing single data bits, this type of Recurrent Neural Network (RNN) can analyze whole data sequences. Similar to how the moment-to-moment shift

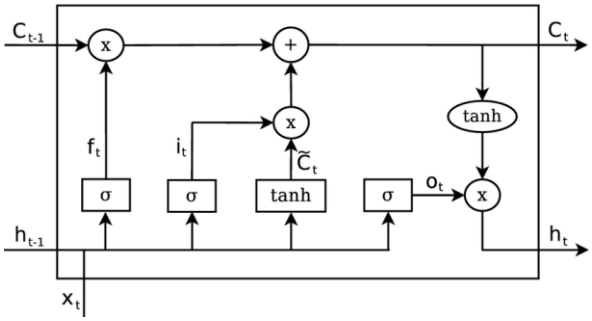


Fig. 2 LSTM architecture.

in electromagnetic discharge frequencies in the brain maintains short attention spans, the activity patterns in the system are disturbed once each time step. According to biological changes in synapse strength that are used to retain long-term memories, the connectivity weights and biases in the system disturbances once for each occurrence of training. Long-term memory is the term used to describe the short-term memory that the LSTM design aims to provide for RNN that can withstand thousands of time-steps.

Input and output gates are the only components of the LSTM design. The expressed as following:

$$i_t = \sigma(W_{ih}h_{t-1} + W_{ix}x_{t+}b_i), \quad (15)$$

$$c_t = tanh(W_{ch}h_{t-1} + W_{cx}x_{t+}b_c), \quad (16)$$

$$c_t = c_{t-1} + i_t c_t, \quad (17)$$

$$o_t = \sigma(W_{oh}h_{t-1} + W_{ox}x_{t+}b_o), \quad (18)$$

$$h_t = o_t \tanh(c_t), \quad (19)$$

where c_t denotes the cell state of LSTM. W_i, W_{ch}, and W_o are the weights, and the operator '·' shows two vectors multiplied together pointwise. The LSTM's structure is seen in Fig. 2. The LSTM's parameters are shown in Table 2. The selected loss function for the training process is Cross Entropy. The Adam optimizer is employed to optimize the model's parameters during training. A dropout rate of 0.5 is implemented, indicating that 50% of the neurons are randomly omitted during each training iteration to prevent overfitting. The training process is set to run for a maximum of 800 epochs, defining the number of times the entire dataset is processed by the model. During each iteration of training, a batch size of 100 is utilized, determining the number of data samples processed before updating the model's parameters. The learning process commences with an initial learning rate of 0.005, influencing the size of the steps taken during the optimization process. The Sigmoid activation function is chosen for the gates within the LSTM network, contributing to the control over the flow of information in the memory cell.

Algorithm 1 outlines the proposed method for classifying EEG signals, starting with input EEG data denoted as S_k and aiming to produce a classified EEG signal as output. The algorithm iterates through a dataset of EEG signals, performing a sequence of processing steps on each signal.

For each iteration from $k = 0$ to N, the algorithm follows these steps: Read the EEG signal S_k. Apply preprocessing to the signal, resulting in the preprocessed signal S_R. Extract statistical features from the preprocessed signal, which characterizes its statistical properties. Further extract frequency features (F_R) from the preprocessed signal to capture its spectral characteristics. Initialize the LSTM network ($LSTM\_I$) with training parameters. Train the LSTM network (LSTM) using the initialized parameters, along with the statistical and frequency features (S_k and M_R) obtained from the EEG signal. The algorithm repeats these steps for each signal in the dataset. The overall goal of this process is to classify EEG signals effectively using LSTM-based neural networks. It is important to note that the actual processing details and specific parameters used in these steps may vary depending on the implementation and goals of the EEG signal classification task.

Table 2 Training parameter of LSTM.

Parameter	Value
Loss Function	Cross Entropy
Optimizer	Adam
Dropout	0.5
Maximum Epochs	800
Batch size	100
Initial learning rate	0.005
Gate activation function	Sigmoid

Algorithm 1 Algorithm of Proposed method.

Input : Signal(S_k)
Output : Classified EEG Signal

For k=0 to N
Read Signal S_k,
S_R = preprocessed (S_k)
M_R = extract statistical feature(S_R)
F_R = extract frequency feature(S_R)
$LSTM\_I = Initialize(Training\ Parameter)$
$LSTM = Train(UNET_I, S_k, M_R)$
EndFor

The proposed BCI work is implemented using the Python programming language. Google Colab environment is used to compile the Python code. Various libraries are used to perform the feature extraction and ML training process. Keras library is used to perform the LSTM training operation. To improve the computation speed, the GPU of Colab is utilized. In this work, 80% of the data is used for training, and 20% is used for testing.

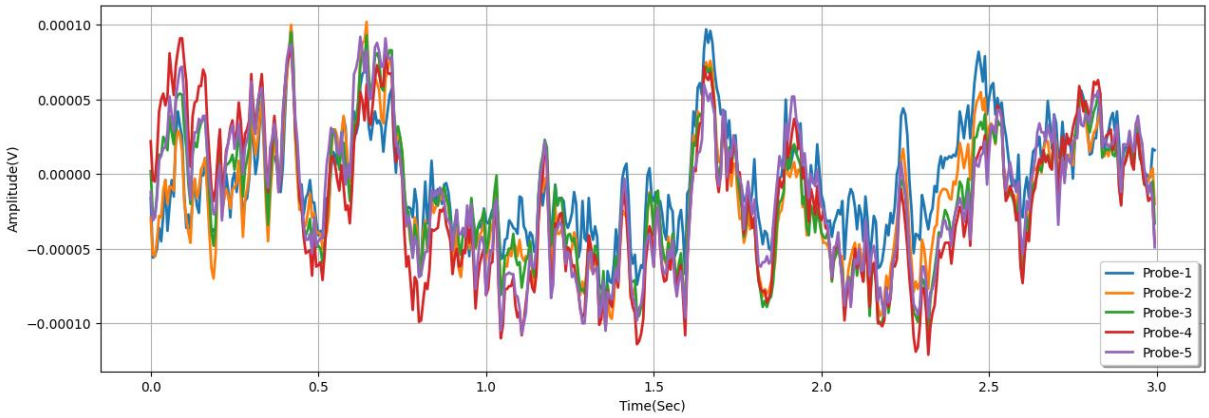


Fig. 3 Sample EEG signals from from the dataset.

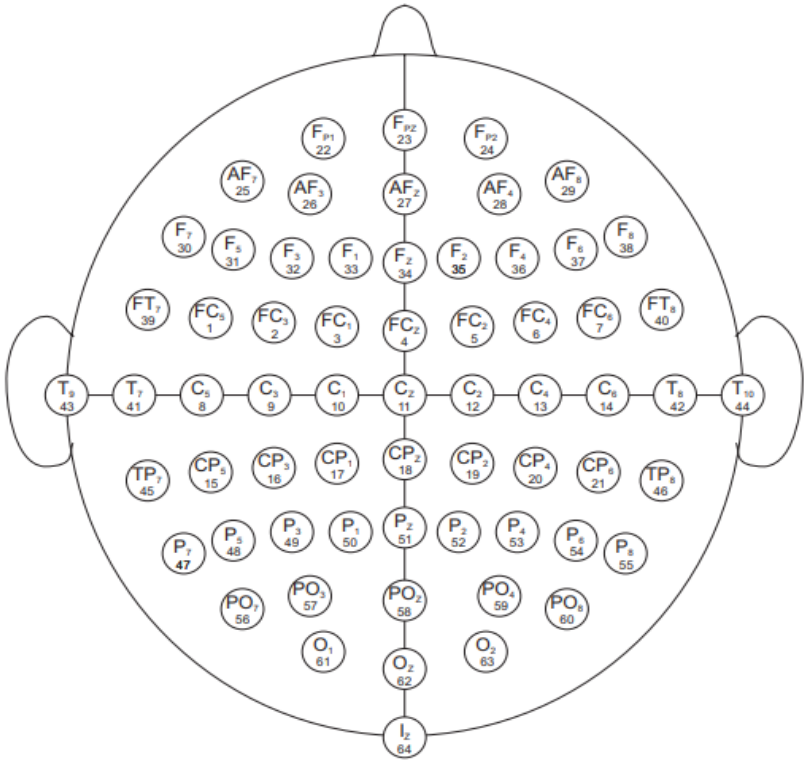


Fig. 4 Probe arrangement.

2.6 Performance Metrics

The accuracy gauges how many instances are correctly classified about the number of occurrences. The sensitivity may be stated as the proportion of correctly labelled positives. The ratio of the total of true negative to accurate negative findings to the total of true negative and false positive results is used to measure specificity. The proportion of better conversion results in diagnostic tests and analytics is known as precision.

$$Accuracy = \frac{TP+TN}{TP+TN+FP+FN}, \quad (20)$$

$$Sensitivity = \frac{TP}{TP+FN}, \quad (21)$$

$$Specificity = \frac{TN}{TN+FP}, \quad (22)$$

$$Precision = \frac{TP}{TP+FP}. \quad (23)$$

3 Results and Discussion

As indicated in Fig. 4, the EEGs were collected from 64 neurons using the worldwide 10-10 standard, eliminating terminals Nz, F9, F10, FT9, FT10, A1, A2, TP9, TP10, P9, and P10. Noting that signals in the database are numbers from 0 to 63, whereas the numerals in the picture vary from 1 to 64, the numbers beneath each electrode name reflect the sequence wherein they appear in the data. Fig. 3 shows the sample EEG signals from the dataset. Fig. 4 depicts the placement of the probes.

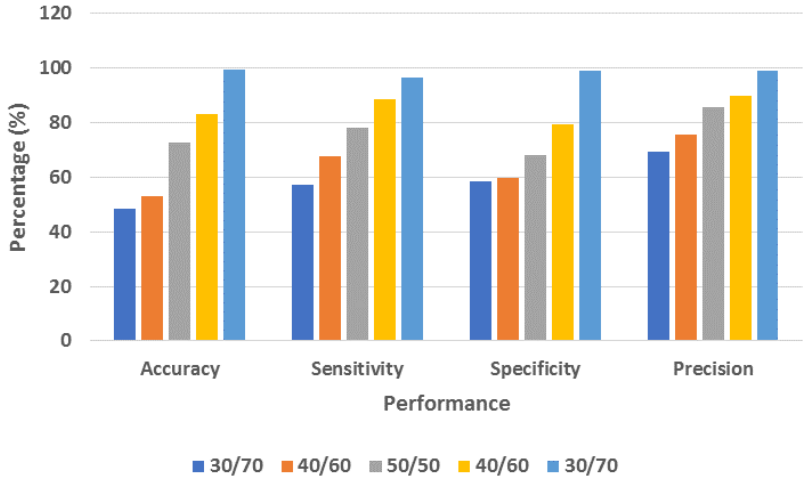


Fig. 5 Performance of the proposed method based on the training and testing ratio.

Table 3 Performance-based on training and testing ratio.

Training / Testing ratio	Accuracy	Sensitivity	Specificity	Precision
40/60	53.12%	67.49%	59.8%	75.63%
50/50	72.51%	78.17%	68.18%	85.64%
60/40	83.14%	88.39%	79.39%	89.96%
70/30	93.17%	90.21%	94.11%	94.71%
80/20	99.35%	96.38%	99.18%	99.21%

Table 4 Comparative performance of the proposed method.

Method	Accuracy	Sensitivity	Specificity	Precision
Ref. [22]	90%	–	–	–
Ref. [23]	98.31%	–	–	–
Ref. [24]	98.3%	–	–	94.7%
This work	99.35%	96.38%	99.18%	99.21%

The performance of classification process is given in Fig. 5. As shown, the accuracy, sensitivity, specificity and precision values are showed for different training ratio.

Table 3 presents the performance metrics of the model based on different training and testing data ratios. At a training/testing ratio of 40/60, the model achieved an accuracy of 53.12%, sensitivity of 67.49%, specificity of 59.8%, and precision of 75.63%. When the ratio was adjusted to 50/50, performance improved, with accuracy reaching 72.51%, sensitivity at 78.17%, specificity at 68.18%, and precision at 85.64%. Further increases in the training set proportion resulted in higher overall performance, with notable values at a ratio of 80/20, where accuracy peaked at 99.35%, sensitivity at 96.38%, specificity at 99.18%, and precision at 99.21%. These results underscore the influence of the training/testing ratio on the model's ability to generalize and perform effectively across different datasets.

The comparative effectiveness of the suggested strategy is displayed in Table 4. The Method [22] achieved an accuracy of 90%, while the Method [23] demonstrated an improved accuracy of 98.31%. Further, the Method [24] exhibited an accuracy of 98.3% and displayed a notable precision of 94.7%. The current work, however, outperformed these methods, attaining an impressive accuracy of 99.35%. Additionally, it achieved a high sensitivity rate of 96.38% and an impressive specificity of 99.18%. The precision for this work was also commendable at 99.21%. These results collectively underscore the advancements made in the current study compared to the previous methods. The suggested method's confusion matrix is displayed in Fig. 6. Fig. 7 shows the performance of the proposed method based on each class.

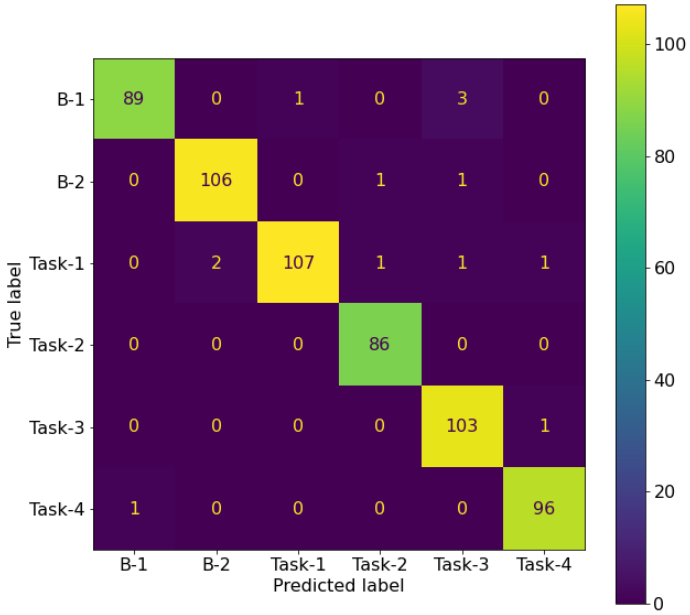


Fig. 6 Confusion matrix of the proposed method.

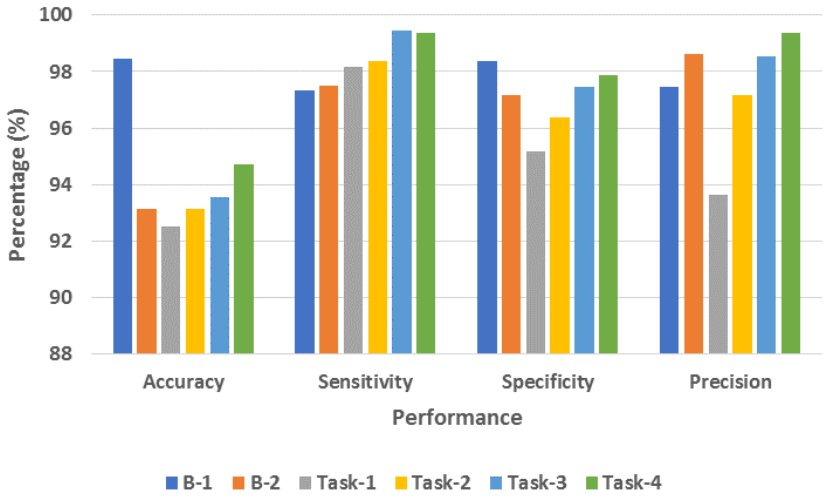


Fig. 7 Performance of the proposed method.

4 Conclusion

The proposed research focuses on enhancing EEG-based intention recognition through the implementation of LSTM networks in conjunction with signal normalization and smoothing techniques. The effectiveness of these refined algorithms is demonstrated through extensive experimentation with publicly available BCI databases, showcasing their ability to accommodate a wide range of human intentions and EEG sensitivities. Furthermore, this work includes a comprehensive examination of the various iterations of the proposed model and their interaction with dataset characteristics. This breakthrough represents a significant advancement in the precise identification of human intentions, holding great significance for the advancement of practical BCI system development. The findings of this work are supported by impressive performance metrics, including a remarkable accuracy rate of 99.35%, a sensitivity rate of 96.38%, specificities that reach 99.18%, and an exceptional precision rate of 99.21%.

Author Contributions

This paper is the responsibility of all authors, who authorised its submission.

Disclosures

On representation of all authors, the associated author denies conflict of interest.

Data Availability

The data that support the findings of this study are openly available at https://archive.physionet.org/pn4/eegmmidb/ (accessed 10 January 2024).

References

1. N. Kosmyna, A. Lécuyer, "A conceptual space for EEG-based brain-computer interfaces," PLoS ONE 14(1), e0210145 (2019).
2. X. Gu, Z. Cao, A. Jolfaei, P. Xu, D. Wu, T.-P. Jung, and C.-T. Lin, "EEG-Based Brain-Computer Interfaces (BCIs): A Survey of Recent Studies on Signal Sensing Technologies and Computational Intelligence Approaches and Their Applications," IEEE/ACM Transactions on Computational Biology and Bioinformatics 18(5), 1645–1666 (2021).
3. H. Cecotti, A. Graser, "Convolutional Neural Networks for P300 Detection with Application to Brain-Computer Interfaces," IEEE Transactions on Pattern Analysis and Machine Intelligence 33(3), 433–445 (2011).
4. N. Padfield, J. Zabalza, H. Zhao, V. Masero, and J. Ren, "EEG-Based Brain-Computer Interfaces Using Motor-Imagery: Techniques and Challenges," Sensors 19(6), 1423 (2019).
5. C.-T. Lin, T.-T. N. Do, "Direct-Sense Brain–Computer Interfaces and Wearable Computers," IEEE Transactions on Systems, Man, and Cybernetics: Systems 51(1), 298–312 (2021).
6. N. Even-Chen, S. D. Stavisky, C. Pandarinath, P. Nuyujukian, C. H. Blabe, L. R. Hochberg, J. M. Henderson, and K. V. Shenoy, "Feasibility of Automatic Error Detect-and-Undo System in Human Intracortical Brain–Computer Interfaces," IEEE Transactions on Biomedical Engineering 65(8), 1771–1784 (2018).
7. O.-Y. Kwon, M.-H. Lee, C. Guan, and S.-W. Lee, "Subject-Independent Brain–Computer Interfaces Based on Deep Convolutional Neural Networks," IEEE Transactions on Neural Networks and Learning Systems 31(10), 3839–3852 (2020).
8. C.-H. Han, K.-R. Muller, and H.-J. Hwang, "Enhanced Performance of a Brain Switch by Simultaneous Use of EEG and NIRS Data for Asynchronous Brain-Computer Interface," IEEE Transactions on Neural Systems and Rehabilitation Engineering 28(10), 2102–2112 (2020).
9. Y. Zhang, G. Zhou, J. Jin, Q. Zhao, X. Wang, and A. Cichocki, "Sparse Bayesian Classification of EEG for Brain–Computer Interface," IEEE Transactions on Neural Networks and Learning Systems 27(11), 2256–2267 (2016).
10. A. Gupta, R. K. Agrawal, J. S. Kirar, B. Kaur, W. Ding, C.-T. Lin, J. Andreu-Perez, and M. Prasad, "A hierarchical meta-model for multi-class mental task based brain-computer interfaces," Neurocomputing 389, 207–217 (2020).
11. D. J. McFarland, J. R. Wolpaw, "EEG-based brain–computer interfaces," Current Opinion in Biomedical Engineering 4, 194–200 (2017).
12. V. J. Lawhern, A. J. Solon, N. R. Waytowich, S. M. Gordon, C. P. Hung, and B. J. Lance, "EEGNet: a compact convolutional neural network for EEG-based brain–computer interfaces," Journal of Neural Engineering 15(5), 056013 (2018).
13. K. Wang, M. Xu, Y. Wang, S. Zhang, L. Chen, and D. Ming, "Enhance decoding of pre-movement EEG patterns for brain–computer interfaces," Journal of Neural Engineering 17(1), 016033 (2020).
14. D. Zhang, L. Yao, X. Zhang, S. Wang, W. Chen, R. Boots, and B. Benatallah, "Cascade and Parallel Convolutional Recurrent Neural Networks on EEG-based Intention Recognition for Brain Computer Interface," Proceedings of the AAAI Conference on Artificial Intelligence 32(1), (2018).
15. K.-S. Hong, M. J. Khan, and M. J. Hong, "Feature Extraction and Classification Methods for Hybrid fNIRS-EEG Brain-Computer Interfaces," Frontiers in Human Neuroscience 12, 246 (2018).
16. Y. Wang, M. Nakanishi, and D. Zhang, "EEG-Based Brain-Computer Interfaces," in Neural Interface: Frontiers and Applications. Advances in Experimental Medicine and Biology, 1101, X. Zheng (Ed.), Springer, Singapore, 41–65 (2019).
17. Z. Jin, G. Zhou, D. Gao, and Y. Zhang, "EEG classification using sparse Bayesian extreme learning machine for brain–computer interface," Neural Computing and Applications 32(11), 6601–6609 (2020).
18. C. Ieracitano, N. Mammone, A. Hussain, and F. C. Morabito, "A novel explainable machine learning approach for EEG-based brain-computer interface systems," Neural Computing and Applications 34(14), 11347–11360 (2022).
19. G. Zhang, V. Davoodnia, A. Sepas-Moghaddam, Y. Zhang, and A. Etemad, "Classification of Hand Movements From EEG Using a Deep Attention-Based LSTM Network," IEEE Sensors Journal 20(6), 3113–3122 (2020).
20. E. C. Djamal, H. Fadhilah, A. Najmurrokhman, A. Wulandari, and F. Renaldi, "Emotion brain-computer interface using wavelet and recurrent neural networks," International Journal of Advances in Intelligent Informatics 6(1), 1 (2020).
21. K. Takahashi, Z. Sun, J. Solé-Casals, A. Cichocki, A. H. Phan, Q. Zhao, H.-H. Zhao, S. Deng, and R. Micheletto, "Data augmentation for Convolutional LSTM based brain computer interface system," Applied Soft Computing 122, 108811 (2022).
22. Tan C, Sun F, Zhang W. Deep transfer learning for EEG-based brain-computer interface. In: 2018 IEEE International Conference on Acoustics, Speech and Signal Processing (ICASSP). IEEE; 2018. p. 916-920.
23. S. Sheykhivand, Z. Mousavi, T. Y. Rezaii, and A. Farzamnia, "Recognizing Emotions Evoked by Music Using CNN-LSTM Networks on EEG Signals," IEEE Access 8, 139332–139345 (2020).
24. Y. Zhang, G. Zhou, J. Jin, Q. Zhao, X. Wang, and A. Cichocki, "Sparse Bayesian Classification of EEG for Brain–Computer Interface," IEEE Transactions on Neural Networks and Learning Systems 27(11), 2256–2267 (2016).

The Implications of Varying Batch-Size in the Classification of Patch-Based Lung Nodules Using Convolutional Neural Network Architecture on Computed Tomography Images

Bushara A. R.*, Vinod Kumar R. S., and Kumar S. S.
Department of Electronics and Communication Engineering, Noorul Islam Center for Higher Education, Kumarakoil, Kanyakumari 629180, Tamil Nadu, India

***e-mail:** bushara.ar@gmail.com

Abstract. In recent years, the research on deep Convolutional Neural Networks (CNNs) has led to remarkable advancements in image categorization and segmentation. This paper presents a new Computer-Aided Detection (CAD) system utilizing convolutional neural networks and Computed Tomography (CT) image segmentation techniques to address the same problem of diagnostic lung nodule detection in low-dose CT scans. To simplify the approach, the system utilizes CNN for the classification of the malignant nodule. Specifically, divide each CT scan into several patches, with nodules and the remainder of the image falling into separate groups. Utilizing CT images from the Lung Image Database Consortium and Image Database Resource Initiative, the CNN models are evaluated. The overall accuracy metric measures the percentage of correctly classified instances (both benign and malignant) out of the total number of instances. From the results, it is observed that the overall accuracy generally ranges from 93% to 96% for different batch sizes. According to the findings, the most advanced model can achieve a detection accuracy of 96% with 256 batch size. © 2024 Journal of Biomedical Photonics & Engineering.

Keywords: medical image; deep learning; convolutional neural network; computed tomography; lung cancer.

Paper #9056 received 11 Jan 2024; revised manuscript received 5 Feb 2024; accepted for publication 12 Feb 2024; published online 4 Mar 2024. doi: 10.18287/JBPE24.10.010305.

1 Introduction

Lung cancer is the leading cause of cancer-related mortality, as reported by 2021 statistics from the American Cancer Society. The rate of lifespan of cancer patients can be greatly enhanced through careful monitoring for any signs of the disease. Computed Tomography (CT) is frequently applied by radiologists in the evaluation of lung cancer because of its high sensitivity to detect pulmonary nodules [1]. Lung cancer death can be reduced more effectively than with chest X-ray (radiograph) screening because of its higher detection rate [2]. Despite the high sensitivity of CT scans [3] in detecting nodules, it is still not easy for a radiologist to inform whether a nodule is benign or malignant in the procedure. According to the National Lung Screening Trial Research Team [4], monitoring using low-dose CT scans [5] lowered lung carcinoma deaths by 15–20%. Radiation exposure is increased because of unnecessary CT scans [6] instructed after a false positive diagnosis. In this research, a Convolutional Neural Network (CNN) [7] is proposed to identify whether a nodule is malignant or not, which will aid radiologists in making an accurate diagnosis of lung cancer. Deep learning, especially CNNs has transformed the world of medical imaging delivering remarkable advancements in pathology detection and classification. The use of CNNs in the patch-based method has proved effective not only for improving detection accuracy but

also minimizing time and resource consumption. Nevertheless, optimizing CNN architectures including finding an optimal batch size during the training process still proves to be a complicated issue. Optimization is essential to balance between computational resources and learning complex features in CT images that can help to improve diagnostic performance.

The major issue in using CNNs for lung nodule detection is the fact that there are different applications of nodules appearance and a large amount of data present within CT scans. Some of the drawbacks in this approach includes high false-positive, variable sensitivity resulting diagnostic oversight and unwarranted anxiety among patients. The selection of the batch size during CNN training plays a significant role as it influences the model generalizes, its stability in training and rate at which the convergence is occurring. An under-optimized batch size may cause suboptimal learning, which affects the ability of a system to differentiate between nodular and nonnodular patches, whereby its clinical usability is compromised.

The objective of this research is to determine the effects of size on the CNN architecture for classification lung nodules in patch-based CT images. The goals include identifying the best batch size that offers a trade-off between computational efficiency and high accuracy in classification, minimizing false positives and negatives on nodule detection. In attaining these objectives, the study aims to develop a more accurate and cost-effective CNN based Computer Aided Diagnosis (CAD) systems that can be easily integrated into clinical workflows for early detection or lung cancer. Hence, improving patient outcomes as well allocation of health care resources was also implied.

The structure of the paper is as follows: Section 2 is the literature review that can be considered a starting point of research to understand the problems. Section 3 methodology analyses the experimental design and data analysis. Section 4 discusses the findings in detail then concludes by an implication discussion. Lastly Section 5 ends with conclusion and future exploration.

2 Literature Review

Several methods have been proposed for classifying lung nodules. However, there is a need for a method that can reliably identify a malignant tumor, thereby reducing the possibility of a wrong diagnosis. Deep reinforcement learning [8], generative adversarial networks [9], and CNNs [10, 11] are highlighted as effective deep learning architectures. Among them, CNN has performed better than other DL architectures. To extract the most effective features for classification, most machine learning algorithms must first examine the connection between the data and the class label. Choosing appropriate features is crucial to the success of a classification system [12]. However, CNNs use a sequential approach to feature extraction and classification. Furthermore, CNN [13] has demonstrated the highest performance in the classification of biomedical images. There are several advantages of using CNN to determine whether lung nodules [14] are malignant. CNN has shown better results than most traditional models at identifying these tumors [15]. To classify lung nodules, CNN architecture's convolution, pooling, and fully connected layer combine the feature extraction and classification phases into a single step. Since CNN [16] is more effective than other deep learning architectures for classifying lung nodules, researchers are primarily interested in refining this particular architecture. The classification of biomedical images using CNN features has improved over that using manually crafted features such as histogram, texture, etc. [17]. Early identification is essential in the process of diagnosing carcinoma and can enhance one's chances of surviving the disease over the long term [18]. Because of this, research on the identification and classification of lung cancer has developed into a significant field in recent years. CNNs have been used in several studies for lung cancer classification and detection to establish a dependable procedure. This section will provide an overview of a few. Deep residual networks were used in the method that was proposed by Bhatia et al. [19] to detect lung cancer and extract features. The UNet and ResNet models are used to extract features, and these features are then given into a variety of classifiers. Additionally, XGBoost and Random Forest, in addition to the individual forecasts, can predict the likelihood that a CT scan will reveal malignancy. The accuracy of the research work is determined to be 84% when applied to the Lung Image Database Consortium and the Image Database Resource Initiative (LIDC-IDRI) dataset.

Kriegsmann et al. [20] investigated the various types of lung carcinoma in connection via the University Clinic Heidelberg. The authors received support from the tissue bank of the National Center of Tumor Diseases, which curated, digitised, annotated, and extracted image patches from the Institute of Pathology Archive for 30 skeletal muscles to serve as controls. The authors investigated multiple configurations of CNN architectures for the purpose of classification. They asserted that the InceptionV3 CNN architecture, which was optimised, yielded the highest accuracy in classification among all the configurations that were tested. Dou et al. [21] came up with a novel strategy for the automatic detection of pulmonary nodules using volumetric CT scans. Their method makes use of 3D CNN to cut down on the number of false positives. The LUNA16 Challenge involved the analysis of a dataset [22], and it was successful in achieving the highest possible score (0.827) on the competition's competition performance metric.

3 Methodology

3.1 Dataset

In this work, experiments were conducted for both training and evaluation using data from the LIDC-IDRI dataset [23]. There are 1018 cases in the LIDC-IDRI, all of which are thoracic CT scans for lung cancer screening with annotated lesions.

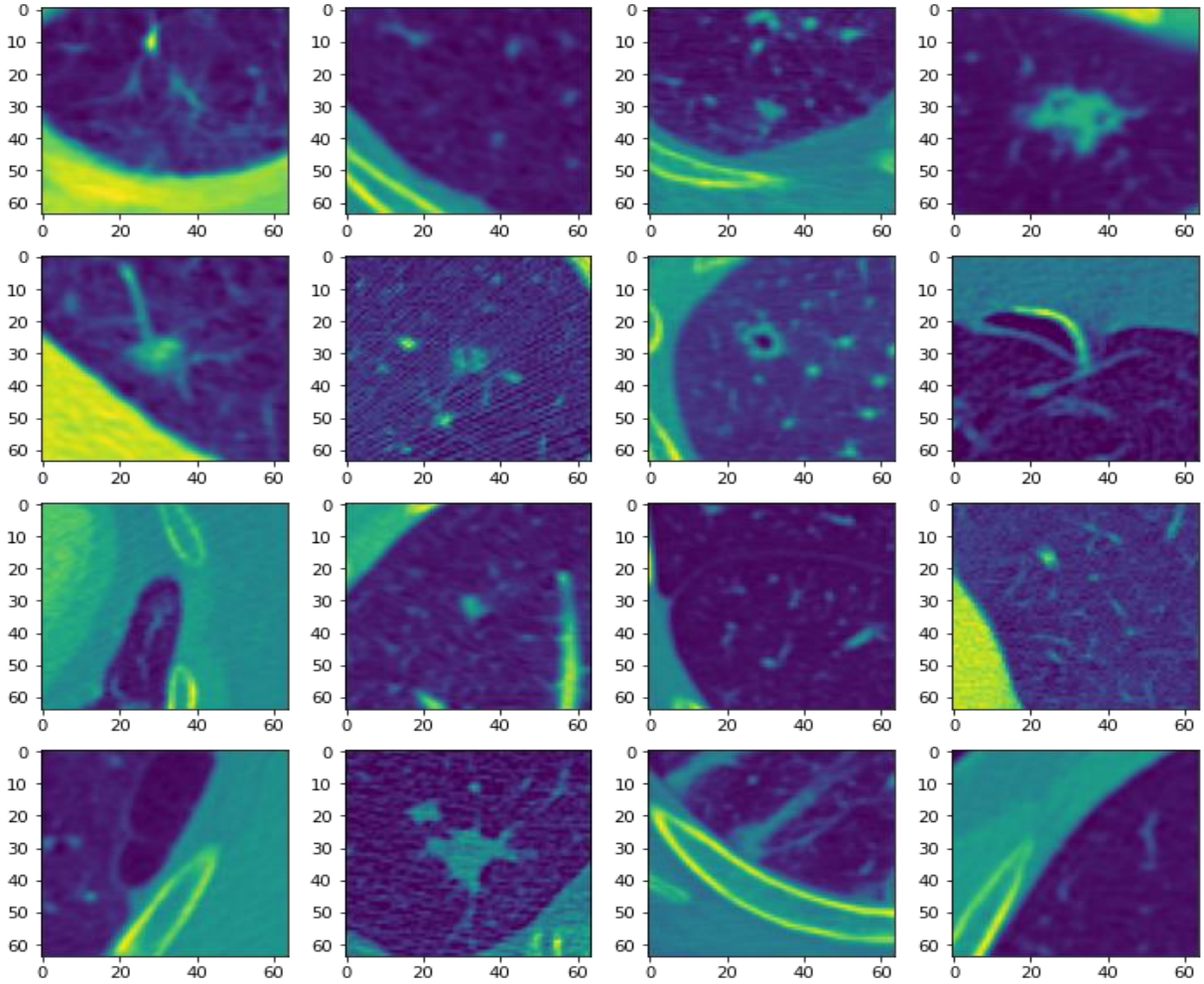


Fig. 1 Samples of patch-based lung nodules used in the proposed CNN architecture (Here X and Y axes represent image size in pixels).

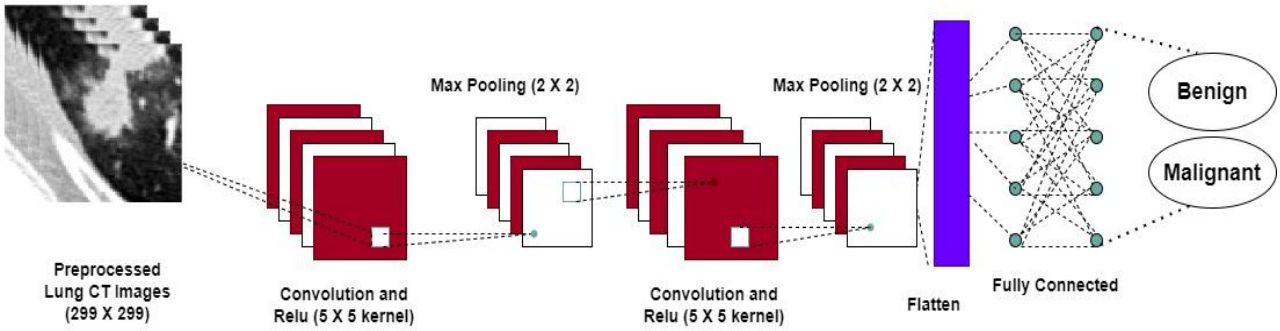


Fig. 2 Architecture of the proposed CNN model for the classification of patch based lung nodules.

These lesions were classified into three groups by size and by four experienced radiologists namely nodule 3 mm, nodule > 3mm andnon-nodule [24].

Each of the four radiologists tagged each nodule with information about its texture, malignancy, and calcification, and this information is included in an XML file that is attached to each patient's file. The 512 × 512 pixel images, with 65 to 764 slices, are all in line with the Digital Imaging and Communications in Medicine (DICOM) standard for medical imaging.

The scanned data is divided into two groups such as training and testing to assess the effectiveness of the proposed CNNs' architecture more accurately. The weights of the convolutional, fully connected, and softmax layers were all updated based on the training set. Hyper-parameters like the learning rate, the number of kernels, and kernel size of each unit, were all adjusted using the validation set. Each component of the CAD system, including the CNN, was put through its paces using the testing set to determine their performance.

Table 1 Proposed CNN parameters for the classification of patch-based lung nodules.

Parameters	Value
Input Image Dimension	(64, 64, 3)
Kernel Size	3 × 3
Max Pooling	2 × 2
Activation Functions	ReLU, Sigmoid
Optimizer	Adam
Epochs	50
Loss Function	Categorical Cross entropy

The LUNA16 [25] competition provided some of the pre-processed data sets used in this research and its samples are shown in Fig. 1. It is made up of 6691 different images and their respective classes.

3.2 Proposed CNN Architecture

The CNN learns to map a given image into its corresponding category by identifying some abstract features. The complexity increases when the number of detected features increases [26]. The network then makes use of these distinguishing characteristics to predict the appropriate image category [27]. Normalization, convolution, activation, pooling, fully connected layers, and a classifier are the fundamental functionalities in the proposed CNN architecture as shown in Fig. 2.

As per the original data [9], the convolutional layer is considered as the central processing unit of the neural network, responsible for executing the convolution operation on the input image in case the input layer or the feature map obtained from the preceding layers. The pooling layer is a technique for down sampling that aids in achieving spatial invariance after a convolution layer. The techniques of pooling that employ the highest and mean values are denoted as “max” and “average” pooling, correspondingly. All activation functions utilised by the nodes in the convolutional layer are non-linear in nature. Non-linear mapping is a powerful technique that enables the conversion of data that is intrinsically incomparable along a linear axis into data that can be more readily classified along a linear axis.

The output stage of the process involves the incorporation of one or more fully connected layers, which serve the purpose of classifying the input data. The flattened input is fed into the fully connected layer to enable its propagation to every neuron. The Softmax Classifier serves as the ultimate activation function in a neural network by allotting decimal probabilities to each class in a multiple-class problem.

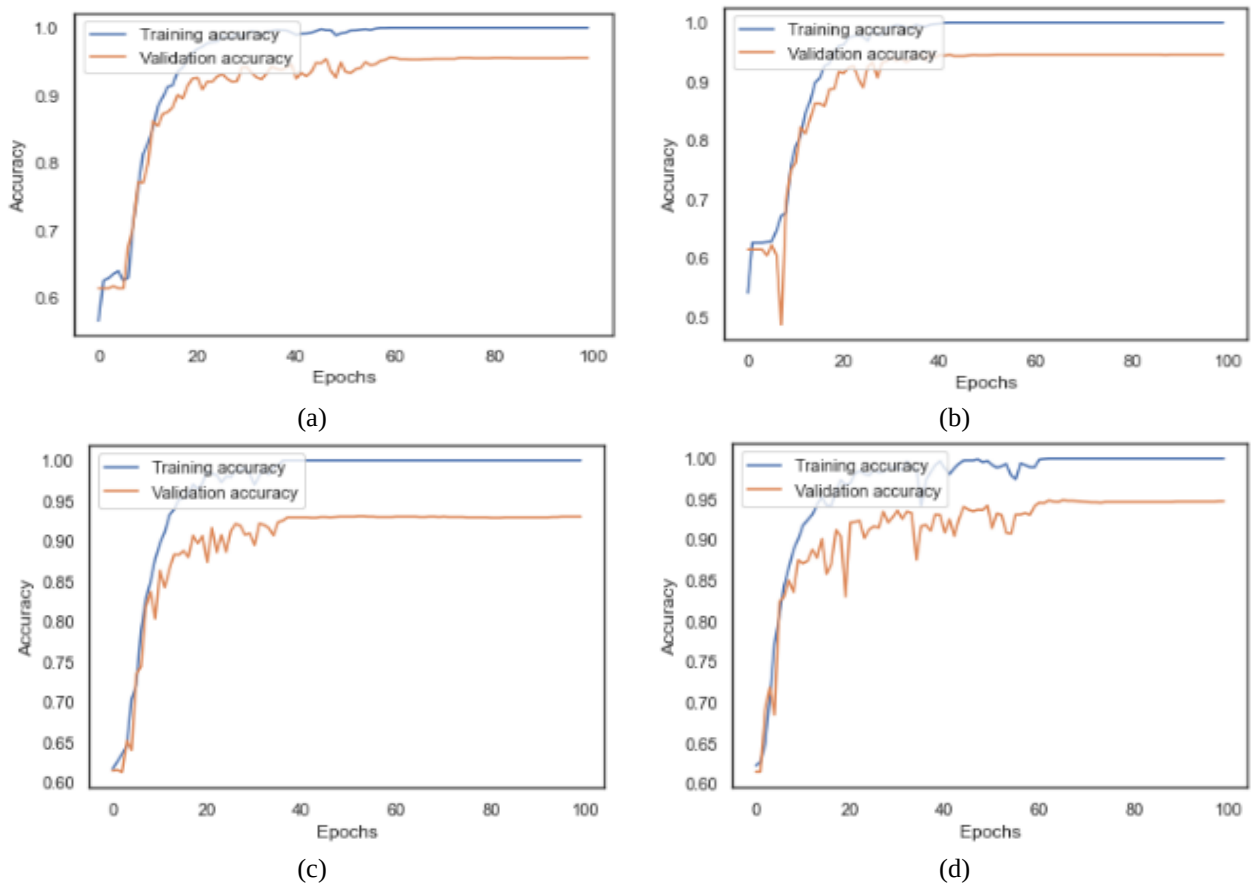


Fig. 3 Training and validation accuracy curve for the classification of patch based lung nodules (a) 32-batch size, (b) 64-batch size, (c) 256-batch size, and (d) 512-batch size.

3.3 Experimental Setup

The proposed CNN architecture comprises ten convolutional layers in two dimensions, six Max-pooling layers, three fully connected layers, and one flattening layer. The activation functions employed are ReLu and Sigmoid. Experiment-specific parameter values are listed in Table 1.

4 Experimental Results and Discussion

4.1 Experimental Setup

The experiments were conducted on a GPU NVIDIA-MX450, an i5-1135G7 processor, and Windows, and utilized Python libraries like Keras and TensorFlow for the pre-processing stage, Augmentation, and CNN. From the Kaggle dataset, lung nodule patches were extracted and split in the ratio of 67:33 for training and evaluation purposes. There were 4482 lung CT images in the training datasets, and 2209 CT images in the testing datasets. The present study examines the performance parameters, namely accuracy, precision, recall, and F_1-score, of the proposed CNN architecture when applied to lung nodule detection from images. The study examined the impact of varying batch sizes, specifically 32, 64, 256, and 512, on the architecture of deep learning.

The findings indicate that there is a positive correlation between batch size and accuracy, with the highest accuracy observed at a batch size of 256. However, a decrease in performance has been observed for a batch size of 512. A 96% accuracy rate is an excellent result for the CNN model. Table 2 summarizes the various metrics, such as accuracy, recall, precision, and F_1-score, that were investigated in this work to measure overall performance. Training and validation accuracy and loss curves are shown in Fig. 3 and Fig. 4 respectively. It follows that when the total number of epochs increases, the accuracy improves while the loss goes down.

Table 2 Confusion matrix of CNN architecture with different batch sizes for the classification of patch based lung nodules.

Batch-Size	TP	TN	FP	FN
32	760	1295	63	91
64	776	1317	41	75
256	784	1327	31	67
512	775	1314	44	76

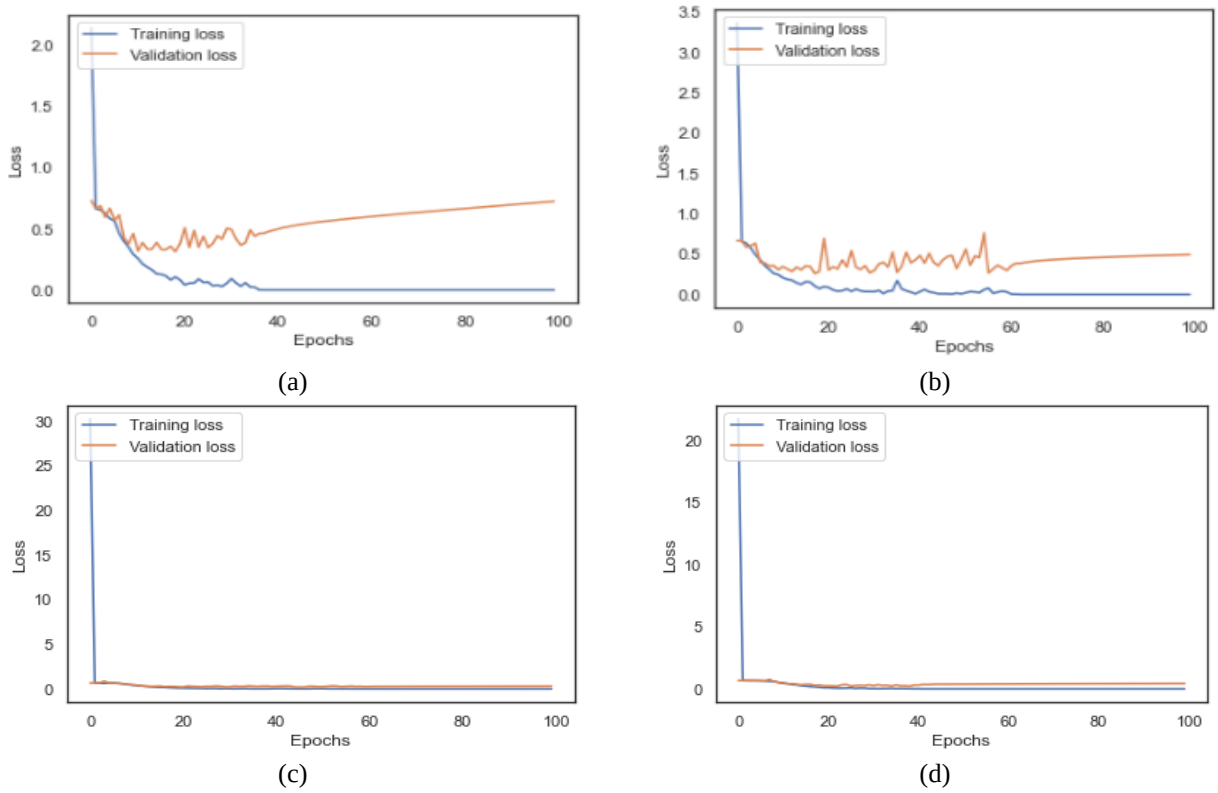


Fig. 4 Training and validation loss curve for the classification of patch based lung nodules (a) 32-batch size, (b) 64-batch size, (c) 256-batch size, and (d) 512-batch size.

While Fig. 3 shows the training and validation accuracy curve for different batch sizes, Fig. 4 describes the accuracy and validation loss curve for batch sizes of 32, 64, 256, and 512.

Table 2 depicts the confusion matrix of the proposed CNN architecture obtained for the identification of lung cancer, with different batch sizes. In Table 2 the term batch size refers to the quantity of data samples that are processed in a single iteration during the training phase. True positive (TP) denotes the instances where a CNN successfully identifies lung cancer cases as positive, meaning the model correctly detects the malignancy in lung cancer.

The term true negative (TN) refers to the quantity of instances in which the CNN architecture accurately identified non-lung cancer cases as negative. These occurrences pertain to individuals who were accurately recognised as negative for lung carcinoma. The false positives (FP) metric denotes the count of instances where non-lung cancer cases were erroneously identified as positive. The instances mentioned above pertain to individuals who were erroneously diagnosed with lung cancer despite the absence of the disease. The term false negatives (FN) refers to instances where the CNN architecture misclassified lung cancer cases as negative. These occurrences pertain to individuals who were erroneously classified as negative for lung cancer despite the presence of the disease. Formulae for accuracy, precision, recall, F_1-score are illustrated in Eqs. (1)–(4).

$$Accuracy = \frac{TP+TN}{TP+TN+FP+FN}, \quad (1)$$

$$Precision = \frac{TP}{TP+FP}, \quad (2)$$

$$Recall = \frac{TP}{TP+FN}, \quad (3)$$

$$F_1 score = \frac{2*Precision*Recall}{Precision+Recall}. \quad (4)$$

Given a batch size of 32, the proposed CNN accurately detected 760 instances of true positive cases. The dataset comprised 1295 instances of true negative cases. The study identified a total of 63 instances of false positive cases, indicating that a few patients who did not have lung cancer were erroneously categorized as positive. Finally, the study identified 91 instances of false negatives. The area under the curve (AUC) is used to evaluate the efficacy of a binary classification model. A higher AUC value suggests superior discrimination and overall model performance. When it comes to differentiating between positive and negative instances in lung nodule detection, the CNN model demonstrates strong AUC values across all batch sizes. An AUC of 99 is reached with a batch size of 256, demonstrating excellent discrimination by the model at that point in time. The AUC values for the receiver operating characteristic (ROC) curves of the CNN model for different batch sizes are shown in Fig. 5.

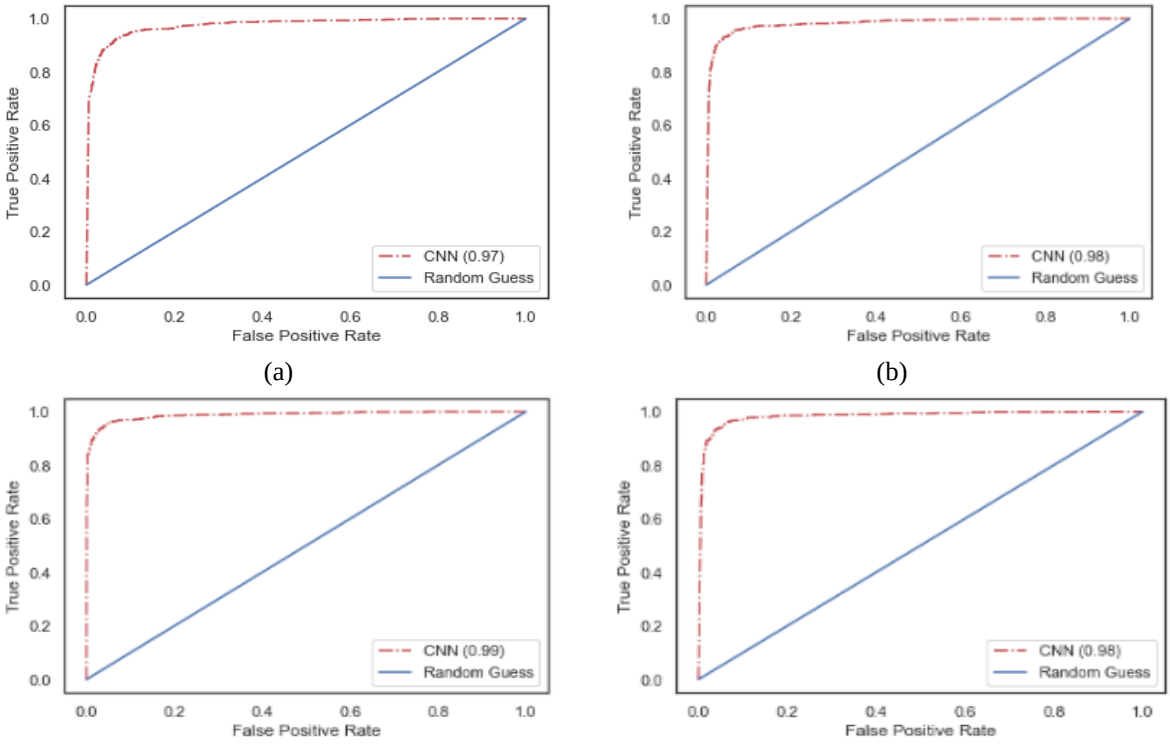


Fig. 5 AUC-curve for the classification of patch based lung nodules: (a) 32-batch size, (b) 64-batch size, (c) 256-batch, size, and (d) 512-batch size.

Table 4 An Ablation study of different convolutional features of proposed CNN model with a batch size of 256.

Ablated Layer	Accuracy (%)	Precision (%)	Recall (%)	F_1-score (%)
Conv2D (512)	95.29	91.54	96.05	97.73
Conv2D (256)	94.70	91.14	94.84	92.95
Conv2D (128)	95.02	90.96	95.91	93.36

Table 5 Performance comparison of proposed method with state-of-the-art architecture for the classification of patch based lung nodules.

Author(s)	Architecture	Accuracy (%)	Precision (%)	Recall (%)	F_1-score (%)
Zhang et al. [28]	DenseNet121	87.77	87.88	80.93	–
Karthika et al. [29]	CNN	80.66	92.59	83.33	87.71
Shafi et al. [30]	CNN+SVM	94.00	95.00	94.50	94.50
Khodabakhshi et al. [31]	Multivariate Adaptive Regression	86.50	71.00	70.30	70.60
Proposed Work	Patch-Based CNN	96.00	95.50	95.00	95.00

Table 3 shows the overall accuracy of CNN model obtained is 95% for batch size 64 and data type benign, suggesting that 95% of the occurrences (both benign and malignant) in this batch were properly identified. For non-threatening conditions, the accuracy is 95%. This means that 95% of the time, the cases were accurately labelled as benign. In circumstances where there is no harm done, 97% of patients are recalled. This means that 97% of truly benign situations were accurately identified by the model. For non-malignant conditions, the F_1-score is 96%. This score incorporates both accuracy and reliability to provide a comprehensive evaluation of harmless-classification efficiency. For malignant data with batch size of 64 has an overall accuracy of 95%. Accuracy for cancer diagnoses is 95%. Malignant cases have a 91% recall rate and F_1-score is 93%.

4.2 Ablation Study

Three experiments were conducted in the ablation study of a CNN model with 256 batch size by eliminating different Conv2D layers that contained different features as presented in Table 4. The findings revealed that eliminating the 512-feature, the Conv2D layer had little effect on accuracy as precision and recall remained high. The removal of the Conv2D layer with 256 features resulted in a moderate loss of accuracy but still ensured good precision and recall rates. Removing the Conv2D layer containing 128 features increased the accuracy by sacrificing a little bit of precision. These results demonstrate the relative stability of the model to removal of some features, providing information about feature importance for accuracy, precision, and recall.

The proposed CNN model demonstrates the superiority over the existing state-of-the-art architectures in the lung cancer classification task, providing an Accuracy of 96%, which is the highest among the compared methods is shown in Table 5. It shows a balanced performance considering precision and recall rates of 95.5% and 95% respectively.

The results from Shafi et al. [30], combined CNN and Support Vector Machine (SVM), with a comparable balance across metrics, reaching 94% accuracy. The traditional architectures such as DenseNet121 [28] and basic CNNs used by Zhang et al. [28] and Karthika et al. [29] proved to be less effective in this case. The comparison emphasizes the potential of the proposed CNN approach in enhancing diagnostic accuracy for lung cancer.

5 Conclusion

This paper presented a deep learning-based approach to pulmonary nodule detection using CNNs for different batch sizes. The research focusing on the classification of benign and malignant nodules from CT scan images. The proposed system consists of two main components namely, the extraction of relevant patches from CT images and the subsequent application of a CNN to classify these patches, aiming to assist in the diagnosis of pulmonary nodules. Utilizing CT images for lung carcinoma detection, the proposed approach demonstrated promising results, achieving an overall accuracy of 96% with a batch size of 256. However, it is important to acknowledge that the performance of the model, particularly in the identification of malignant nodules, is constrained by the limited size of the available training dataset. This limitation underscores the need for access to larger and more diverse datasets to enhance the model's diagnostic capabilities.

The adaptability of the deep learning architectures used in this study suggests the possibility of extending this approach to the detection and diagnosis of other lung diseases, provided that sufficient training data is

available. By expanding the scope and scale of the training datasets, future work can explore the full potential of deep learning techniques in improving diagnostic processes for a wider range of pulmonary conditions. Another promising avenue is the exploration of more advanced deep learning architectures and techniques, such as Generative Adversarial Networks (GANs) for data augmentation, or few-shot learning approaches, which could offer new ways to overcome the challenges of limited training data.

Acknowledgement

There is no scholarship or grant programme that would apply to this work. The author has provided all the necessary components for the experiment. The author would like to express gratitude to their loved ones for their support throughout the research process.

Disclosures

The authors state no conflict of interest.

References

1. M. F. Abdullaha, S. N. Sulaimana, M. K. Osmana, N. K. A. Karimc, S. Setumina, I. S. Isaa, and A. I. C. Ania, "Geometrical feature of lung lesion identification using computed tomography scan images," Jurnal Teknologi 85(2), 149–156 (2023).
2. X. Li, L. Shen, and S. Luo, "a solitary feature-based lung nodule detection approach for chest x-ray radiographs," IEEE Journal of Biomedical and Health Informatics 22(2), 516–524 (2018).
3. D. Riquelme, M. Akhloufi, "Deep learning for lung cancer nodules detection and classification in ct scans," Ai 1(1), 28–67 (2020).
4. N. Horeweg, C. M. van der Aalst, R. Vliegenthart, Y. Zhao, X. Xie, E. T. Scholten, W. Mali, E. Thunnissen, C. Weenink, H. J. M. Groen, J.-W. J. Lammers, K. Nackaerts, J. van Rosmalen, M. Oudkerk, and H. J. de Koning, "Volumetric computed tomography screening for lung cancer : three rounds of the NELSON trial," European Respiratory Journal 42(6), 1659–1667 (2013).
5. J. Li, Z. Chen, "Integrated intravascular ultrasound and optical coherence tomography technology: a promising tool to identify vulnerable plaques [INVITED PAPER]," Journal of Biomedical Photonics & Engineering 1(4), 209–224, (2015).
6. A. R. Bushara, R. S. V. Kumar, and S. S. Kumar, "An ensemble method for the detection and classification of lung cancer using Computed Tomography images utilizing a capsule network with Visual Geometry Group," Biomedical Signal Processing and Control 85, 104930 (2023).
7. M. Vijayalakshmi, V. J. Peter, "CNN based approach for identifying banana species from fruits," International Journal of Information Technology 13(1), 27–32 (2021).
8. X. Wang, S. Wang, X. Liang, D. Zhao, J. Huang, X. Xu, B. Dai, and Q. Miao, "Deep reinforcement learning : a survey," IEEE Transactions on Neural Networks and Learning Systems, 1–15 (2022).
9. A. Creswell, T. White, V. Dumoulin, K. Arulkumaran, B. Sengupta, and A. A. Bharath, "Generative adversarial networks: an overview," IEEE Signal Processing Magazine 35(1), 53–65 (2018).
10. A. Patil, M. Rane, "Convolutional neural networks: an overview and its applications in pattern recognition," Information and Communication Technology for Intelligent Systems. ICTIS 2020. Smart Innovation, Systems and Technologies, T. Senjyu, P. N. Mahalle, T. Perumal, A. Joshi (Eds.), 195, Springer, Singapore, 21–30 (2021).
11. R. Singh, S. Saurav, T. Kumar, R. Saini, A. Vohra, and S. Singh, "Facial expression recognition in videos using hybrid CNN & ConvLSTM," International Journal of Information Technology 15(4), 1819–1830 (2023).
12. B. V. Grechkin, V. O. Vinikurov, Y. A. Khristoforova, and I. A. Matveeva, "VGG convolutional neural network classification of hyperspectral images of skin neoplasms," Journal of Biomedical Photonics & Engineering 9(4), 040304 (2023).
13. B. Ar, "A deep learning-based lung cancer classification of ct images using augmented convolutional neural networks," ELCVIA Electronic Letters on Computer Vision and Image Analysis 21(1), 130–142 (2022).
14. Y. Gu, J. Chi, J. Liu, L. Yang, B. Zhang, D. Yu, Y. Zhao, and X. Lu, "A survey of computer-aided diagnosis of lung nodules from CT scans using deep learning," Computers in Biology and Medicine 137, 104806 (2021).
15. P. Tiwari, B. Pant, M. M. Elarabawy, M. Abd-Elnaby, N. Mohd, G. Dhiman, and S. Sharma, "CNN based multiclass brain tumor detection using medical imaging," Computational Intelligence and Neuroscience 2022, 1830010 (2022).
16. S. Lamba, A. Baliyan, and V. Kukreja, "A novel GCL hybrid classification model for paddy diseases," International Journal of Information Technology 15(2), 1127–1136 (2023).
17. T. Saba, "Computer vision for microscopic skin cancer diagnosis using handcrafted and non-handcrafted features," Microscopy Research and Technique 84(6), 1272–1283 (2021).
18. H. F. Al-Yasriy, M. S. Al-Husieny, F. Y. Mohsen, E. A. Khalil, and Z. S. Hassan, "Diagnosis of lung cancer based on CT scans using CNN," IOP Conference Series: Materials Science and Engineering 928(2), 022035 (2020).

19. S. Bhatia, Y. Sinha, and L. Goel, "Lung cancer detection: A deep learning approach," Soft Computing for Problem Solving. Advances in Intelligent Systems and Computing, J. Bansal, K. Das, A. Nagar, K. Deep, A. Ojha (Eds.), vol 817, Springer, Singapore, 699–705 (2019).
20. M. Kriegsmann, C. Haag, C. A. Weis, G. Steinbuss, A. Warth, C. Zgorzelski, T. Muley, H. Winter, M. E. Eichhorn, F. Eichhorn, J. Kriegsmann, P. Christopoulos, M. Thomas, M. Witzens-Harig, P. Sinn, M. von Winterfeld, C. P. Heussel, F. J. F. Herth, F. Klauschen, A. Stenzinger, and K. Kriegsmann, "Deep learning for the classification of small-cell and non-small-cell lung cancer," Cancers 12(6), 1604 (2020).
21. Q. Dou, H. Chen, L. Yu, J. Qin, and P. A. Heng, "Multilevel contextual 3-d cnns for false positive reduction in pulmonary nodule detection," IEEE Transactions on Biomedical Engineering 64(7), 1558–1567 (2017).
22. P. Afshar, A. Oikonomou, F. Naderkhani, P. N. Tyrrell, K. N. Plataniotis, K. Farahani, and A. Mohammadi, "3D-MCN: A 3D Multi-scale Capsule Network for Lung Nodule Malignancy Prediction," Scientific Reports 10(1), 7948 (2020).
23. S. G. Armato III, G. McLennan, L. Bidaut, M. F. McNitt-Gray, C. R. Meyer, A. P. Reeves, B. Zhao, D. R. Aberle, C. I. Henschke, E. A. Hoffman, E. A. Kazerooni, H. MacMahon, E. J. R. van Beek, D. Yankelevitz, A. M. Biancardi, P. H. Bland, M. S. Brown, R. M. Engelmann, G. E. Laderach, D. Max, R. C. Pais, D. P.-Y. Qing, R. Y. Roberts, A. R. Smith, A. Starkey, P. Batra, P. Caligiuri, A. Farooqi, G. W. Gladish, C. M. Jude, R. F. Munden, I. Petkovska, L. E. Quint, L. H. Schwartz, B. Sundaram, L. E. Dodd, C. Fenimore, D. Gur, N. Petrick, J. Freymann, J. Kirby, B. Hughes, A. Vande Casteele, S. Gupte, M. Sallam, M. D. Heath, M. H. Kuhn, E. Dharaiya, R. Burns, D. S. Fryd, M. Salganicoff, V. Anand, U. Shreter, S. Vastagh, B. Y. Croft, and L. P. Clarke, "The lung image database consortium (lidc) and image database resource initiative (idri): a completed reference database of lung nodules on ct scans," Medical Physics 38(2), 915–931 (2011).
24. A. R. Bushara, R. S. V. Kumar, and S. S. Kumar, "LCD-capsule network for the detection and classification of lung cancer on computed tomography images," Multimedia Tools and Applications 82, 37573–37592 (2023).
25. A. A. A. Setio, A. Traverso, T. de Bel, M. S. N. Berens, C. van den Bogaard, P. Cerello, H. Chen, Q. Dou, M. E. Fantacci, B. Geurts, R. van der Gugten, P. A. Heng, B. Jansen, M. M. J. de Kaste, V. Kotov, J. Y.-H. Lin, J. T. M. C. Manders, A. Sóñora-Mengana, J. C. García-Naranjo, E. Papavasileiou, M. Prokop, M. Saletta, C. M. Schaefer-Prokop, E. T. Scholten, L. Scholten, M. M. Snoeren, E. L. Torres, J. Vandemeulebroucke, N. Walasek, G. C. A. Zuidhof, B. van Ginneken, and C. Jacobs, "Validation, comparison, and combination of algorithms for automatic detection of pulmonary nodules in computed tomography images: The LUNA16 challenge," Multimedia Tools and Applications 42, 1–13 (2017).
26. A. R. Bushara, R. S. V. Kumar, and S. S. Kumar, "Classification of benign and malignancy in lung cancer using capsule networks with dynamic routing algorithm on computed tomography images," Journal of Artificial Intelligence and Technology 4(1), 40–48 (2024).
27. N. Khehrah, M. S. Farid, S. Bilal, and M. H. Khan, "Lung nodule detection in CT images using statistical and shape-based features," Journal of Imaging 6(2), 6 (2020).
28. Q. Zhang, H. Wang, S. W. Yoon, D. Won, and K. Srihari, "Lung nodule diagnosis on 3D computed tomography images using deep convolutional neural networks," Procedia Manufacturing 39, 363–370 (2019).
29. M. S. Karthika, H. Rajaguru, and A. R. Nair, "Evaluation and exploration of machine learning and convolutional neural network classifiers in detection of lung cancer from microarray gene – a paradigm shift," Bioengineering 10(8), 933 (2023).
30. I. Shafi, S. Din, A. Khan, I. D. L. T. Díez, R. J. P. Casanova, K. T. Pifarre, and I. Ashraf, "An effective method for lung cancer diagnosis from ct scan using deep learning-based support vector network," Cancers 14(21), 5457 (2022).
31. Z. Khodabakhshi, S. Mostafaei, H. Arabi, M. Oveisi, I. Shiri, and H. Zaidi, "Non-small cell lung carcinoma histopathological subtype phenotyping using high-dimensional multinomial multiclass CT radiomics signature," Computers in Biology and Medicine 136, 104752 (2021).

Photobiomodulation at 660 nm Modifies Apoptosis Regulators Bcl-2 and Caspase-3 in Diabetic Wounded Cell Models *in Vitro*

Sandy Winfield Jere*and Nicolette Nadene Houreld
Laser Research Centre, Faculty of Health Sciences, University of Johannesburg, P.O. Box 17011, Doornfontein 2028, South Africa

***e-mail:** sandyj@uj.ac.za

Abstract. While it has been identified that photobiomodulation (PBM) improves hyperglycaemic impaired cutaneous wound healing, there is insufficient knowledge about the cellular mechanism involved. During the normal wound healing process, apoptosis is fundamental for the elimination of inflammatory cells and scar formation. Under diabetic conditions there is increased apoptosis, making the wound susceptible to infection and delayed healing due to a persistent inflammatory state. This study examined the assumption that PBM at 660 nm modifies apoptosis regulators Bcl-2 and caspase 3 in diabetic wounded cell models *in vitro*. WS1 skin fibroblasts were modelled into normal (N), wounded (W), and diabetic wounded (DW), and were irradiated at a wavelength of 660 nm and a fluence of 5 J/cm^2. Non-irradiated cells (0 J/cm^2) were employed as controls. Following 48 h of incubation, cells were evaluated for morphology, percentage migration rate, wound closure, viability (trypan blue and MTT), and apoptosis (Caspase 3/7, Bcl-2, and Annexin V/PI). PBM at 660 nm significantly increased cell migration, wound closure and viability, and reduced apoptosis in DW cells. PBM at 660 nm and 5 J/cm^2 increases cell viability and *in vitro* diabetic wound healing through the reduction of apoptosis by diminishing caspase activity and increasing the release of Bcl-2. © 2024 Journal of Biomedical Photonics & Engineering.

Keywords: fibroblasts; photobiomodulation; wound; apoptosis; Bcl-2; caspase; diabetes mellitus; laser therapy.

Paper #9043 received 1 Dec 2023; revised manuscript received 17 Dec 2023; accepted for publication 18 Dec 2023; published online 10 Mar 2024. doi: 10.18287/JBPE24.10.010306.

1 Introduction

The wound healing process requires the combination of complicated molecular and cellular events that take place in succeeding phases of inflammation, formation of granulation tissue, and remodelling. In the first phase, inflammatory cells including neutrophils infiltrate the wound to eliminate debris and avoid infection [1]. The inflammatory phase is followed by the formation of granulation tissue, and is characterised by fibroblast and endothelial cell proliferation. Regulated by inflammatory factors, fibroblast cells migrate to the fibrin clot, proliferate and facilitate angiogenesis and the construction of granulation tissue. The presence of fibroblast cells supports migration of other cells involved in the healing process by producing matrix metalloproteinases (MMPs) and extracellular matrix (ECM) proteins. Towards the beginning of the remodelling phase, fibroblast cells, stimulated by C-X-C Motif Chemokine Ligand 8 (CXCL8) and transforming growth factor-β (TGF-β), differentiate into myofibroblasts, critical cells involved in the remodelling phase [2, 3]. This phase mainly involves structural adjustment of the deposited collagen and development of the stretchy and tensile strength of the wound. Thus, fibroblast cell viability, proliferation, and migration is

critical in a standard cutaneous wound healing process [1].

In diabetes mellitus (DM), advanced glycation end products (AGEs) trigger apoptosis due to the increased presence of reactive oxygen species (ROS). AGEs are formed as a consequence of glucose-protein concentration, which when increased affect wound healing and remodelling [4, 5]. Cellular caspases are a frequently activated death protease, catalysing the precise cleavage of several key intracellular proteins [6, 7]. The mitochondrial or intrinsic pathway for apoptosis is triggered by a diversity of inducements including hypoxia and oxidative stress, resulting in mitochondrial outer membrane permeabilisation and discharge of apoptogenic cytochrome c into the cytoplasm to form an apoptosomal complex which activates the effector caspases -3 and -7 to induce apoptosis [8]. On the other extreme, B cell lymphoma 2 (Bcl-2), the most distinctive anti-apoptotic protein, obstructs apoptosis by creating a heterodimer with BAX (Bcl-2-like protein 4), thereby controlling the concentration and antioxidant effect of ionized calcium, and the activities of caspase-3 and -7 [9].

DM is a systemic condition resulting from insulin deficiency or loss of responsiveness in its target tissue, resulting in hyperglycaemia [5]. It impairs the wound healing process including defects in the inflammatory response, and raised fibroblast cell apoptosis. Literature shows that the mechanism of diminished diabetic wound healing is related to increased apoptosis and reduced viability of fibroblast cells [10, 11]. According to the 2021 International Diabetes Federation (IDF) Diabetes Atlas [12], approximately 540 million adults aged between 20 and 79 years are living with DM, and this number is expected to rise to approximately 645 million before 2030 and 784 million before 2045. Patients with DM have a 25% lifetime risk for developing a chronic diabetic wound of the foot, and approximately between 14% and 24% of these patients may require a major or minor non-traumatic limb amputation, mostly due to acute gangrene [13].

There are several treatment methods for diabetic wounds with each method having its own efficacy short falls. Photobiomodulation (PBM) is a new treatment method used for the treatment of diabetic wounds, and its benefits have been demonstrated to be significant in reducing acute pain, amendment of tissue scars, and improving cellular proliferation and generation of viable cells [14, 15]. Mitochondria are the basic site for the primary effects of PBM, leading to raised production of adenosine triphosphate (ATP), alteration of ROS, and stimulation of transcription factors, leading to raised fibroblast cell proliferation, viability, and migration [16]. In the mitochondria, photons are absorbed by components of the respiratory chain, mainly complex IV or cytochrome c oxidase (COX), which moves electrons to form molecular oxygen [17].

PBM therapy is known to regulate healing activities in diabetic wounds. However, the mechanism by which these activities are affected is not completely understood. This investigation examined the assumption that 660 nm PBM reduces apoptosis by increasing the release of Bcl-2 and reducing caspase activity in diabetic wounded fibroblast cells *in vitro* to gain new insights into mechanisms by which PBM induces wound healing in DM.

2 Materials and Methods

American Type Culture Collection WS1 human skin fibroblast cells (ATCC®, CRL-1502™) were cultured using standard culture procedures. Three models were used, namely normal (N), wounded (W), and diabetic wounded (DW). An *in vitro* diabetic cell model was realised by uninterruptedly cultivating WS1 cells in minimum essential medium eagle (MEM) with a basal glucose concentration of 5.6 mM, to which an extra 17 mM D-glucose was added, giving a final glucose concentration of 22.6 mM, thus mimicking a hyperglycaemic condition [18]. Cells (6×10^5) were seeded in 3.4 cm diameter tissue culture plates and incubated for 24 h at 37 °C in 5% CO_2 for attachment, after which a wounded cell model was created using the central scratch assay performed on a confluent monolayer and incubated for 30 min pre-irradiation. A central scratch assay creates a cell free zone bordered by cells on both sides of the "wound" [19]. After 30 min incubation, cell culture plates, with the lids off, were subjected to laser light from above in the dark and incubated for 48 h before detachment using 300 µL of TrypLE™ Select (Life Technologies, Gibco, 12563-029). All cell models were analysed for cell morphology, and the percentage migration rate and wound closure in wounded cell models (W and DW) using an inverted light microscope and the analySIS getIT software. All cell models were assessed for viability using the Trypan blue and 3-(4,5-dimethylthiazol-2-yl)-2,5-diphenyl tetrazolium bromide (MTT) assays, and apoptosis using the Caspase-Glo® 3/7 assay for caspase activity, enzyme linked immunosorbent assay (ELISA) for the release of Bcl-2, and Annexin V/PI–fluorescein isothiocyanate (FITC) and propidium iodide (PI) to categorise membrane phosphatidyl serine in apoptotic cells and membrane damage in necrotic cells. Table 1 displays the laser parameters utilised in this study. Non-irradiated cells were used as controls. All experiments were analysed in duplicate, and were repeated three times ($n = 3$).

2.1 Cell Morphology and the Percentage Migration Rate

In this study, the percentage migration rate and wound closure were analysed by measuring the distance between the borders of the "wound" at 3 specific points marked on the culture dishes and using the graduated locator marks on the mechanical stage for easy return to the area for observation. The results were calculated as the percentage migration rate per point using the following Eq.:

$$(At_{0h} - At_{time})/At_{0h} \times 100,$$

where At_{0h} is the distance between the borders of the "wound" at 0 h, and At_{time} is the distance between the borders of the "wound" at 48 h [20–22]. The average rate of the points was used to get the average percentage of the 3 repeats (n = 3).

Table 1 Laser parameters.

Light source	Diode laser
Wavelength (nm)	660
Emission	Continuous wave
Power output (mW)	101
Power density (mW/cm^2)	11
Spot size (cm^2)	9.1
Energy density (J/cm^2)	5
Irradiation time	7 min 35 s
Energy (J)	46

2.2 Cell Viability

2.2.1 Trypan Blue

To establish the number of viable and healthy cells present in each cell model, the Trypan blue (Sigma-Aldrich, T8154) exclusion assay was used. Cells were detached using TrypLE™ Select, suspended in 1 mL pre-warmed Hank's balanced salt solution (HBSS; Sigma-Aldrich, 55037c), and 10 µL of the suspension was mixed to an equal volume (10 µL) of 0.4% Trypan blue stain. The mixture was gradually mixed and left to incubate for approximately 3 min, after which 10 µL of the mixture was loaded into the Invitrogen Countess® II FL disposable counting slide chambers and loaded into the Invitrogen Countess® II FL automated bench-top cell counter for analysis.

2.2.2 The 3-(4,5-dimethylthiazol-2-yl)-2,5-Diphenyl Tetrazolium Bromide (MTT) Assay

The MTT colorimetric assay (Roche, 11465007001) was used to confirm cell viability. In this assay, tetrazolium salts are cleaved to formazan by the succinate-tetrazolium reductase system belonging to the respiratory chain of the mitochondria, and is only functional in metabolically undamaged viable cells. Cells (5×10^4) were resuspended in 100 µL media/well of a 96-well tissue culture plate and incubated for 4 h at 37°C in 5% CO_2 for attachment, after which, 10 µL MTT reagent was added and incubated at 37 °C in 5% CO_2 for 4 h. Following this, a 100 µL of the solubilisation buffer was added, and the plate was incubated overnight at 37°C in 5% CO_2. The plate was then read using the VICTOR Nivo® Multimode Plate Reader (PerkinElmer) at 570 nm.

2.3 Apoptosis

2.3.1 The Caspase-Glo® 3/7 Assay

The Caspase-Glo® 3/7 assay (Promega, AnaTech, G8090) is centred on measuring standardised luminescent activity of the members of the cysteine aspartic acid-specific protease (caspase) family, caspase-3 and -7, that play an essential effector role in cell apoptosis. In this assay, addition of the Caspase-Glo 3/7® reagent causes cell lysis, with subsequent caspase cleavage of a tetra peptide sequence DEVD substrate, and the production of luminescence. Approximately 2×10^4 cells were suspended in a total volume of 100 µL media/well of a white-walled 96-well plate and incubated for 4 h at 37 °C in 5% CO_2 for attachment. After incubation, 100 µL of Caspase-Glo® 3/7 reagent was added, and using an orbital shaker, the contents were gently mixed at 300–500 rpm for 30 s and incubated at room temperature for 1 h. The luminescence of each sample was read in the VICTOR Nivo® Multimode Plate Reader (PerkinElmer). The emitted luminescence is proportional to the extent of caspase-3 and -7 activity in the cells.

2.3.2 The Enzyme-Linked Immunosorbent Assay (ELISA)

The sandwich ELISA was used to quantitatively evaluate the concentration of the released Bcl-2 (Human Bcl-2 ELISA Kit, Abcam, ab202411) in culture media according to the manufactures' guidelines. Culture media was collected 48 h post-irradiation, frozen, and stored for further analysis. All three repeats were run together on the same plate. Briefly, 100 µL of standard or sample was dispensed in duplicate to a 96-well plate coated with immobilised human Bcl-2 capture antibody. Wells were washed 4× with wash buffer (Bio-Rad, PW40 microplate washer), followed by the addition of 100 µL of biotinylated anti-human Bcl-2 antibody. Unbound biotinylated antibody was washed and 100 µL of HRP-conjugated streptavidin added. After another washing step, 100 µL of 3,3′,5,5′-Tetramethylbenzidine (TMB) substrate solution was added, and incubated at room temperature in the dark on a shaker (moderate shaking) for 30 min. The reaction was stopped through the addition of 50 µL stop solution, and absorbance measured at 450 nm by means of the VICTOR Nivo® Multimode Plate Reader (PerkinElmer). The developed colour was relative to the concentration of the bound Bcl-2.

2.3.3 The Annexin V/PI–Fluorescein Isothiocyanate (FITC) and Propidium Iodide (PI) Assay

The Annexin V/PI–fluorescein isothiocyanate (FITC) and propidium iodide (PI) (BD Biosciences, 556547, The Scientific Group, South Africa) flow cytometry assay is mostly used to categorise membrane phosphatidyl serine in apoptotic cells and destruction of the membrane in necrotic cells. The assay was performed on the BD Accuri™ C6 flow cytometer matching the manufacturers'

instructions. In brief, following treatment and incubation, cells from all models were detached using TrypLE™ Select and washed 3× in HBSS. Cells were resuspended in 1× binding buffer at a concentration of 10^6 cells/mL. A 100 µL of the cell suspension was stained with 5 µL each of the Annexin V–FITC and PI reagents for 10 min in the dark at room temperature. Flow cytometric analysis at a rate of 400 events per second with a limit of 350 µL was performed within 1 h. Annexin V–FITC was detected as green fluorescence, and PI as red.

2.4 Statistical Analysis

SigmaPlot version 14 (Systat Software, Inc.) was used for statistical analysis, and the statistical difference between groups was distinguished by using the Student's *t*-test. The one way analysis of variance (ANOVA) followed by Dunnett's test was used to compare the differences between the cell models. A statistically significant difference between two groups determined using a *p*-value does not show the true magnitude of the difference which can only be determined using an effect size. To quantify the effect size between unirradiated and irradiated groups, Cohen's *d* was employed. Results are shown as standard error of the mean (SEM) and statistical significance is shown in the graphs as $^{*}p < 0.05$, $^{**}p < 0.01$ and $^{***}p < 0.001$.

3 Results

3.1 Cell Morphology and Migration Rate

There was no cellular morphological difference in both irradiated and non-irradiated normal and diabetic wounded cell models 48 h following irradiation. The cells appeared aligned, mostly in parallel, slender, and stretching outwards, with protrusions, proliferating and spreading to form a single stratum of cells (Fig. 1).

This study assessed the distance between the borders of the "wound" (Fig. 2) which were used to calculate the percentage migration rate. A significant percentage migration rate was observed in irradiated W and DW cells with large effect sizes (Cohen's *d* of 3.027 and 2.375, respectively) as compared to their unirradiated controls (Table 2). When compared to unirradiated (0 J/cm^2) W cells, a significant decline in the percentage migration rate was noted in unirradiated (0 J/cm^2) DW cell models ($p < 0.01$).However, irradiated (5 J/cm^2) DW cells displayed no difference in the percentage migration rate as compared to irradiated (0 J/cm^2) W cells ($p = 0.842$), and as shown in Fig. 2, there was partial and complete wound closure observed in irradiated (5 J/cm^2) W and DW cell models, respectively, 48 h after irradiation.

3.2 Cell Viability

Cellular viability represents the percentage of viable/live cells of the culture. The Trypan blue exclusion and MTT assays were used to assess for cell viability in all models. Using the Trypan blue exclusion assay (Fig. 3), a significant increase in cellular viability was observed in irradiated (5 J/cm^2) W and DW cells with large effect sizes (Cohen's *d* of 3.377 and 4.859, respectively). Using one-way ANOVA, there was a significant decline in percentage cell viability in unirradiated (0 J/cm^2) W cells ($p < 0.05$) and DW cells ($p < 0.001$) when compared to unirradiated (0 J/cm^2) N cells. When cells were irradiated, this difference was no longer evident in irradiated (5 J/cm^2) W cells as compared to unirradiated (0 J/cm^2) N cells.

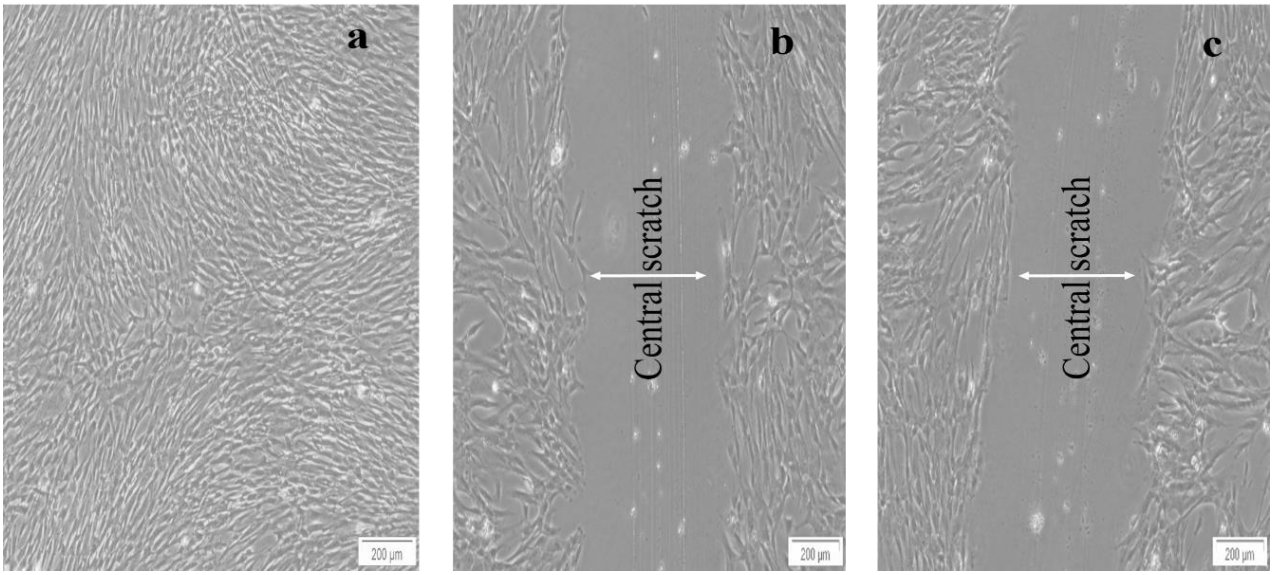


Fig. 1 Representative micrographs showing cellular morphology observed in (a) normal (N), (b) wounded (W), and (c) diabetic wounded (DW) WS1 human skin fibroblast cells. Wounded cell models were created using the central scratch assay performed on a confluent monolayer, and is highlighted by a white line. Magnification ×200.

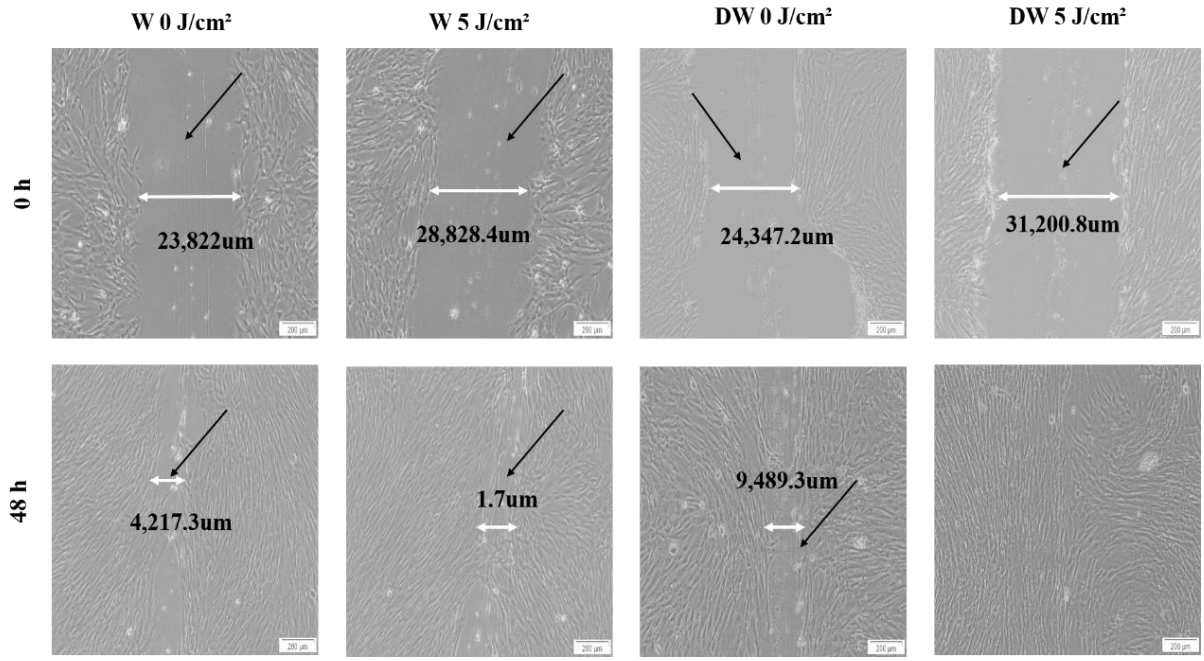


Fig. 2 Cell migration observed at 0 h and 48 h (n = 3) in both irradiated (5 J/cm^2) and unirradiated (0 J/cm^2) wounded (W) and diabetic wounded (DW) cells. In the micrographs, the "wound" and the remaining gaps of the wound are shown by a white line or black arrows. Magnification ×200.

Table 2 The percentage migration rate in wounded (W) and diabetic wounded (DW) cells was calculated using the formula $(At_{0h} - At_{time})/At_{0h} \times 100$. An elevated percentage at which the "wound" closed was noted in irradiated (5 J/cm^2) W and DW cells at 48 h (n = 3). The p-value (SEM) shows the significant probability as compared to respective unirradiated (0 J/cm^2) controls (SEM).

Model	Unirradiated (0 J/cm^2)	Irradiated (5 J/cm^2)	p-value
W	82.3 ± 1%	99.9 ± 0.1%	$p < 0.05$
DW	61.0 ± 0.6%	100.0 ± 0.0%	$p < 0.01$

However, a significant decrease was still evident in irradiated (5 J/cm^2) DW cells ($p < 0.05$) when compared to unirradiated (0 J/cm^2) N cells. A significant decrease in cell viability was noted when unirradiated (0 J/cm^2) DW cell models were compared to unirradiated W cells ($p < 0.01$), as is expected. This decrease was still evident after irradiation ($p < 0.05$).

The MTT assay revealed a significant reduction in viability, with a large effect size (Cohen's d of 6.496) in irradiated (5 J/cm^2) N cells, and a significant increase in irradiated (5 J/cm^2) W and DW cells with large effect sizes (Cohen's d of 7.167194 and 4.147085, respectively) (Fig. 3). Using one-way ANOVA, a significant decline in cell viability was observed in unirradiated (0 J/cm^2) W and DW cells when compared to unirradiated (0 J/cm^2) N cells ($p < 0.001$). There was no significant difference observed in cell viability when unirradiated (0 J/cm^2) DW cell models were compared to unirradiated W cells. However, a significant increase in cell viability was noted in irradiated (5 J/cm^2) DW cells ($p < 0.01$) when compared to irradiated (5 J/cm^2) W cells.

3.3 Apoptosis

Apoptosis normally occurs during embryonic development and is important for maintaining tissue homeostasis. Unwanted compromised cells activate an intracellular death program characterised by the cells morphologic changes including loss of plasma membrane symmetry, condensed cytoplasm and nucleus, and cleavage of deoxyribonucleic acid (DNA). In wound healing apoptosis is critical for the removal of the inflammatory response cells, and later for scar construction [23]. Abnormal and uncontrolled cellular apoptosis may hinder the wound healing process leading to the development of wound chronicity. Here, cellular apoptosis was assessed using the Caspase-Glo® 3/7 assay, and ELISA for the cellular release/excretion of Bcl-2, a cellular protein that controls apoptosis.

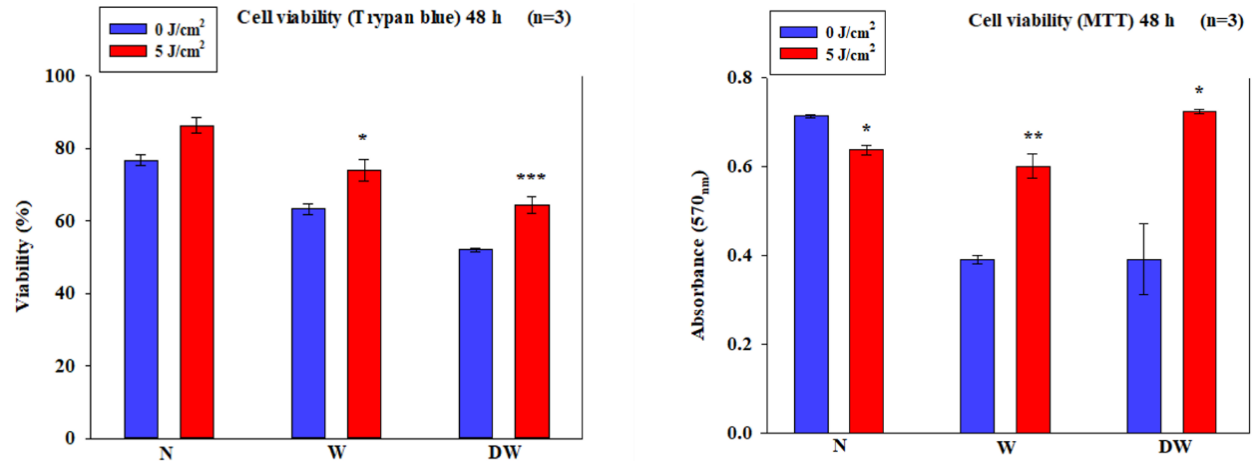


Fig. 3 Cellular viability as measured by the Trypan blue exclusion and MTT assays in unirradiated (0 J/cm^2) and irradiated (5 J/cm^2) normal (N), wounded (W) and diabetic wounded (DW) cell models 48 h after irradiation. Significant probability is indicated as $^{*}p < 0.05$, $^{**}p < 0.01$ and $^{***}p < 0.001$ (± SEM).

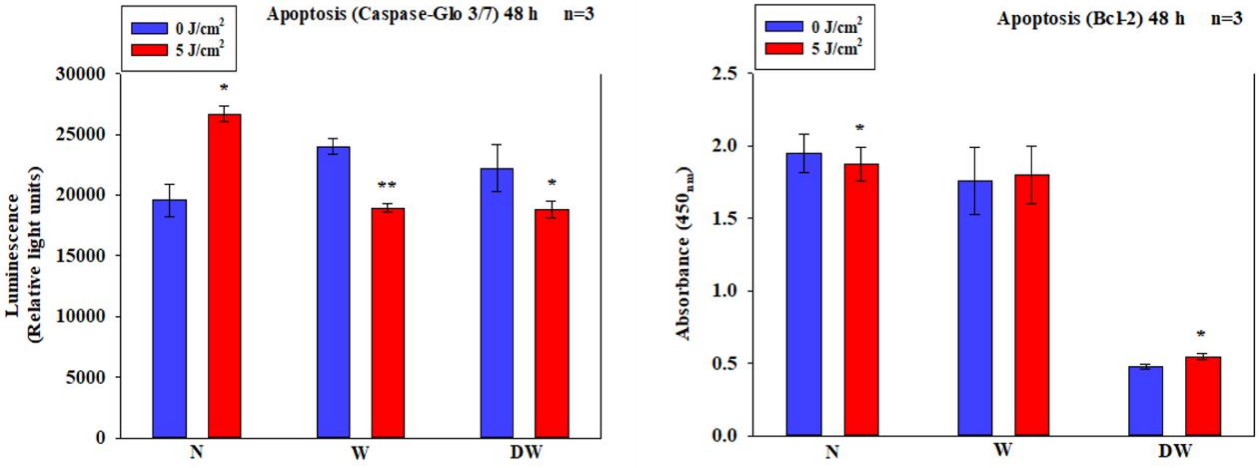


Fig. 4 Cellular apoptosis as measured by the Caspase-Glo® 3/7 assay that measures caspase-3 and -7 activity, and the release/excretion of Bcl-2 (ELISA) in normal (N), wounded (W), and diabetic wounded (DW) cells at 48 h after irradiation at 660 nm with 5 J/cm^2. Significant probability related to control cells is shown as $^{*}p \leq 0.05$ and $^{**}p \leq 0.01$ (± SEM).

This study further tracked cellular apoptosis using Annexin V/PI assay, a method that is widely used to determine stages of apoptotic cell death. The assay assesses cells that are viable/live, those that are undergoing early apoptosis, and finally those that are undergoing late stage of apoptosis or are dead (necrotic) [24].

3.3.1 Caspase-3 and -7 Activity

Using the Caspase-Glo® 3/7 assay, a significant increase in caspase-3 and -7 activity was observed in irradiated N cells with a large effect size (Cohen's *d* of 4.755). However, irradiated W and DW cells displayed a significant decrease with large effect sizes (Cohen's *d* of 6.743 and 1.641, respectively) (Fig. 4). When W and DW cell models were compared to unirradiated (0 J/cm^2) N cells using one-way ANOVA, a significant increase in cell caspase-3 and -7 activity was seen in unirradiated (0 J/cm^2) W and DW cells ($p < 0.05$). This difference compared to unirradiated (0 J/cm^2) N cells was no longer evident when W and DW cells were irradiated. There was no difference between unirradiated (0 J/cm^2) and irradiated (5 J/cm^2) W and DW cells, respectively.

3.3.2 Release of Bcl-2

Determining for the release of Bcl-2 into cell culture media using ELISA revealed a significant reduction in Bcl-2 in irradiated (5 J/cm^2) N cells with a medium effect size (Cohen's *d* of 0.587), and a significant increase in irradiated (5 J/cm^2) DW cells with a large effect size (Cohen's *d* of 3.462) (Fig. 4). A significant reduction in the release of Bcl-2 was revealed in both unirradiated (0 J/cm^2) and irradiated (5 J/cm^2) DW cells ($p < 0.001$) compared to unirradiated (0 J/cm^2) N cells. This difference was not observed in unirradiated (0 J/cm^2) and irradiated W cells compared to unirradiated (0 J/cm^2) N cells. When compared to unirradiated (0 J/cm^2) and irradiated (5 J/cm^2) W cells, a significant decrease was observed in unirradiated (0 J/cm^2) and irradiated (5 J/cm^2) DW cells ($p < 0.001$), respectively.

Table 3 Variations in live cells, early apoptosis, late apoptosis, and necrotic cells at 48 h ($n = 3$) using Annexin V/PI–fluorescein isothiocyanate (FITC) and propidium iodide (PI) flow cytometry assay in normal (N) wounded (W) and diabetic wounded (DW). Significant probability is shown as $^{*}p \leq 0.05$, $^{**}p \leq 0.01$ and $^{***}p \leq 0.001$ (SEM).

Model	Live cells		Early apoptosis		Late apoptosis		Necrotic cells	
	0 J/cm^2	5 J/cm^2	0 J/cm^2	5 J/cm^2	0 J/cm^2	5 J/cm^2	0 J/cm^2	5 J/cm^2
N	80.0 ± 2.0	82.0 ± 2.0	4.0 ± 0.7	3.0 ± 0.8	13.0 ± 5.0	14.0 ± 1.0	3.0 ± 1.0	1.0 ± 1.0
W	85.0 ± 3.0	85.0 ± 2.0	5.0 ± 0.7	2.0 ± 1.2*	9.0 ± 1.2	17.0 ± 1.2**	2.0 ± 0.5	1.0 ± 0.2
DW	72.0 ± 2.0	83.0 ± 2.0***	9.0 ± 2.0	3.0 ± 1.0**	9.0 ± 0.6	6.0 ± 1.0***	10.0 ± 1.0	6.0 ± 1.0*

The Annexin V/PI assay (Table 3) revealed a significant decrease in the population of early apoptotic cells with a large effect size (Cohen's *d* of 1.897), and a significant increase in late apoptotic cells with a large effect size (Cohen's *d* of 3.578) in irradiated W cells when compared to their unirradiated control cells. Irradiated DW cells showed a significant increase in live (viable cells) with a large effect size (Cohen's *d* of 3.667), and a significant decrease in late apoptotic and necrotic cells with a large effect size (Cohen's *d* of 3.667 and 2.530, respectively) when compared to their control cells. When compared to the unirradiated (0 J/cm^2) N cell model using one-way ANOVA, a significant increase in cells going through early apoptosis and necrosis was noted in unirradiated (0 J/cm^2) DW cells ($p < 0.01$), along with a significant decrease in live cells ($p < 0.01$). There was a significantly increased number of necrotic cells noted in irradiated (5 J/cm^2) DW cells ($p < 0.05$) when compared to unstressed, unirradiated (0 J/cm^2) N cells. When compared to both unirradiated (0 J/cm^2) W cells, unirradiated (0 J/cm^2) DW cells showed a significant decrease in live cells ($p < 0.001$). No difference was observed in irradiated (5 J/cm^2) DW cells. A significant decrease in late apoptosis was noted in unirradiated (5 J/cm^2) DW cells when compared to irradiated (5 J/cm^2) W cells ($p < 0.01$). A significant decrease in late apoptosis was noted in irradiated (5 J/cm^2) DW cells ($p < 0.001$) when compared to irradiated (5 J/cm^2) W cells. No difference was observed in unirradiated (5 J/cm^2) DW cells ($p < 0.001$) when compared to unirradiated (5 J/cm^2) W cells. There was a significant increase in necrotic cells in both unirradiated (0 J/cm^2) and irradiated (5 J/cm^2) DW cells when compared to both unirradiated (0 J/cm^2) and irradiated (5 J/cm^2) W cells ($p < 0.001$), respectively.

4 Discussion

All complications related to DM, including chronic wounds, increase economic burden to the affected persons as well as society [25, 26]. In DM, the normal wound healing process is disrupted, causing tissue damage, and abnormal apoptotic ability [27]. Hyperglycaemia and the systemic build-up of AGEs affect fibroblast cell migration, proliferation, viability, secretion of growth factors, and construction of granulation tissue. Fibroblasts from diabetic patients suffer mitochondrial impairments and become susceptible to apoptosis [28, 29]. PBM has shown to have therapeutic effects on diabetic wounds, and when used as an adjunctive therapy along with standard treatment methods, it improves diabetic wound healing [30, 31]. For instance, when Layegh et al. [32], used PBM at a wavelength of 660 nm and a fluence of 3 J/cm^2, they noted a significant decrease in the diabetic wound area and an increase in the formation of granulation tissue. Nevertheless, the mechanism of PBM in diabetic wound healing is not completely clarified. This study used PBM at 660 nm and a fluence of 5 J/cm^2 to understand its molecular and cellular effect on diabetic wounded fibroblast cells 48 h after irradiation.

Under a light microscope, fibroblast cells appear spindle shaped or radiating star like patterned cells with a centrally round or oval nucleus [33]. According to Loots et al. [34], fibroblast cells from diabetic foot ulcers appear to be large and broadly spread under light microscopy. Chellini et al. [35], observed that near infrared (NIR) and violet-blue light irradiated fibroblast cells presented with a polygonal outline and a higher surface area when compared to red light irradiated fibroblast cells which seemed extended or stretched and spindle-shaped. The present study noticed no cellular morphological difference in both irradiated and non-irradiated normal and diabetic cell models following irradiation. Gradually, cells began spreading out and changed their direction of growth, and started moving into the central scratch in an attempt to 'close the wound'.

Fibroblast cells are a key in the production of ECM, and remodelling and tightening of the healing wound [36]. Mostly, wound healing is delayed or may not get restored at all when the granulation tissue construction process is dysfunctional [37]. Fibroblast cell migration towards the wound milieu is critical during the proliferative stage of wound healing. In DM, cellular migration has been shown to be delayed [38]. The present study demonstrates that PBM at 660 nm and a fluence of 5 J/cm^2 accelerates the wound repairing processes via the stimulation of fibroblast migration and viability. The study observed a significant increase with a large effect size in cellular viability, migration towards the centre of the "wound", and wound closure in irradiated wounded and diabetic wounded cell models. Xuan et al. [39], suggested that the hyperglycaemic mediated suspension of cell migration is related to the inhibition of basic fibroblast growth factor (bFGF) signalling, specifically because of c-Jun N-terminal kinases (JNKs) suppression.

In another study, Lerman et al. [40], observed that diabetic fibroblasts show impairments in cellular migration, growth factor production, and their reaction to hypoxia *in vitro*. This study demonstrated decreased cell migration and viability in unirradiated DW cells when compared to unirradiated W cells, indicating the effect of high glucose concentration in the culture media. However, after irradiation this effect was no longer evident, suggesting the positive effect of PBM on diabetic cells and the effect of high glucose concentration in the culture media.

Besides reducing cell migration, viability, proliferation, and synthesis of collagen, *in vitro* experiments have shown that hyperglycaemia increases apoptosis in different cell types [41]. In typical wound healing, apoptosis is necessary for eradicating inflammatory cells and scar construction without inflammation and tissue damage [30], and involves different cellular morphological features and signalling pathways with the instigation of caspases, and subsequent reduction in viability [42]. PBM at a wavelength ranging between 600 and 1200 nm has been reported to reduce apoptosis in different tissues, and when Davies et al. [43], investigated the influence of 660 nm PBM on cell apoptosis, they observed a significantly high fraction of apoptotic cells in the control group as compared to irradiated group. In addition, Rajendran et al. [44], noted that PBM at a wavelength of 660 nm reversed high oxidative stress in diabetic and diabetic wounded fibroblast cells as represented by decreased FOXO1 levels, and suggested that PBM advanced diabetic wound healing by reducing oxidative stress via the inhibition of FOXO1 signalling. Tam et al. [45], suggested that PBM at a lower energy reduces apoptosis but promotes it at a higher energy. Nonetheless, the existing understanding regarding the effect of PBM on cellular apoptosis and diabetic wound healing is elusive. To determine the protective impact of PBM at 660 nm and 5 J/cm^2 against apoptosis in diabetic wound healing, this study used Caspase-Glo® 3/7 assay, ELISA and Annexin V/PI assay to compare cellular caspase activity, secretion of Bcl-2, the percentage of live cells, and those that were undergoing early and late apoptosis, as well as necrotic cells in both unirradiated and irradiated cell models. This study noted a significant decrease with a large effect size in the activity of pro-apoptotic caspase-3 and -7, and a significant increase with a large effect size in anti-apoptotic Bcl-2 protein in DW cells exposed to PBM at 660 nm. This study noted an increase in the percentage of cells undergoing early apoptosis in unirradiated DW cells as compared to unirradiated W cells, signifying the effect of high sugar concentration in the culture media. As compared to unirradiated N cells, there was a considerable rise in early apoptosis and necrotic cells, as well as a decrease in viable cells and late apoptosis in unirradiated W and DW cells. However, when these cells were irradiated, they responded positively with a large effect size, as compared to their unirradiated control cells, suggesting a positive therapeutic effect of PBM. In another study, Cheng et al. [46], suggested that PBM improves cell proliferation and reduces tumour necrosis factor alpha (TNF-α)/cycloheximide-facilitated cell death. Maldaner et al. [47], also suggested that PBM augmented the proliferative and protective effect of hydrogen peroxide (H_2O_2) induced senescence in fibroblast cells. These observations indicate that the therapeutic effects observed were due to PBM, and this study has further demonstrated that PBM used at a wavelength of 660 nm and a fluence of 5 J/cm^2 influence cell viability, migration, and wound healing specifically through modulation of the cellular pro- and anti-apoptotic proteins in diabetic wounded cells *in vitro*.

5 Conclusion

This study has demonstrated that reduced wound healing in diabetic wounded cells *in vitro* is caused by reduced cell viability and migration, and increased cell apoptosis. However, PBM effectively regulated these defects, and restored the normal functioning of DW cells *in vitro*, indicating that PBM in the visible red range speed up diabetic wound healing. Although the present study demonstrated these molecular effects of PBM in hastening wound healing, there is a need for further studies to gain more understanding on its effect at a molecular, cellular and tissue level. This study has exhibited that PBM could indeed influence the rebuilding and restoration of diabetic wounds, and within this context, it could be used as an adjunct treatment method to stimulate wound healing processes *in vivo*.

Acknowledgements

Lasers used in this study were provided and maintained by the Council for Scientific and Industrial Research (CSIR)-National Laser Centre (NLC). This work was funded by the South African Research Chairs Initiative of the Department of Science and Technology (DST) and National Research Foundation of South Africa (NRF, Grant No 98337), as well as grants received from the University of Johannesburg (URC), the National Research Foundation (NRF, Grant No 129327).

Disclosures

The authors declare no conflict of interest.

References

1. S. Ellis, E. J. Lin, and D. Tartar, "Immunology of wound healing," Current Dermatology Reports 7, 350–358 (2018).

2. F. Cialdai, C. Risaliti, and M. Monici, "Role of fibroblasts in wound healing and tissue remodeling on Earth and in space," Frontiers in Bioengineering and Biotechnology 10, 958381 (2022).
3. M. Kandhwal, T. Behl, S. Singh, N. Sharma, S. Arora, S. Bhatia, A. Al-Harrasi, M. Sachdeva, and S. Bungau, "Role of matrix metalloproteinase in wound healing," American Journal of Translational Research 14(7), 4391–4405 (2022).
4. A. E. Dodi, I. O. Ajayi, C. Chang, M. Beard, S. L. Ashley, S. K. Huang, V. J. Thannickal, D. J. Tschumperlin, T. H. Sisson, and J. C. Horowitz, "Regulation of fibroblast fas expression by soluble and mechanical pro-fibrotic stimuli," Respiratory Research 19(1), 91 (2018).
5. J. Dai, H. Chen, and Y. Chai, "Advanced glycation end products (ages) induce apoptosis of fibroblasts by activation of nlrp3 inflammasome via reactive oxygen species (ros) signaling pathway," Medical Science Monitor: International Medical Journal of Experimental and Clinical Research 25, 7499–7508 (2019).
6. M. Brentnall, L. Rodriguez–Menocal, R. L. De Guevara, E. Cepero, and L. H. Boise, "Caspase–9, caspase–3 and caspase–7 have distinct roles during intrinsic apoptosis," BMC Cell Biology 14, 32 (2013).
7. A. G. Porter, R. U. Jänicke, "Emerging roles of caspase–3 in apoptosis," Cell Death & Differentiation 6, 99–104 (1999).
8. E. Eskandari, C. J. Eaves, "Paradoxical roles of caspase–3 in regulating cell survival, proliferation, and tumorigenesis," Journal of Cell Biology 221(6), e202201159 (2022).
9. S. Qian, Z. Wei, W. Yang, J. Huang, Y. Yang, and J. Wang, "The role of Bcl–2 family proteins in regulating apoptosis and cancer therapy," Frontiers in Oncology 12, 985363 (2022).
10. T. Desta, J. Li, T. Chino, and D. T. Graves, "Altered fibroblast proliferation and apoptosis in diabetic gingival wounds," Journal of Dental Research 89, 609–614 (2010).
11. P. Bainbridge, "Wound healing and the role of fibroblasts" Journal of Wound Care 22(8), 407–408 (2013).
12. "IDF Diabetes Atlas", 10th ed., 2021 (accessed 12 June 2023). [https://diabetesatlas.org/data/en/].
13. X. Liao, S. H. Li, M. M. El Akkawi, X. Fu, H. Liu, and Y. Huang, "Surgical amputation for patients with diabetic foot ulcers: A Chinese expert panel consensus treatment guide," Frontiers in Surgery 9, 1003339 (2022).
14. S. Rashidi, A. Yadollahpour, and M. Mirzaiyan, "low level laser therapy for the treatment of chronic wound: clinical considerations," Biomedical and Pharmacology Journal 8(2), 1121–1127 (2015).
15. C. Dompe, L. Moncrieff, J. Matys, K. Grzech-Leśniak, I. Kocherova, A. Bryja, M. Bruska, M. Dominiak, P. Mozdziak, T. H. I. Skiba, J. A. Shibli, A. A. Volponi, B. Kempisty and M. Dyszkiewicz-Konwińska, "Photobiomodulation–underlying mechanism and clinical applications," Journal of Clinical Medicine 9(6), 1724 (2020).
16. S. Farivar, T. Malekshahabi, and R. Shiari, "Biological effects of low level laser therapy," Journal of Lasers in Medical Sciences 5(2), 58–62 (2014).
17. N. Houreld, "Healing effects of photobiomodulation on diabetic wounds," Applied Sciences 9(23), 5114 (2019).
18. N. Houreld, H. Abrahamse, "Low-intensity laser irradiation stimulates wound healing in diabetic wounded fibroblast cells (ws1)," Diabetes Technology & Therapeutics 12(12), 971–978 (2010).
19. N. N. Houreld, P. R. Sekhejane, and H. Abrahamse, "Irradiation at 830 nm stimulates nitric oxide production and inhibits pro–inflammatory cytokines in diabetic wounded fibroblast cells: Diabetic wounded fibroblast cells," Lasers in Surgery and Medicine 42(6), 494–502 (2010).
20. F. Felice, Y. Zambito, E. Belardinelli, A. Fabiano, T. Santoni, and R. Di Stefano, "Effect of different chitosan derivatives on in vitro scratch wound assay: A comparative study," International Journal of Biological Macromolecules 76, 236–241 (2015).
21. M. Fronza, G. F. Caetano, M. N. Leite, C. S. Bitencourt, F. W. G. Paula–Silva, T. A. M. Andrade, M. A. Frade, I. Merfort, and L. H. Faccioli, "Hyaluronidase modulates inflammatory response and accelerates the cutaneous wound healing," PLoS ONE 9(11), e112297 (2014).
22. S. W. Jere, N. N. Houreld, and H. Abrahamse, "Photobiomodulation at 660 nm stimulates proliferation and migration of diabetic wounded cells via the expression of epidermal growth factor and the JAK/STAT pathway," Journal of Photochemistry and Photobiology B: Biology 179, 74–83 (2018).
23. M. Ghasemi, T. Turnbull, S. Sebastian, and I. Kempson, "The MTT assay: utility, limitations, pitfalls, and interpretation in bulk and single-cell analysis," International Journal of Molecular Sciences 22(23), 12827 (2021).
24. S. Riwaldt, T. J. Corydon, D. Pantalone, J. Sahana, P. Wise, M. Wehland, M. Krüger, D. Melnik, S. Kopp, M. Infanger, and D. Grimm,"Role of apoptosis in wound healing and apoptosis alterations in microgravity," Frontiers in Bioengineering and Biotechnology 9, 679650 (2021).
25. R. Kumar, A. Saneja, and A. K. Panda, "An annexin V-FITC-propidium iodide–based method for detecting apoptosis in a non–small cell lung cancer cell line," Lung Cancer: Methods and Protocols 2279, 213–223 (2021).
26. S. S. K. Reddy, M. Tan, "Diabetes mellitus and its many complications," Chapter 1 in Diabetes Mellitus, M. Tan (Ed.), Academic Press, 1–18 (2020).
27. P. Farmaki, C. Damaskos, N. Garmpis, A. Garmpi, S. Savvanis, and E. Diamantis, "Complications of the type 2 diabetes mellitus," Current Cardiology Reviews 16(4), 249–251 (2020).

28. J. Y. Ji, D. Y. Ren, and Y. Z. Weng, "Efficiency of multifunctional antibacterial hydrogels for chronic wound healing in diabetes: a comprehensive review," International Journal Nanomedicine 17, 3163–3176 (2022).
29. J. Berlanga-Acosta, G. S. Schultz, E. López-Mola, G. Guillen-Nieto, M. García-Siverio, and L. Herrera-Martínez, "Glucose toxic effects on granulation tissue productive cells: the diabetics' impaired healing," BioMed Research International 2013, 256043 (2013).
30. Y. Liu, Y. Liu, W. He, X. Mu, X. Wu, J. Deng, and X. Nie "Fibroblasts: immunomodulatory factors in refractory diabetic wound healing," Frontiers in Immunology 13, 918223 (2022).
31. Z. X. Wang, S. H. Kim, "Effect of photobiomodulation therapy (660 nm) on wound healing of rat skin infected by staphylococcus," Photobiomodulation, Photomedicine, and Laser Surgery 38(7), 419–424 (2020).
32. S. B. Pavlov, N. M. Babenko, M. V. Kumetchko, I. B. Litvinova, and R. N. Mikhaylusov, "Experimental study of the effect of photobiomodulation therapy on the regulation of the healing process of chronic wounds," International Journal of Photoenergy 2021, 3947895 (2021).
33. E. R. Layegh, F. F. Fadaei, M. Lotfinia, F. Zare, A. M. Tofigh, S. Abrishami, and A. Piryaei, "Photobiomodulation therapy improves the growth factor and cytokine secretory profile in human type 2 diabetic fibroblasts," Journal of Photochemistry and Photobiology B: Biology 210, 111962 (2020).
34. M. Ravikanth, P. Soujanya, K. Manjunath, T. R. Saraswathi, and C. R. Ramachandran, "Heterogenecity of fibroblasts," Journal of Oral and Maxillofacial Pathology 15(2), 247–250 (2011).
35. M. A. Loots, E. N. Lamme, J. R. Mekkes, J. D. Bos, and E. Middelkoop, "Cultured fibroblasts from chronic diabetic wounds on the lower extremity (non-insulin-dependent diabetes mellitus) show disturbed proliferation," Archives of Dermatological Research 291, 93–99 (1999).
36. F. Chellini, A. Tani, S. Zecchi-Orlandini, M. Giannelli, and C. Sassoli, "In vitro evidences of different fibroblast morpho-functional responses to red, near-infrared and violet-blue photobiomodulation: clues for addressing wound healing," Applied Sciences 10(21), 7878 (2020).
37. H. Xing, Y. Huang, B. H. Kunkemoeller, P. J. Dahl, O. Muraleetharan, N. S. Malvankar, M. P. Murrell, and T. R. Kyriakides, "Dysregulation of TSP2–Rac1–WAVE2 axis in diabetic cells leads to cytoskeletal disorganization, increased cell stiffness, and dysfunction," Scientific Reports 3(1), 4253 (2022).
38. R. Addis, S. Cruciani, S. Santaniello, E. Bellu, G. Sarais, C. Ventura, M Maioli, and G Pintore, "Fibroblast proliferation and migration in wound healing by phytochemicals: evidence for a novel synergic outcome," International Journal of Medical Sciences 17(8), 1030–1042 (2020).
39. Y. H. Xuan, B. B. Huang, H. S. Tian, L. S. Chi, Y. M. Duan, X. Wang, Z. X. Zhu, W. H. Cai, Y. T. Zhu, T. M. Wei, H. B. Ye, W. T. Cong, and L. T. Jin, "High-glucose inhibits human fibroblast cell migration in wound healing via repression of bFGF-regulating JNK phosphorylation," PLoS One 9(9), e108182 (2014).
40. O. Z. Lerman, R. D. Galiano, and M. Armour, J. P. Levine, and G. C. Gurtner, "Cellular dysfunction in the diabetic fibroblast: impairment in migration, vascular endothelial growth factor production, and response to hypoxia," The American Journal of Pathology 162(1), 303–312 (2003).
41. P. Buranasin, K. Mizutani, K. Iwasaki, C. P. N. Mahasarakham, D. Kido, K. Takeda, and Y. Izumi, "High glucose-induced oxidative stress impairs proliferation and migration of human gingival fibroblasts," PLoS One 13(8), e0201855 (2018).
42. S. Elmore, "Apoptosis: a review of programmed cell death," Toxicologic Pathology 35(4), 495–516 (2007).
43. D. J. Davies, M. Hadis, V. Di Pietro, G. Lazzarino, M. Forcione, G. Harris, A. R. Stevens, W. C. Soon, P. Goldberg Oppenheimer, M. Milward, A. Belli, and W. M. Palin, "Photobiomodulation reduces hippocampal apoptotic cell death and produces a Raman spectroscopic signature," PLoS One 17(3), e0264533 (2022).
44. N. K. Rajendran, N. N. Houreld, and H. Abrahamse, "Photobiomodulation reduces oxidative stress in diabetic wounded fibroblast cells by inhibiting the FOXO1 signaling pathway," Journal of Cell Communication and Signaling 15(2), 195–206 (2021).
45. S. Y. Tam, V. C. W. Tam, S. Ramkumar, M. L. Khaw, H. K. W. Law, and S. W. Y. Lee, "Review on the cellular mechanisms of low-level laser therapy use in oncology," Frontiers in Oncology 10, 1255 (2020).
46. Y. J. Cheng, H. C. Ou, and C. H. Lee, "Low level laser therapy prevent endothelial cells from TNF–alpha/cycloheximide–induced apoptosis by modulating P38 MAPK/NF-kB pathway," Physiotherapy 101(1), 401–403 (2015).
47. D. Maldaner, V. Azzolin, F. Barbisan, M. Mastela, C. Teixeira, A. Dihel, T. Duarte, N. Pellenz, L. Lemos, C. Negretto, I. Da cruz, and M. Duarte, "In vitro effect of low-level laser therapy on the proliferative, apoptosis modulation, and oxi-inflammatory markers of premature-senescent hydrogen peroxide-induced dermal fibroblasts," Lasers in Medical Science 34(11), 1333–1343 (2019).

Multidimensional Analysis of Dermoscopic Images and Spectral Information for the Diagnosis of Skin Tumors

Irina A. Matveeva[1], Andrey I. Komlev[1], Oleg I. Kaganov[2,3], Alexander A. Moryatov[2,3], and Valery P. Zakharov[1]

[1] Department of Laser and Biotechnical Systems, Samara National Research University, 34 Moskovskoe shosse, Samara 443086, Russia

[2] Department of Oncology, Samara State Medical University, 50 Solnechnaya str., Samara 443099, Russia

[3] Department of Visual Localization Tumors, Samara Regional Clinical Oncology Dispensary, 50 Solnechnaya str., Samara 443031, Russia

*e-mail: m-irene-a@yandex.ru

Abstract. The paper is devoted to the identification of skin tumors and interpretation of their component composition based on multidimensional analysis of Raman scattering spectral data and dermoscopic images. The dataset contains 65 samples of malignant melanomas, 107 seborrheic keratoses, and 166 nevi. The multivariate curve resolution alternating least squares analysis was performed for the Raman spectra to extract spectral profiles of main skin components and their composition. The obtained biochemical profiles of skin neoplasms were analyzed by the gradient boosting method. Dermoscopic image analysis was performed using a convolutional neural network with modified Visual Geometry Group 16-layer model architecture. Joint analysis of component and spatial features was carried out using logistic regression of the predicted values of a model based on Raman spectra and a model based on image analysis. As a result, a binary model for the classification of malignant melanoma and pigmented benign neoplasms was constructed, showing an area under the receiver operating characteristic of 0.94 (0.90–0.98) with 95% confidence interval. Combining spatial and Raman spectra derived component features makes it possible to increase the efficiency of diagnosing skin cancer. © 2024 Journal of Biomedical Photonics & Engineering.

Keywords: Raman spectra; multivariate curve resolution; dermatoscopy; malignant melanoma; seborrheic keratosis; pigmented nevus; multivariate method; gradient boosting; convolutional neural network.

Paper #9079 received 12 Mar 2024; revised manuscript received 20 Mar 2024; accepted for publication 21 Mar 2024; published online 22 Mar 2024. doi: 10.18287/JBPE24.10.010307.

1 Introduction

Skin neoplasms are one of the most commonly diagnosed forms of cancer [1]. However, visual diagnosis of skin tumors significantly depends on the qualifications and professional experience of the physician, and its accuracy varies from 40 to 80% due to the presence of many different nosologies of skin tumors that have similar distinctive features [2]. The gold standard in oncology is histological examination, but it requires sampling and is not applicable for initial examination or mass monitoring. Therefore, the urgent task is to develop tools and information processing methods that allow the doctor to diagnose skin tumors in a timely and accurate manner.

In recent years, optical methods have been increasingly used to investigate biological tissues and fluids [3–6]. Raman spectroscopy (RS) methods have the greatest sensitivity to changes in the chemical composition of neoplasms compared to healthy skin due to the recording the intensities of vibrational-rotational vibrations of the functional groups of molecules of nucleic acids, proteins, lipids, and hydrocarbons [7–9]. It

has been shown that discriminant analysis of RS samples using projection to latent structures (PLS-DA) provides a statistically reliable result [10]. Principal component analysis was successfully used to obtain differences in spectral data [11, 12]. Optical diagnostics of skin cancer has been further developed through the use of classification algorithms based on neural networks, demonstrating high sensitivity and specificity in real time. It was shown that the use of convolutional neural networks (CNN) for analyzing RS spectra allows one to achieve an accuracy in determining the type of skin tumor comparable to the diagnostic accuracy of qualified dermatologists [13, 14]. However, in most studies this approach is presented in the form of a "black box", focusing exclusively on the classification problem, and the classification criteria very often remain unknown, which does not allow them to be physically interpreted.

Recently, the method of multidimensional curve resolution (MCR) has found effective application in biology and medicine to determine the concentration of mixture components from spectra [15−17]. The application of the MCR method has been studied for the analysis of the RS spectra of mixtures of proteinogenic amino acids [18], the effect of noise on RS spectra resolution [19], and the possibility of diagnosing skin diseases [20]. It was shown [20] that each RS spectrum may be represented with accuracy 95% by concentration profile of eight groups of spectral components: elastin and nature moisturizing factor (1386, 1518, 1174, and 1230 cm^{-1}), keratin, collagen and elastin (1248, 1450, 1656 cm^{-1}), water (1642 cm^{-1}), proteins, lipids and nuclear acid (1248, 1271, 1301, 1318 cm^{-1}), proteins, lipids, nature moisturizing factor and melanin (1144, 1275, 1750, 1355, 1386, 1559, 1694 cm^{-1}), proteins and water (1450, 1642 cm^{-1}) and the contribution of the optical system. The relative component composition of skin neoplasms reconstructed using MCR analysis of Raman spectra can be physically interpreted and contains sufficient information for the classification of neoplasms [20]. However, the area under the receiver operating characteristic (ROC AUC) values do not exceed 0.70 for the discriminant analysis by PLS-DA.

It is known that the increase of the efficiency of tumor recognition can be achieved by implementation of multimodal diagnostic methods [21] that combine several qualitatively different groups of features. Since RS uses spectral and component profiles as characteristic distinguishing features, it is most natural to supplement them with spatial properties that characterize the heterogeneity of tumor growth and can be obtained from the analysis of dermatoscopic images. Machine learning algorithms demonstrate good performance in analyzing dermatoscopic images when working with several hundred features [22, 23], but classification accuracy indicators decrease with an increase in the number of features. To overcome the described shortcomings, deep learning methods are used [24−26], which require a huge amount of data. It is difficult to generate such a volume of data, so it is interesting to use methods for increasing and retraining the classifier when adding new data.

Therefore, the aim of this research is to develop a method for identifying skin tumors and interpreting their component composition based on multidimensional analysis of RS data and dermoscopic images.

2 Materials and Methods

2.1 Experimental Data

All Raman spectra and dermoscopic images of skin lesions were obtained using the experimental system (see Fig. 1), which combines portable RS unit and multispectral digital dermatoscope.

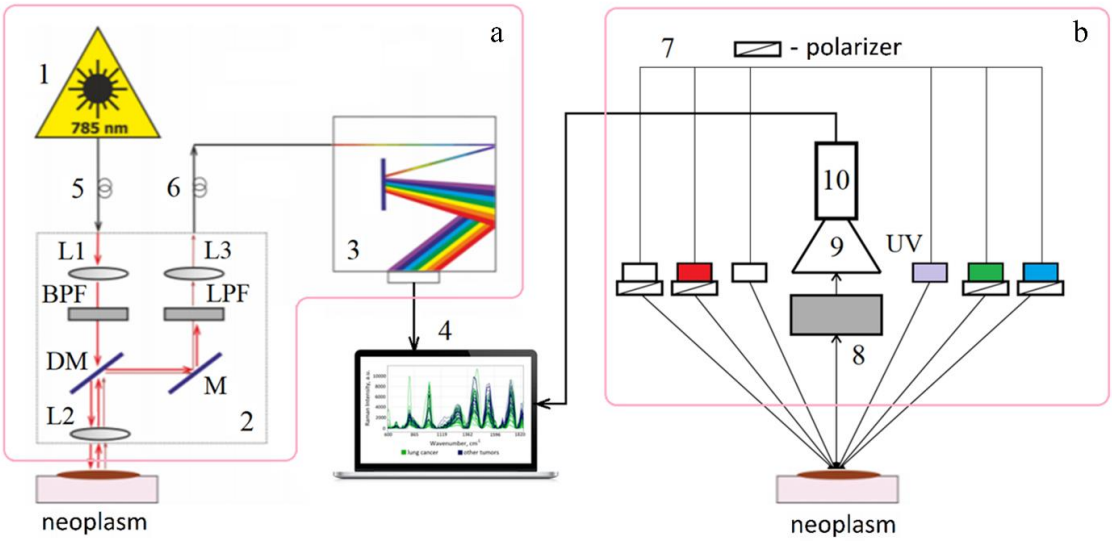


Fig. 1. Experimental system for recording Raman spectra of skin and dermoscopic images. (a) portable RS unit for *in vivo* studies of human skin (1 – laser module, 2 – Raman probe, 3 – spectrometer, 4 – personal computer, 5 – excitation fiber, 6 – collecting fiber, L1, L2, L3 – lenses, BPF – bandpass filter, DM – dichroic mirror, M – mirror, LPF – longpass filter) [27]. (b) Multispectral digital dermatoscope (7 – backlight, 8 – lens, 9 – camera, 10 – microcontroller, UV – ultraviolet LED).



Fig. 2 Convolutional neural network architecture.

The RS unit allows recording of Raman spectra in the near-infrared region when excited by 785 nm radiation. The multispectral digital dermatoscope with a Basler acA1920-25uc camera (RGB color system, resolution ~ 13 μm/pixel) [28] provides image recording in polarized visible light (1920 × 1080, 48 bits, 96 dpi, .tiff).

All measurements of *in vivo RS* spectra were carried out with a spectral resolution of 0.2 nm in the range from 800 to 1000 nm at a signal accumulation time of 60 s. The optical detector was located above the tissue sample at a distance of 7−8 mm. The diameter of the probe radiation beam on the skin was approximately 3 mm. The laser power density on the skin did not exceed 1.56 W/cm^2. Preprocessing of RS spectra included cutting in the range of 860−920 nm, which corresponds to 1114−1874 cm^{-1}, smoothing with a Savitzky-Golay filter and baseline removal in order to eliminate autofluorescence. Registration of dermoscopic images was carried out in polarized illumination mode.

The study protocols were approved by the ethics committee of Samara State Medical University (protocol No. 132 of May 29, 2013). An excisional biopsy was taken for each of the lesions, the diagnosis was established using histological analysis. The dataset contains 65 samples of malignant melanomas (MM), 107 seborrheic keratoses (SK), and 166 nevi (NE). The dermoscopic image set contains 65 MM, 166 NE, and 107 SK. Electronic recourse HAM10K (224 × 224, 24 bits, 96 dpi, .jpeg) with 1113 MM, 6705 NE, and 1099 SK images [29] was used for preliminary training of the neural network.

2.2 Analysis of Raman Spectra by Multivariate Curve Resolution Method

The alternating least squares (ALS) of MCR-ALS GUI 2.0 method [30] was used for reconstruction of concentrations and spectral profiles of skin components. The application of the MCR method for *in vivo* RS spectral analysis allows us to reflect the contribution of the most significant skin components.

As a classification method, we used the gradient boosting algorithm, namely, Light Gradient Boosting Machine (LightGBM) framework. It is an ensemble algorithm based on decision tree models that are sequentially added to the ensemble to correct errors made by previous models [31].

The proposed approach makes it possible to extract important diagnostic information from spectral data that is understandable to the doctor, namely the relative concentrations of the components in the sample.

2.3 Convolutional Neural Network

For the analysis of spatial data, we used a CNN based on a modified Visual Geometry Group 16-layer model (VGG16) architecture (see Fig. 2). We used the Python library Keras to build the CNN architecture. The neural network receives dermoscopic images with dimensions of 224 × 224 pixels as input. The classifier consists of five alternating blocks of Conv2D and MaxPooling2D layers (with ReLU activation function) and fully connected Dense layers as an output. The Conv2D CNN layer performs the convolution operation using a 3 × 3 sliding window method. It slides along the feature map and extracts a three-dimensional feature template with a certain shape (window height, window width, entry depth) at each possible position. MaxPooling2D layers are used for decrease the resolution of the feature map, which reduces the number of trainable parameters. The operating principle of MaxPooling2D is based on selecting the maximum value from the extracted window of the input feature map. In this paper, the window size was 2 × 2, which makes it possible to reduce the resolution by half. At the output, the total number of training parameters was 1,097,345. The sigmoid was used as the activation function at the output layer, the optimizer was Adam.

The data was divided into training, validation, and test sets in a ratio of 8:1:1. It is important to mention that the dermoscopic images dataset may contain arbitrary number of different types of neoplasms, therefore, when forming the training, validation, and test sets, the classes were balanced as follows. The set of the smaller class included all available samples, and the set of the larger class was formed randomly from the available samples of this class. Taking into account the random nature of the sampling, the construction of classification models was carried out at least 10 times, and the results was calculated by averaging the model metrics over the number of experiments performed. Thus, at each stage of constructing a classification model for MM and benign pigmented neoplasms, 65 MM, 26 SK, and 39 NE were used, randomly taken from the data set obtained by the multispectral digital dermatoscope. Since the classes in HAM10K dataset are also unbalanced, the number of images of the smaller class (MM) was increased using various geometric transformations, such as rotation by a random angle, shifts, zooming, etc.

The stability of the resulting models was checked by 10-fold cross-validation. This cross-validation was carried out using the following algorithm: 10% of the objects in the set were excluded from it and became the test set. The model was rebuilt based on the remaining part of the data. Then the excluded part of the objects was returned, random 10% of objects that have not yet been in the test set were again selected as a new test set, and the model was rebuilt again. The cycle was repeated 10 times, and the final performance of the model was calculated as the average of the ten test results obtained. Cross-validation allows one to determine the optimal parameters of the class separation model to avoid overfitting.

The learning process was based on the concept of transfer learning: the network was trained on HAM10K data, then the network was additionally trained on the second set of data obtained by multispectral digital dermatoscope presented in Fig. 1. Additional training was carried out in conditions where the four upper layers are frozen. Freezing the layers is necessary in order to preserve the common features previously identified by the classifier and the resulting weights.

The use of two data sets is due to the small number of images in the data set obtained by multispectral digital dermatoscope and to the difference in the characteristics of the dermoscopic equipment. Training on HAM10K is not enough for the CNN to be able to work with other data, it is necessary to additionally train the network on images recorded by a multispectral digital dermatoscope.

The optimal number of epochs was determined experimentally based on the analysis of accuracy graphs for the training and validation sets. Accuracy was calculated as the proportion of correct responses of the neural network. To analyze what the trained CNN pays attention to when forming a forecast, attention maps were built using the Python library Tensorflow. The areas where CNN pays more or less attention to when forming a diagnosis are highlighted in yellow or blue, respectively.

2.4 Multidimensional Analysis by Logistic Regression

In this research, we attempted a joint analysis of the spectral component features identified by the MCR method and spatial features extracted by a CNN from dermoscopic images. It was proposed to combine classification models at the very last stage where the model receives predicted values for each observation. Thus, we used logistic regression of the predicted values of both models for multidimentional analysis of neoplasms based on their RS derived component compositions and spatial properties of dermoscopic images. ROC AUC was chosen as a scalar characteristic for comparing several models. ROC AUC confidence intervals (CI) were calculated for a probability level of at least 95%.

3 Results and Discussion

3.1 Analysis of Raman spectra by Gradient Boosting Method

Information about the relative component composition of each neoplasm was used as features for recognizing RS spectra. In order to overcome the low accuracy of PLS-DA method for analyzing of MCR resolved RS spectra reported in Ref. [20], it was proposed to use ensemble algorithm LightGBM. As a result of the selection of the LightGBM hyperparameters, the maximum number of leaves was set to 30, and the maximum number of trees did not exceed 100. The stability of the resulting models was checked by 10-fold cross-validation. A binary model for classifying MM versus benign pigmented neoplasms (SK+NE) was constructed (RS model). The ROC curve is shown in Fig. 3 (blue line). Model quality metrics are presented in Table 1. The model shows the accuracy, sensitivity, and specificity of 0.78, 0.77, and 0.80, respectively, and the ROC AUC of 0.82 (0.76−0.89, 95% CI), which is significantly higher compared to the value of 0.69 (0.63−0.76, 95% CI) received by PLS-DA method [10, 20].

Automation of the process of recognizing MM while maintaining the possibility of physical interpretation of the obtained data on the relative composition of the skin area makes the algorithm a candidate for widespread use in decision control systems. However, despite the superiority of the LightGBM model over the results of previous studies, the ROC AUC values do not exceed 0.90. To increase the efficiency of tumor recognition, it is necessary to expand the spectral classification features by implemention of qualitatively new characteristics, which leads us to the analysis of dermoscopic images.

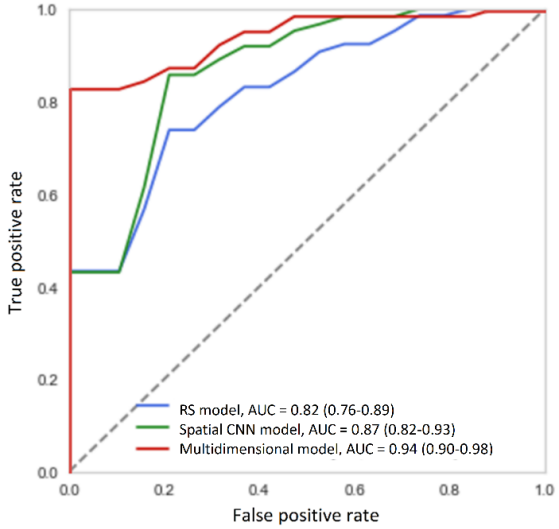


Fig. 3 ROC curves of RS model (blue line), spatial CNN model (green line), and multidimensional model (red line). ROC AUC confidence intervals are calculated for a probability level of at least 95%.

3.2 Analysis of Dermoscopic Images by the Convolutional Neural Network

Using transfer learning approach described above, a CNN classifier for MM versus benign pigmented neoplasms (SK+NE) was constructed (spatial CNN model). As it can be seen from evaluating learning process accuracy graph for preliminary CNN training on HAM10K dataset the model is trained smoothly (Fig. 4a), the number of correctly classified images increases. From attention maps for test images (Fig. 5a), it is noticeable that the neural network trained on the HAM10K dataset pays attention to the tumor boundary, focusing on the size and shape of the object in the decision-making process.

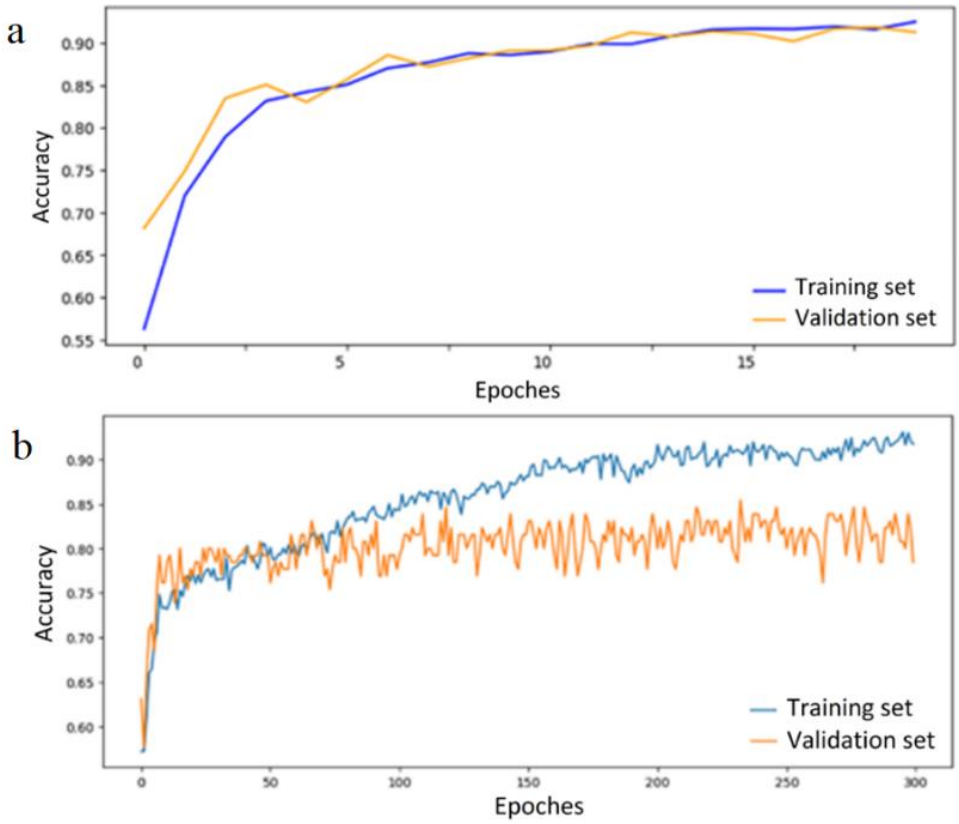


Fig. 4 Accuracy graphs: (a) for the model trained on the HAM10K set, (b) for the model additionally trained on the second data set registered by the experimental system.

Table 1 Quality metrics for the binary classification model of MM and SK+NE.

Models	RS spectra (MCR+LightGBM)	Dermoscopic images (CNN)	Multidimensional analysis (threshold 0.5)	Multidimensional analysis (threshold 0.67)
ROC AUC	0.82 (0.76−0.89, 95% CI)	0.87 (0.82−0.93, 95% CI)	0.94 (0.90−0.98, 95% CI)	
Accuracy	0.78	0.85	0.84	0.87
Sensitivity	0.77	0.85	0.83	0.74
Specificity	0.80	0.85	0.85	1.00

At the next stage, for images recorded using the experimental system, there is a general trend toward increasing accuracy (Fig. 4b), but the model behaves somewhat unstable, which may be due to the small amount of data used for additional training. As for attention maps (Fig. 5b), the model begins to pay attention to the neoplasm itself, assessing not only its shape and size, but also its relief. Taking into account textural features, the neural network analyzes the heterogeneity of tumor growth.

The ROC curve is shown in Fig. 3 (green line). Model quality metrics are presented in Table 1. The use of a CNN in combination with transfer learning and the use of an additional dataset for preliminary training of the CNN allows us to obtain a stable classification model that demonstrates an accuracy of 85%. The model shows sensitivity and specificity of 0.85, and 0.85, respectively, and the ROC AUC of 0.87 (0.82−0.93, 95% CI), which is slightly higher compared to the value of 0.82 (0.76−0.89, 95% CI), obtained by the analysis of RS spectra derived component compositions using the LightGBM method.

3.3 Multidimensional Analysis of Raman Spectra and Dermoscopic Images of Neoplasms

As a result of logistic regression of the predicted values of two independent components composition and spatial CNN models, a joint binary model for classifying MM versus benign pigmented neoplasms (SK+NE) was constructed (multidimentional model). The stability of the resulting combined multidimentional model was tested by 10-fold cross-validation. The ROC curve is shown in Fig. 3 (red line). Model quality metrics are presented in Table 1.

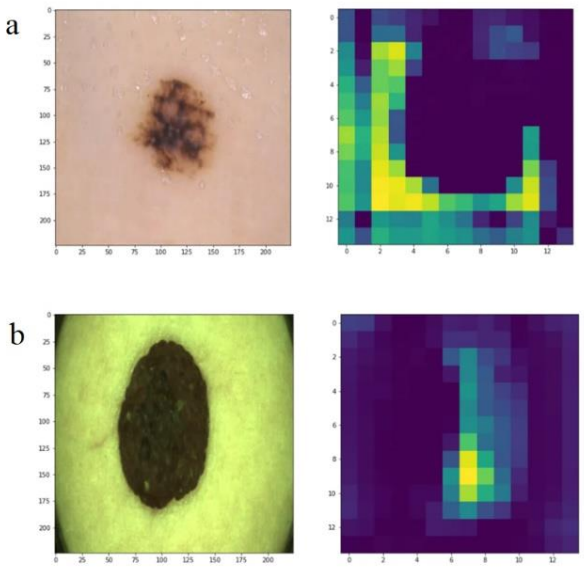


Fig. 5 Attention maps for images from the test set: (a) for the model trained on the HAM10K set, (b) for the model additionally trained on the second set registered by the experimental system (yellow – more attention, blue – less attention). The axes indicate pixels.

Analyzing the presented metrics, one can note the good ability of the classification model using multidimensional analysis to distinguish between MM and SK+NE. The model shows the accuracy, sensitivity, and specificity of 0.84, 0.83, and 0.85, respectively. The quality metrics calculated for the 0.5 threshold are slightly inferior to the results provided by the CNN model. However, these metrics depend on the chosen classification threshold. For a commonly used classification threshold at 0.67 (two-thirds of the maximum possible value), an accuracy of 0.87 and a specificity of 1.00 can be achieved. The obtained result suggests the possibility of the effective use of the described multidimensional method for diagnosing neoplasms in clinical practice in population screening programs, since for the classification case under consideration, the model will not miss any MM, accurately identifies as MM all samples that are really MM. Of course, in this case part of the samples (not more than 25%) will be identified as MM by the model, although in fact they are benign pigmented neoplasms. However, all these cases can be resolved with an in-depth study, which is always carried out when diagnosing MM.

The ROC AUC of the multidimensional model is 0.94 (0.90−0.98, 95% CI), which surpasses the ROC AUC of the RS and spatial CNN models, where the ROC AUC was 0.82 (0.76−0.89, 95% CI) and 0.87 (0.78−0.95, 95% CI), respectively. This means that, in general, the ability of multidimensional model to distinguish between MM and benign pigmented neoplasms is better than that of models based on component analysis by LightGBM method or CNN analysis of dermoscopic images. The latter is explained by the possibility of a multidimensional model to use spatial classification features when prediction by spectral features fails, and vice versa.

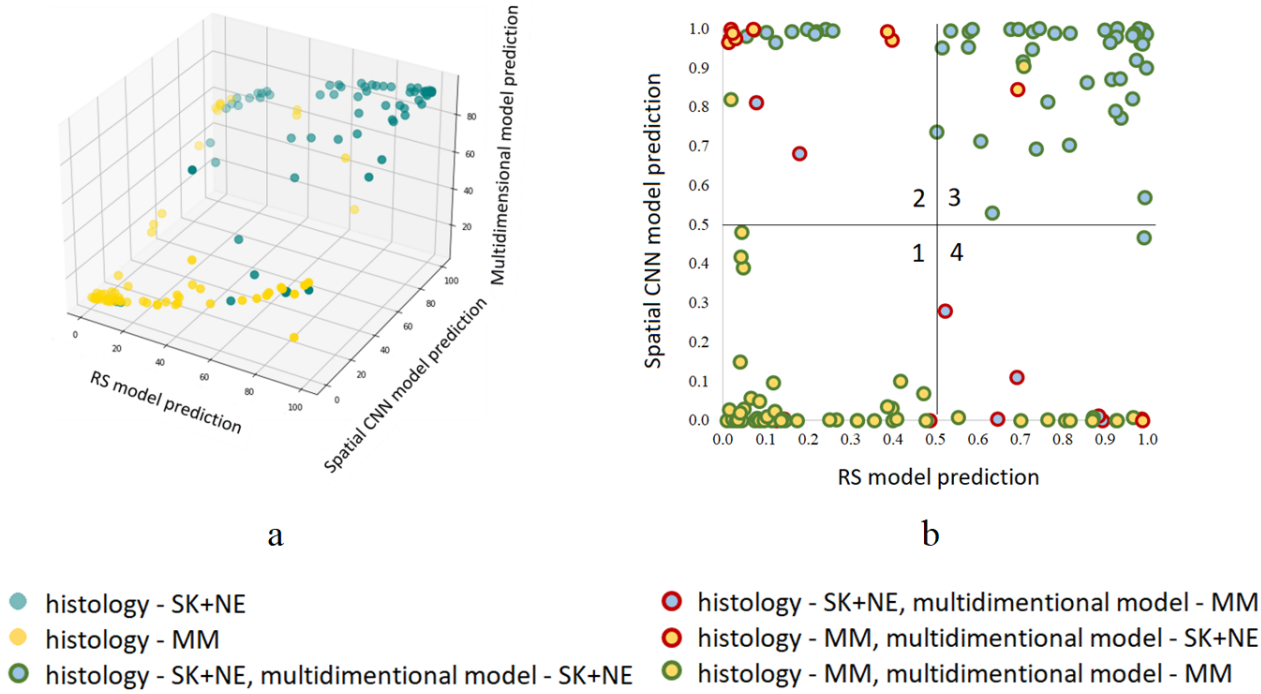


Fig. 6 Scatter diagram of predicted values of designed RS, spatial CNN, and multidimensional models of RS spectra and images: (a) three-dimensional space of the predicted values of all models, (b) projection on prediction plane of RS and spatial CNN models.

This can be easily demonstrated from the analysis of Fig. 6, where the studied neoplasms are shown in the three-dimensional space of the predicted values of the constructed RS, spatial CNN, and multidimensional models. Each marker in Fig. 6a is one of the neoplasms with the coordinates of the predicted values for the models, and its color indicates the true diagnosis of the sample obtained as a result of histological examination: yellow – MM, blue – SK or NE. The predicted values of the models range from 0 to 1, where 0 means MM, and 1 means benign pigmented neoplasms (SK+NE). If the predicted value is less than the threshold value (in this case 0.5), it means that the model classifies the sample as MM; if it exceeds the threshold value, it is classified as SK+NE. The projection of tumor markers onto the prediction plane of the RS and spatial CNN models is shown in Fig. 6b. Here, the outlines of the markers indicate the correctness of determining the diagnosis using a multidimensional model. Samples that were correctly recognized by multidimensional model are circled in green, samples that were incorrectly recognized are circled in red.

As one can see, only a small part of the borderline cases is subject to incorrect classification (when independent RS and spatial CNN models make different decisions, that is, when one model shows a predicted value above the classification threshold, and the other model shows a lower one). These cases are shown in Fig. 6b in the graphs in quadrants 2 and 4. Thus, the multidimensional method allows us to resolve controversial cases when spectral (component compositions) features indicate one diagnosis, and spatial features indicate another, and draw a conclusion about the correct diagnosis.

When comparing the results obtained with other studies, it is worth noting a clear advantage. Thus, in a study [2], the average sensitivity and specificity of 58 dermatologists for the classification of 100 skin lesions was 86.6% (±9.3%) and 71.3% (±11.2%), respectively. This corresponds to a mean ROC AUC of 0.79 (±0.06). Moreover, the average values of sensitivity, specificity and ROC AUC for the expert group are 89% (±9.2%), 74.5% (±12.6%) and 0.82 (±0.06), respectively [2]. Thus, the combined classification model can help ordinary dermatologists to identify skin lesions on average more effectively.

4 Conclusion

The results obtained support the feasibility of multidimensional analysis of multimodal optical skin data, namely RS spectra and dermoscopic images. Combining spatial features of dermoscopic images and the component features identified by the MCR method allows us to preserve the advantages of the physical interpretability of the results of MCR analysis and at the same time allows us to include in the analysis the entire volume of spectral information and textural features of tumors visible on the images.

Due to the complex complementarity of the distinguished spatial, spectral, and component features, the method is characterized by high stability and accuracy with ROC AUC equal to 0.94 (0.90−0.98, 0.95 CI) for the binary classification of MM and benign pigmented neoplasms, which the quality of determining the type of neoplasm is higher when using only spatial features or only spectral and component features by 7% and 12%, respectively.

The developed methods, models, and algorithms of multidimensional analysis make it possible to recognize the type of neoplasm and increase the efficiency of diagnosing skin cancer to a level comparable to or exceeding the efficiency of diagnosing neoplasms by general practitioners and medical specialists by combining spatial, spectral, and component signs.

Acknowledgments

This research was funded by Russian Science Foundation, grant number 21-75-10097.

Disclosures

The authors state no conflict of interest.

References

1. J. Ferlay, M. Colombet, I. Soerjomataram, D. M. Parkin, M. Piñeros, A. Znaor, and F. Bray, "Cancer statistics for the year 2020: An overview," International Journal of Cancer 149(4), 778–789 (2021).
2. H. A. Haenssle, C. Fink, R. Schneiderbauer, F. Toberer, T. Buhl, A. Blum, A. Kalloo, A. Ben Hadj Hassen, L. Thomas, A. Enk, and L. Uhlmann, "Man against machine: diagnostic performance of a deep learning convolutional neural network for dermoscopic melanoma recognition in comparison to 58 dermatologists," Annals of Oncology 29(8), 1836–1842 (2018).
3. E. Borisova, D. Ivanov, B. Kolev, T. Genova, V. Mircheva, S. Ilyov, L. Zaharieva, I. Lihachova, A. Lihachovs, J. Spigulis, and P. Troyanova, "Autofluorescence spectroscopy of cutaneous neoplasia under ultraviolet, visible and near infrared excitation," Tissue Optics and Photonics 11363, 100–104 (2020).
4. G. Lentsch, E. G. Baugh, B. Lee, M. Aszterbaum, C. B. Zachary, K. M. Kelly, and M. Balu, "Research techniques made simple: emerging imaging technologies for noninvasive optical biopsy of human skin," Journal of Investigative Dermatology 142(5), 1243–1252 (2022).
5. M. Mogensen, L. Thrane, T. M. Jørgensen, P. E. Andersen, and G. B. Jemec, "OCT imaging of skin cancer and other dermatological diseases," Journal of Biophotonics 2(6–7), 442–451 (2009).

6. V. O. Vinokurov, I. A. Matveeva, Y. A. Khristoforova, O. O. Myakinin, I. A. Bratchenko, L. A. Bratchenko, A. A. Moryatov, S. G. Kozlov, A. S. Machikhin, I. Abdulhalim, and V. P. Zakharov, "Neural network classifier of hyperspectral images of skin pathologies," Computer Optics 45(6), 879–886 (2021).
7. J. Popp, C. Krafft, and T. Mayerhöfer, "Modern Raman spectroscopy for biomedical applications: A variety of Raman spectroscopical techniques on the threshold of biomedical applications," Optik & Photonik 6(4), 24–28 (2011).
8. A. Mahadevan-Jansen, R. R. Richards-Kortum, "Raman spectroscopy for the detection of cancers and precancers," Journal of Biomedical Optics 1(1), 31–70 (1996).
9. Z. Huang, H. Lui, X. K. Chen, A. Alajlan, D. I. McLean, and H. Zeng, "Raman spectroscopy of in vivo cutaneous melanin," Journal of Biomedical Optics 9(6), 1198–1205 (2004).
10. I. A. Bratchenko, L. A. Bratchenko, A. A. Moryatov, Y. A. Khristoforova, D. N. Artemyev, O. O. Myakinin, A. E. Orlov, S. V. Kozlov, and V. P. Zakharov, "In vivo diagnosis of skin cancer with a portable Raman spectroscopic device," Experimental Dermatology 30(5), 652–663 (2021).
11. V. P. Zakharov, L. A. Bratchenko, Y. A. Khristoforova, O. O. Myakinin, D. N. Artemyev, A. A. Moryatov, S. V. Kozlov, E. G. Borisova, T. I. Genova, P. P. Troyanova, and I. A. Bratchenko, "Multiparametric spectral diagnosis of skin cancer," Tissue Optics and Photonics 11363, 105–110 (2020).
12. M. Wu, B. Gao, and X.Wei, "Recent advances in Raman spectroscopy for skin diagnosis," Journal of Innovative Optical Health Sciences 16(03), 2330003 (2023).
13. R. Luo, J. Popp, and T. Bocklitz, "Deep learning for Raman spectroscopy: A review," Analytica 3(3), 287–301 (2022).
14. I. A. Bratchenko, L. A. Bratchenko, Y. A. Khristoforova, A. A. Moryatov, S. V. Kozlov, and V. P. Zakharov, "Classification of skin cancer using convolutional neural networks analysis of Raman spectra," Computer Methods and Programs in Biomedicine 219, 106755 (2022).
15. T. Azzouz, R. Tauler, "Application of multivariate curve resolution alternating least squares (MCR-ALS) to the quantitative analysis of pharmaceutical and agricultural samples," Talanta 74(5), 1201–1210 (2008).
16. J. Felten, H. Hall, J. Jaumot, R. Tauler, A. De Juan, and A. Gorzsás, "Vibrational spectroscopic image analysis of biological material using multivariate curve resolution–alternating least squares (MCR-ALS)," Nature Protocols 10(2), 217–240 (2015).
17. H. Noothalapati, K. Iwasaki, and T. Yamamoto, "Biological and medical applications of multivariate curve resolution assisted Raman spectroscopy," Analytical Sciences 33(1), 15–22 (2017).
18. I. A. Matveeva, O. O. Myakinin, Y. A. Khristoforova, I. A. Bratchenko, E. N. Tupikova, and V. P. Zakharov, "Possibilities for decomposing Raman spectra of amino acids mixture by Multivariate Curve Resolution (MCR) analysis," Proceedings of SPIE 11582, 115821G (2020).
19. I. A. Matveeva, L. A. Bratchenko, O. O. Myakinin, E. N. Tupikova, and V. P. Zakharov, "The Effect of Noise in Raman Spectra on the Reconstruction of the Concentration of Amino Acids in the Mixture by Multivariate Curve Resolution (MCR) Analysis," Journal of Biomedical Photonics & Engineering 7(2), 020309 (2021).
20. I. Matveeva, I. Bratchenko, Y. Khristoforova, L. Bratchenko, A. Moryatov, S. Kozlov, O. Kaganov, and V. Zakharov, "Multivariate curve resolution alternating least squares analysis of in vivo skin Raman spectra," Sensors 22(24), 9588 (2022).
21. V. V. Tuchin, J. Popp, and V. Zakharov (Eds.), Multimodal optical diagnostics of cancer, Springer International Publishing (2020). ISBN: 978-3-030-44593-5. ISBN: 978-3-030-44594-2.
22. X. Feng, A. J. Moy, H. T. Nguyen, J. Zhang, M. C. Fox, K. R. Sebastian, J. S. Reichenberg, M. K. Markey, and J. W. Tunnell, "Raman active components of skin cancer," Biomedical Optics Express 8(6), 2835–2850 (2017).
23. T. J. Brinker, A. Hekler, A. H. Enk, C. Berking, S. Haferkamp, A. Hauschild, M. Weichenthal, J. Klode, D. Schadendorf, T. Holland-Letz, C. von Kalle, S. Fröhling, B. Schilling, and J. S Utikal, "Deep neural networks are superior to dermatologists in melanoma image classification," European Journal of Cancer 119, 11–17 (2019).
24. A. Mahbod, G. Schaefer, I. Ellinger, R. Ecker, A. Pitiot, and C. Wang, "Fusing fine-tuned deep features for skin lesion classification," Computerized Medical Imaging and Graphics 71, 19–29 (2019).
25. A. Takiddin, J. Schneider, Y. Yang, A. Abd-Alrazaq, and M. Househ, "Artificial intelligence for skin cancer detection: scoping review," Journal of Medical Internet Research 23(11), e22934 (2021).
26. A. Esteva, B. Kuprel, R. A. Novoa, J. Ko, S. M. Swetter, H. M. Blau, and S. Thrun, "Dermatologist-level classification of skin cancer with deep neural networks," Nature 542(7639), 115–118 (2017).
27. Y. A. Khristoforova, I. A. Bratchenko, O. O. Myakinin, D. N. Artemyev, A. A. Moryatov, A. E. Orlov, S. V. Kozlov, and V. P. Zakharov, "Portable spectroscopic system for in vivo skin neoplasms diagnostics by Raman and autofluorescence analysis," Journal of Biophotonics 12(4), e201800400 (2019).
28. S. G. Konovalov, O. A. Melsitov, O. O. Myakinin, I. A. Bratchenko, A. A. Moryatov, S. V. Kozlov, and V. P. Zakharov, "Dermatoscopy software tool for in vivo automatic malignant lesions detection," Journal of Biomedical Photonics & Engineering 4(4), 040302 (2018).
29. Kaggle, A large collection of multi-source dermatoscopic images of pigmented lesions "Skin Cancer MNIST: HAM10000," (accessed 29 February 2024). [https://www.kaggle.com/datasets/kmader/skin-cancer-mnist-ham10000].

30. J. Jaumot, A. de Juan, and R. Tauler, "MCR-ALS GUI 2.0: New features and applications," Chemometrics and Intelligent Laboratory Systems 140, 1–12 (2015).
31. "LightGBM," (accessed 29 February 2024). [https://lightgbm.readthedocs.io/en/latest/index.html].

Improving the Detection of Blood on Poultry Meat Based Colorimetry Using a Camera

Koekoeh Santoso[1*], Hadri Latif[1], La Jumadin[2], and Putri Gusfani Wida[1]

[1] School of Veterinary Medicine and Biomedical Sciences, IPB University, Bogor 16680, Indonesia

[2] Department of Biology Education, Faculty of Teacher Training and Education, HaluOleo University, Kendari 93231, Indonesia

***e-mail:** koekoehipb@gmail.com

Abstract. The purpose of this study was to measure blood levels in quail meat with a cellphone camera using a spectrophotometer as a standard. Samples were obtained from 9 pieces of quail meat cut by hanging, 9 pieces of quail meat cut without hanging, 9 pieces of quail carcass dead for 4 h, and 9 pieces of quail carcass dead for 8 h. The relative concentration of blood in the meat of the quail carcass with or without hanging measured on 430 nm with spectrophotometer after 4 h and 8 h were 0.0149%, 0.0165%, 0.0173%, and 0.0177%, respectively. Since the absorption coefficient of the main blood absorber namely hemoglobin differs significantly in the violet and red spectral regions, the time dependence of the absorption intensity obtained by spectrophotometer was compared with a similar dependence of the blue channel of a smartphone, measured using ImageJ. It has been shown that measurements by the smartphone have a similar tendency as the measurements of the spectrophotometer, and they can be used as indicators of blood concentration threshold in quail meat, and, as a consequence, determine the duration of this procedure. © 2024 Journal of Biomedical Photonics & Engineering.

Keywords: carrion; colorimetry; digital image; ImageJ; quail.

Paper #9008 received 11 Aug 2023; revised manuscript received 31 Dec 2023; accepted for publication 31 Dec 2023; published online 29 Mar 2024. doi: 10.18287/JBPE24.10.010308.

1 Introduction

Quail are livestock that produce meat and eggs as a source of animal protein [1]. The perfect bleeding process can be seen by looking at the hemoglobin parameters in the carcass. Hemoglobin levels can be determined using the spectrophotometer method.

The UV-Vis spectrophotometry method has the advantage that the results obtained are quantitative so that the results can be more accurate [2]. The spectrophotometric method uses monochromatic light to observe changes in the clarity of the blood-Ethylen Diamine Tetra Acetic Acid (blood-EDTA) boundary at one point, namely the top part, which is recorded in the form of absorbance values. Light absorbance values that gradually change indicate changes in the concentration in blood plasma [3]. The light absorbance spectrum stores cellular interaction information that describes the erythrocyte aggregation process. The absorbance spectrum can be analyzed using the Principal Component Analysis (PCA) method, which is a calculation used for data analysis in multidimensional data sets, especially in the field of graphics. PCA reduces information without having to eliminate the main information by finding eigenvalues and eigenvectors to obtain covariance and correlation values between dimensions in data [4]. The spectrophotometer uses serum or plasma as an object of registration, so it is not influenced by blood cells like in whole blood samples [5]. The use of a spectrophotometer requires preparation of serum samples, so it requires more blood and the process takes a long time.

There is an alternative method to determine the color intensity in a solution, namely the digital imaging method using a camera [6]. The camera measures electromagnetic radiation from colored zones via the camera sensor [7]. Digital imaging methods with cameras are capable of detecting objects, and role of camera sensors is to capture the color of an object and convert

visual data into digital data, which can be processed [8]. The algorithm of the camera processes information to produce output values red (R'), green (G'), and blue (B') from the actual red (R), green (G), and blue (B) values [7]. The color resulting from the malachite green test then are captured by the camera and visualized. The resulting camera image is then processed using an image processor, namely ImageJ [9]. This research is expected to be able to show the potential of cameras to measure blood concentration in quail meat based on calorimetry carried out with a spectrophotometer as the standard.

2 Materials and Methods

Equipment and sample preparation were carried out at the Physiology Laboratory, Department of Anatomy, Physiology, and Pharmacology, School of Veterinary Medicine and Biomedical, Bogor Agricultural University. Quail meat samples were obtained from the Observation Laboratory of the Department of Anatomy, Physiology, and Pharmacology, School of Veterinary Medicine and Biomedical Medicine, Bogor Agricultural University.

This study used a completely randomized design with factors of quail slaughtered by hanging, not hanging, and quail carcasses which were kept for 4 h and 8 h. The number of quail was calculated using the Federer formula $(t-1)\ (n-1) \geq 15$ We used 36 quails: 9 slaughtered by hanging process, 9 slaughtered without hanging process, 9 carcasses that were kept for 4 h, and 9 carcasses that were kept for 8 h.

The difference in the treatment of the carcasses that were kept for 4 h and 8 h before measuring blood concentrations, was based on the lag time required between slaughtering and selling poultry in the market which usually takes 4 to 8 h.

Before examination of the sample, a standard curve is made as a reference for the results. The standard curve was prepared from $FeCl_3$ in distilled water, then diluted again in HCl.

Quails that were slaughtered by hanging and not hanging were taken from the thigh, then cut into small pieces and soaked in distilled water for 30 min. The extract was centrifuged at 3000 rpm for 10 min, then the precipitate and liquid were separated. Quail carcasses were kept for 4 h and 8 h, then subjected to the same treatment as quails that were slaughtered by hanging or not hanging. The extract used is from the liquid part.

The meat extract was reacted with malachite green and H_2O_2 then homogenized using a vortex and left for 20 min so that the reaction took place perfectly. After 20 min $KMnO_4$ was added to stop the reaction and then it was homogenized again using a vortex.

The results were registered with a spectrophotometer after adding $KMnO_4$. Scanning is also performed using a digital camera in the microplate. Digital camera calibration begins with extracting feature points in the video, then tracing them throughout the video. The movement of these points is then minimized using the objective function and changing the camera parameters, and in this way, a set of calibrated parameters is obtained [9]. The sample to which $KMnO_4$ had been added was mesured using a spectrophotometer, then the sample was transferred to a microplate using a micropipette at 0.2 mL/well. The microplate was placed on the scanner and closed using a mobile camera Scanjet XPA. Image scanning using a scanner is carried out from under the microplate. The microplate when using a mobile camera is placed on top of the mobile camera Scanjet XPA and then covered with a wooden box. Taking images using a mobile camera is done from above the microplate. Images that have been scanned with a scanner are saved in Tagged Image File Format (TIFF) format and images taken by mobile cameras are saved in Joint Photographic Experts Group (JPEG) format.

The images were processed using image processing software ImageJ obtained from the plate wells. ImageJ represents the color component in pixels and converts it to numbers in the RGB color component. The intensity of the color obtained is translated into absorbance by the Lambert-Beer law. Next, the absorbance value is entered into the equation of the standard curve obtained so that the concentration of blood in the meat is known.

The UV-VIS Spectrophotometer calibration procedure refers to the procedures of the 2020 National Directorate of Thermoelectric and Chemical Measurement Units. The calibration procedure consists of 3 stages, namely initial inspection, equipment preparation, and calibration. The initial inspection stage begins with carrying out a visual inspection, checking the stray radiant energy (SRE) value using an SRE filter in the 200 nm to 450 nm area, measuring baseline flatness and noise from the instrument, as well as monitoring and recording the environmental temperature around the spectrophotometer. The equipment preparation stage is carried out by cleaning the standard filters used either using an air blower or with a lint-free cloth (microfiber). The calibration stage begins with turning on the instrument for 30−60 min, setting the wavelength scanning range from 240 nm to 650 nm, setting the slit size, paying attention to the wavelength scanning distance (interval/step), and repeating the measurement 9 times.

Using ImageJ for particle analysis requires the definition of the part of the image which is an object/particle and the part of the image which is the background. It is referred to as image segmentation. This can be done using Image > Adjust > Threshold. By setting the Threshold level, you can adjust the brightness level of the image for the definition of objects/particles and their background. After the Threshold adjustment is made, the measurement of the size/area of the intended particle can be carried out by the particle analysis feature in ImageJ. Particle analysis in ImageJ can be done by clicking Analyze > Set Measurements to determine what output you want in particle analysis. Then particle analysis is done by clicking Analyze > Analyze Particles.

Data were analyzed quantitatively using Microsoft Excel 2010 to obtain concentration. The results of the concentrations were analyzed statistically by comparing blood concentrations in meat slaughtered by hanging, not

hanging, carcass meat which was kept for 4 h and 8 h using a spectrophotometer and a camera, then analyzed using the descriptive one-way ANOVA (analysis of variance)) method.

3 Results and Discussion

3.1 Quail Blood Concentration Measurement with a Spectrophotometer

Measurement of the concentration of quail blood samples was carried out using a spectrophotometer. The standard spectrophotometer calibration curve is obtained by measuring the absorbance of a standard solution at a wavelength of 430 nm. Based on the measurement results of the standard spectrophotometer solution, the standard spectrophotometer calibration curve is obtained as shown in Fig. 1.

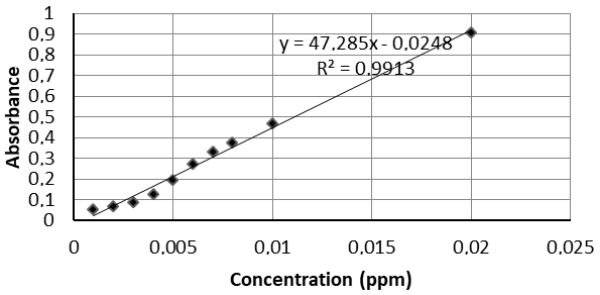


Fig. 1 Spectrophotometer standard calibration curve at an absorbance wavelength of 430 nm.

The standard curve shows the relationship between the concentration of the solution (x-axis) and the absorbance of the solution (y-axis). The regression line equation serves to determine the mathematical model used to predict one variable from another. While the correlation coefficient shows the relationship between concentration and absorbance. Based on the calibration curve above, the regression line equation is $y = 47.285x - 0.0248$ with a correlation coefficient of 0.9913. This shows that there is a positive correlation between concentration and absorbance. The concentration increases, the absorbance value also increases [10]. The correlation value is considered good if it is more than 80% ($R^2 \geq 0.80$) [11]. The largest R^2 value is 1, and the smallest is −1, so that it can be written as $-1 \leq R^2 \leq 1$. For $R = 1$, it is called a perfect positive relationship and the direct linear relationship is very high.

3.2 Image Processing Program for Measuring Quail Blood Concentration with a Smartphone Camera Using ImageJ

Mobile phone cameras can capture color, which in principle is a derivative of the colorimetric analysis method. Images taken using a cellphone camera are saved in the JPEG format, which is an image with subtle color changes [6]. The results of taking images with the camera can be seen in Fig. 2.

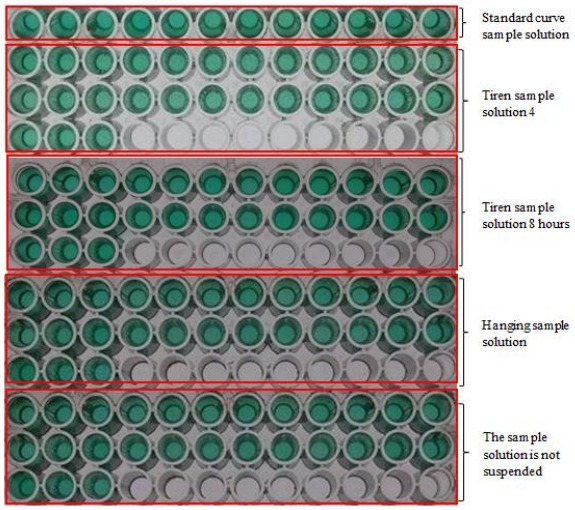


Fig. 2 Camera results from the microplate.

The compiled image processing program can determine the image parameters of objects analyzed through color images, namely the RGB color index. The RGB color index is analyzed using the help of ImageJ software and collected using Microsoft Office Excel 2013 to obtain the distribution of three indices. The ImageJ program automatically calculate, and the resulting data may be selected through the Regions of Interests (ROI) manager. The ROI manager contains a list of analyzes and the ROI manager function can help in selecting the quality of the calculated results. The standard camera calibration curve is described in Fig. 3.

The cellphone camera calibration curve (see Fig. 2) has different tilt angles for R, G, B. Of course, hemoglobin has a different absorption coefficient at different wavelengths, but it remains constant. Therefore, the calibration lines R, G, B can be different, but the angle of inclination must be the same. The fact that the angles are different means that the measurement scheme and spectral device characteristics have a great influence on the results.

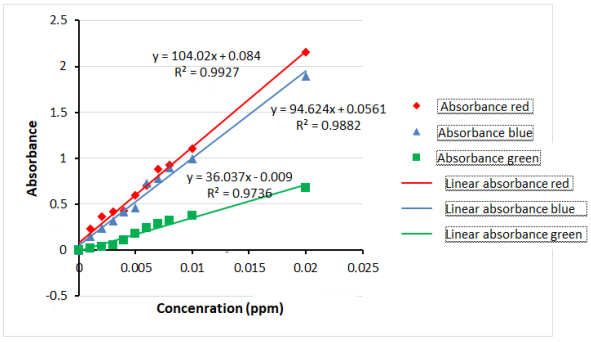


Fig. 3 Cellphone camera calibration curve.

Based on the calibration curve above, it was shown that the RGB channel produces different regression value equations and correlation coefficients. The correlation coefficients of each RGB channel are $y = 104.02x + 0.0084$, $y = 94.624x + 0.0561$, and

$y = 36.037x - 0.009$ with correlation coefficients $R^2 = 0.9927$, $R^2 = 0.9882$, and $R^2 = 0.9736$, respectively. This shows that there is a positive correlation between concentration and absorbance. The curve that has the steepest slope indicates that the curve is most sensitive to changes in concentration. Based on the calibration curve (see Fig. 3), the red curve was chosen for further calculations because of the larger correlation coefficient with better linearity which is reflected in the steeper shape of the curve. This is because when the sample solution is exposed to light, the camera will capture more light reflected by the red complement so that the absorbed color has the highest value. Sample solution and sample concentration have a linear relationship with absorbance. Absorbance is directly proportional to the concentration according to the application of the Beer-Lambert law in absorbance measurements.

3.3 Comparison of Quail Blood Concentration Measurements Using Spectrophotometers and Mobile Cameras

In this study, colorimetric measurements using spectrophotometry and image processing using cellphone cameras have the same measurement principle, namely measuring the wavelengths reflected by the sample. However, in the process of measuring these two tools have differences. The color value obtained from the capture of the wavelength by the spectrophotometer is the wavelength reflected by one surface area. Meanwhile, the color value obtained with the help of ImageJ is the color value captured by a digital camera from the reflection of the wavelength by the cellphone camera from a small portion of the surface area. A comparison of blood concentration in the carcass and non-carcass quail meat can be seen in Table 1.

The results obtained using the spectrophotometer show a significant difference ($p < 0.05$) between the slaughtered quail meat group and the carcass quail meat group. The value of blood concentration in carcass meat was greater than in the group of slaughtered quails hanging and slaughtered not hanging. The carcass sample smells bad, so the sample has produced H_2S [12]. The myoglobin content of the carcass samples was more than that of the quail samples which were slaughtered by hanging or not, so the concentration numbers were lower than those of the live samples. This is caused by several factors which are the disadvantages of digital imaging. First, the lighting system consists of lighting coming from the scanner which affects the intensity of the light produced. If the resulting color is weaker or stronger, it will affect the subtracting number for calculating the difference in absorbance in the quail meat solution. The absorption value in the solution obtained for carcass and non-carcass quail meat depends not only on blood concentrations, but also on other products. The turbidity of the solution increased over time, indicating an increase in other components in the solution. In this case, the results shown in Table 1 are not only interpreted as changes due to changes in blood concentration, but as changes due to an increase in the amount of other impurities. Indirectly this is evidenced by the presence of smell.

Blood concentration and absorbance are the ratios of the intensity of the absorbed light to the intensity of the incident light. This absorbance value depends on the levels of substances contained in a sample, the more molecules absorb light at a certain wavelength so that the absorbance value is greater, or in other words, the absorbance is directly proportional to the concentration of the substance contained in a sample. The graph of the relationship between the absorbance values obtained using the spectrophotometer and using a cellphone camera is presented in Fig. 4.

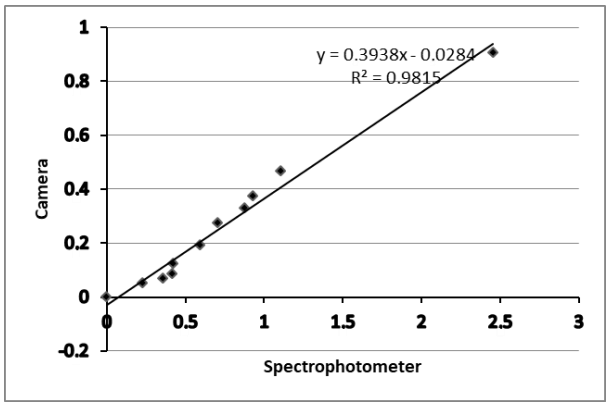


Fig. 4 The relationship between the absorbance value of the spectrophotometer and digital image processing.

Table 1 Concentration of blood in quail meat (%).

Treatment	Spectrophotometer	Mobile Camera
Slaughter hanged	0.0149 ± 0.00108^a	0.0022 ± 0.00007^a
Slaughter is not hung	0.0165 ± 0.00078^b	0.0051 ± 0.00064^b
Carcass 4 h	0.0173 ± 0.00135^c	0.0062 ± 0.00065^c
Carcass 8 h	0.0177 ± 0.00183^c	0.0067 ± 0.00043^d

Note: Different superscript letters (a, b, c, d) in the same column indicate a significant difference.

From the graph on Fig. 4, the regression equation $y = 0.3938x - 0.0284$ is obtained with a correlation coefficient value of 0.9815. The absorbance value of solution obtained using the standard spectrophotometer with the measurement results of digital image processing has a high positive correlation with the absorbance value of a digital camera with a correlation value of more than 0.9. This shows a very strong relationship. This regression value can explain the changes in the value of the variable y (actual lab value). The absorption of hemoglobin in the violet region of the spectrum (430 nm) differs significantly (by two orders of magnitude) from the absorption in the red region. Therefore, it will be correct to compare the dependencies obtained from the spectrophotometer (430 nm) with the smartphone calibration curve in the blue channel. As can be seen from the comparison in Figs. 2 and 3, they differ significantly.

4 Conclusions

Measurements using smartphone are indicative, namely, they allow one to determine the duration for a certain threshold of relative blood concentration in the meat of suspended quails.

Disclosures

The authors declare that they have no conflict of interest.

References

1. L. Jumadin, H. Maheshwari, N. Ulupi, and A. S. Satyaningtijas, "Physiological performance and productivity of japanese quail supplemented with cassava leaf paste," Tropical Animal Science Journal 45(4), 460–466 (2022).
2. N. S. Lestari, K. A. Nugroho, and N. Ngadikun, "Deteksi tumor payudara (breast benign diseases) berdasar interaksi eritrosit akibat perubahan ion–ion dalam darah–edta menggunakan spektrofotometer UV–Vis," Journal for Physics Education and Applied Physics 5(1), 47–61 (2023).
3. K. A. Nugroho, K. Abraha, and N. Ngadikun, "The mechanism of erythrocytes aggregation in EDTA–blood of ovarian cancer patients viewed by Coulomb's law," International Journal on Advanced Science, Engineering and Information Technology 7(6), 2175–2182 (2017).
4. I. T. Jollife, J. Cadima, "Principal component analysis: A review and recent developments," Philosophical Transactions of the Royal Society A: Mathematical, Physical and Engineering Sciences 374 (2065), 20150202 (2016).
5. V. L. Stevens, E. Hoover, Y. Wang, and K. A. Zanetti, "Pre–analytical factors that affect metabolite stability in human urine, plasma, and serum: a review," Metabolites 9(8), 156 (2019).
6. T. Gregory, M. P. Edgar, G. M. Gibson, and P. A. Moreau, "Computational version of the correlation light–field camera," Scientific Reports 12(1), 21409 (2022).
7. E. Stanev, M. Dencheva, "Calorimetry in Allergy Diagnostic," Intech Open (2022).
8. A. A. Abdulsahib, M. A. Mahmoud, M. A. Mohammed, H. H. Rasheed, S. A. Mostafa, and M. S. Maashi, "Comprehensive review of retinal blood vessel segmentation and classification techniques: Intelligent solutions for green computing in medical images, current challenges, open issues, and knowledge gaps in fundus medical images," Network Modeling Analysis in Health Informatics and Bioinformatics 10, 1–32 (2021).
9. K. Kesonkan, C. Yeerum, K. Kiwfo, K. Grudpan, and M. Vongboot, "Green downscaling of solvent extractive determination employing coconut oil as natural solvent with smartphone colorimetric detection: demonstrating the concept via Cu(II) assay using 1,5–Diphenylcarbazide," Molecules 27(23), 8622 (2022).
10. W. Hallén, "Automatic Calibration of Camera Parameters: A Steppingstone to Analysing Videos," Student thesis, Uppsala Universitet (2022).
11. E. C. Chao, "Islam and veterinary science: rethinking animal suffering through islamic animal ethics and the evolving definition of halal slaughter," Frontiers in Veterinary Science 9, 785585 (2022).
12. F. A. Noraldin, A. B. Sabow, "Bleeding efficiency, carcass characteristics and meat quality assessments in broiler chickens subjected to different pre-slaughter restraining methods," Research Square, 1–22 (2022).

The Assessment of Photo-Induced Toxicity of [$NaYF_4$:Yb^{3+}, Er^{3+}] Upconversion Nanoparticles on Model Normal and Cancer Cell Lines *in Vitro*

Irina Yu. Yanina[1,2,3*], Roman A. Verkhovskii[4], Nikita A. Navolokin[5,6], and Vyacheslav I. Kochubey[1,3]

[1] Institute of Physics, Saratov State University, 83 Astrakhanskaya str., Saratov 410012, Russian Federation
[2] Science Medical Center, Saratov State University, 83 Astrakhanskaya str., Saratov 410012, Russian Federation
[3] Laboratory of laser molecular imaging and machine learning, Tomsk State University, 36 Lenin's av., Tomsk 634050, Russian Federation
[4] Remote Controlled Theranostic Systems Lab, Science Medical Center, Saratov State University, 83 Astrakhanskaya str., Saratov 410012, Russian Federation
[5] Department of Pathological Anatomy, Saratov State Medical University, 112 B Kazachaya str., Saratov 410012, Russian Federation
[6] Pathological Department, State Healthcare Institution "Saratov City Clinical Hospital No. 1 named after Yu. Ya. Gordeev", 19 str. named after A. I. Kholzunova, Saratov 410017, Russian Federation

*e-mail: irina-yanina@list.ru

Abstract. Upconversion nanoparticles (UCNPs) are promising alternatives to traditional fluorescent labels for cell imaging that have outstanding potential in biological and clinical applications. As we previously established, the co-incubation of synthesized in-house [$NaYF_4$:Yb^{3+}, Er^{3+}] UCNPs uncoated and coated by SiO_2 shell with the cell lines resulted in particles' uptake. Because of the tendency to particle internalization by cells, the assessment of the biocompatibility of UCNPs intended for biomedical applications and their ability to induce desirable biological effects under the appropriate wavelength irradiation is an important step in UCNPs development. The present work is focused on the assessment of [$NaYF_4$:Yb^{3+}, Er^{3+}] UCNPs' phototoxicity and changes in human lung-derived embryonic fibroblast (FLEH-104) and human laryngeal epidermoid carcinoma (Hep-2) cell lines' morphology in response to the influence of UCNPs. © 2024 Journal of Biomedical Photonics & Engineering.

Keywords: cell lines; upconversion nanoparticles; luminescence; phototoxicity; laser; NIR.

Paper #9046 received 15 Dec 2023; revised manuscript received 19 Mar 2024; accepted for publication 19 Mar 2024; published online 31 Mar 2024. doi: 10.18287/JBPE24.10.010309.

1 Introduction

Cancer is the leading cause of mortality worldwide and a significant factor hindering life expectancy growth. According to the World Health Organization statistics from 2019, cancer ranks as the primary or secondary contributor to mortality under the age of 70 in 112 out of 183 countries [1, 2]. Therefore, the development of new methods for cancer diagnostics and therapy at early stages and the amendment of currently existing ones are top priorities for modern medicine.

Currently, conventional surgery remains one of the most commonly used approaches for tumor removal. However, tumor surgery is accompanied by a substantial risk of malignant cells remaining in the surgery site, which can later result in the disease recurrence [3]. Radiotherapy and chemotherapy are also commonly used approaches, however, the resistance of some tumors to these types of therapy can also result in the treatment failure or even disease relapsing [4, 5]. Besides, conventional approaches to cancer therapy possess multiple undesirable side effects including off-target

toxicity of chemotherapeutic agents affecting healthy organs, tissues, and cells. Targeted therapy, which aims to affect only tumor cells, represents an alternative direction in the development of anticancer remedies [6−10]. The application of monoclonal antibodies targeting tumor-specific antigens [11], and oligonucleotide aptamers targeting different tumor-specific structures including gens [12, 13] are illustrative examples of this therapy realm.

The early-stage cancer diagnostics is crucial for therapy success and facilitates the chances of long-term patient survival. The usage of optical methods for cancer diagnostics deserves close attention. For the last two decades, label-free optical methods have been capturing the interest of researchers [14−16]. Differences in fluorescence level of endogenous fluorophores and morphology of normal and malignant cells are pillars of label-free approaches. Whereas exogenous fluorophores' usage for cancer cell labeling is a more conventional approach and, currently, is widely used in clinic [17−19]. The selective labeling of cancer-specific structures within malignant cells or on their surface by fluorophores, conjugated with molecules providing cancer-targeting, is the grounds of this technique [8−9, 20, 21].

The successful experience of selective fluorescent labeling application in clinic encourages researchers to search for new natural fluorophores and develop new synthetic fluorophores and nanostructures possessing fluorescent properties [22−28].

Many types of luminophores are currently used in bioimaging (e.g. quantum dots, fluorescent proteins, organic dyes, dye-doped silica nanoparticles, metallic nanoparticles). However, the use of organic probes for luminescence imaging of living organisms has some limitations. Excitation of traditional bio-labels usually requires UV or VIS light, which results in low signal-to-noise ratio due to high biological autofluorescence, low light penetration depth and possible cell photodamage. Therefore, it is desirable to use fluorescent bio-labels that can be excited by near-infrared light. Compared with organic dyes and semiconductor quantum dots, upconversion nanoparticles have attractive chemical and optical properties, such as low toxicity, sharp emission bandwidths, large anti-Stokes shifts and high resistance to photobleaching and photoblinking. NIR light can non-invasively penetrate deep into living organisms because the excitation wavelength is within the optical transparency window of tissues (700−1000 nm).

From the viewpoint of the elaboration of exogenous fluorescence labels, nanomaterials have attracted great interest due to their unique physical and chemical properties. So, fluorescent semiconductor quantum dots possess larger photon action areas than organic fluorophores (>1,000 GM compared to 1,300 GM for organic fluorophores) (1 GM = 10^{-50} $cm^4 s$ $photon^{-1}$) [29]. However, quantum dots mostly comprise heavy metals characterized by substantial toxicity [30] which significantly obstruct their introduction to clinical practice. Gold nanoparticles also have a large photon action area (greater than 2000 GM for gold nanorods), however, in contrast to quantum dots, they are biocompatible, which is crucial for their biomedical applications [27, 31]. The other promising class of nanoscale luminophores is rare-earth-doped upconversion nanoparticles (UCNPs) capable of converting longer wavelength near-infrared radiation into visible one via a nonlinear optical process [32]. The unique NIR-induced photoluminescence properties of UCNPs benefit bioimaging through the image contrast improvement via avoiding tissue autofluorescence, and through the increased labels' photostability, ensuring prolonged imaging even at the single nanoparticle level [16−21]. These make UCNPs attractive for application in biological sensing, biomedical imaging, and disease theranostics [33−38].

Thus, UCNPs are promising alternatives to traditional fluorescent biolabels for cell imaging and have outstanding potential in biological and clinical applications such as photodynamic therapy (PDT). In this therapy, reactive oxygen species (ROS) are used as a lethal factor. In the traditional case of PDT, a photosensitizer is activated by visible light to generate ROS; as described above, this type of light has limitations in tissue penetration. Materials with upconverting properties could be used to activate the photosensitizer directly in the tumor environment. UCNPs excited by NIR light transfer the absorbed energy to photosensitizer molecules and cause the generation of ROS. The most efficient host material for 980 nm upconversion is the hexagonal phase $NaYF_4$, often doped with rare earth ions.

Mostly UCNPs are hydrophobic and their surface modification can provide the improvement of particles' dispersibility in the aqueous biological media. Charged or polar moieties such as amphiphilic (co)polymers, lipids and silica are therefore attached to the particle surface. The silica coating imparts many useful properties to the nanoparticles, including the capability for their additional functionalization and biocompatibility [44]. The implementation of a silica shell is based on its unique properties, including high thermal and chemical stability, optical transparency, and easy control of the coating shell. In addition, the biocompatibility of the SiO_2 shell and its further fictionalization with versatile organic and inorganic compounds are crucial for its biological applications as well as for enabling nanoparticle dispersion in polar and non-polar environments. By coating the $NaYF_4$:Yb,Tm NCs with a uniform SiO_2, the hydrophobic UCNs become water dispersible [45].

The surface modification of the nanoparticles by silica results in an increase in photoluminescence intensity of about 9% compared to the uncoated sample of $NaYF_4$:(Yb^{3+}, Er^{3+}) phosphor. This increase in photoluminescence intensity can be explained by the suppression of non-radiative recombination of electron-hole pairs via surface defects [46].

Furthermore, the use of SiO_2 for the external coating of lanthanide-doped UCNPs is attractive because silica is known to be relatively harmless when used in biological

systems. The nanomaterials are relatively non-toxic even at relatively high concentrations (50 mg/ml) for 48 h incubation in HeLa cells [47]. Also, the dependence of UNPs' cytotoxicity on their coating type was comprehensively considered previously in Ref [48].

Previously, we have demonstrated the possibility of Hep-2 cells labeling with uncoated and coated with SiO_2 shell [$NaYF_4$:Yb^{3+}, Er^{3+}] UCNPs *in vitro* and estimated their phototoxicity [49]. SiO_2-coated nanoparticles were found more toxic under NIR irradiation than uncoated ones and capable of inducing cell apoptosis (pycnosis stage). Also, we found a decrease in the number of cells containing autophagosomes, which can probably point to the blocking of resistance in tumor cells. Uncoated UCNPs did not substantially decrease Hep-2 cells' viability, however, the same effect of autophagy blockage as for covered nanoparticles was found. Therefore, our preliminary data point to the prospective of the elaborated SiO_2-coated UCNPs for application in cancer therapy.

Here, we compared the photocytotoxic effect of [$NaYF_4$:Yb^{3+}, Er^{3+}] UCNPs on human lung-derived embryonic fibroblast (FLEH-104) and human laryngeal epidermoid carcinoma (Hep-2) cell lines under the NIR irradiation. Also, we assessed the effect of both types of nanoparticles in the presence of NIR irradiation on the morphology of normal and cancer cell lines.

2 Experimental Section

2.1 UCNPs Synthesis and Characterization

Uncoated and coated with SiO_2 shell [$NaYF_4$:Yb^{3+}, Er^{3+}] (fluoride matrix doped with ytterbium and erbium ions) UCNPs were synthesized by a hydrothermal method as it was described previously in Ref. [50]. The final UCNP concentration was 10 mg/mL. UCNP images (Fig. 1(a)) obtained using the field-emission scanning electron microscope (SEM)MIRA 2 LMU(TESCAN, Czech) were used for particles morphology and size assessment. The average size of UCNPs was measured using ImageJ software.

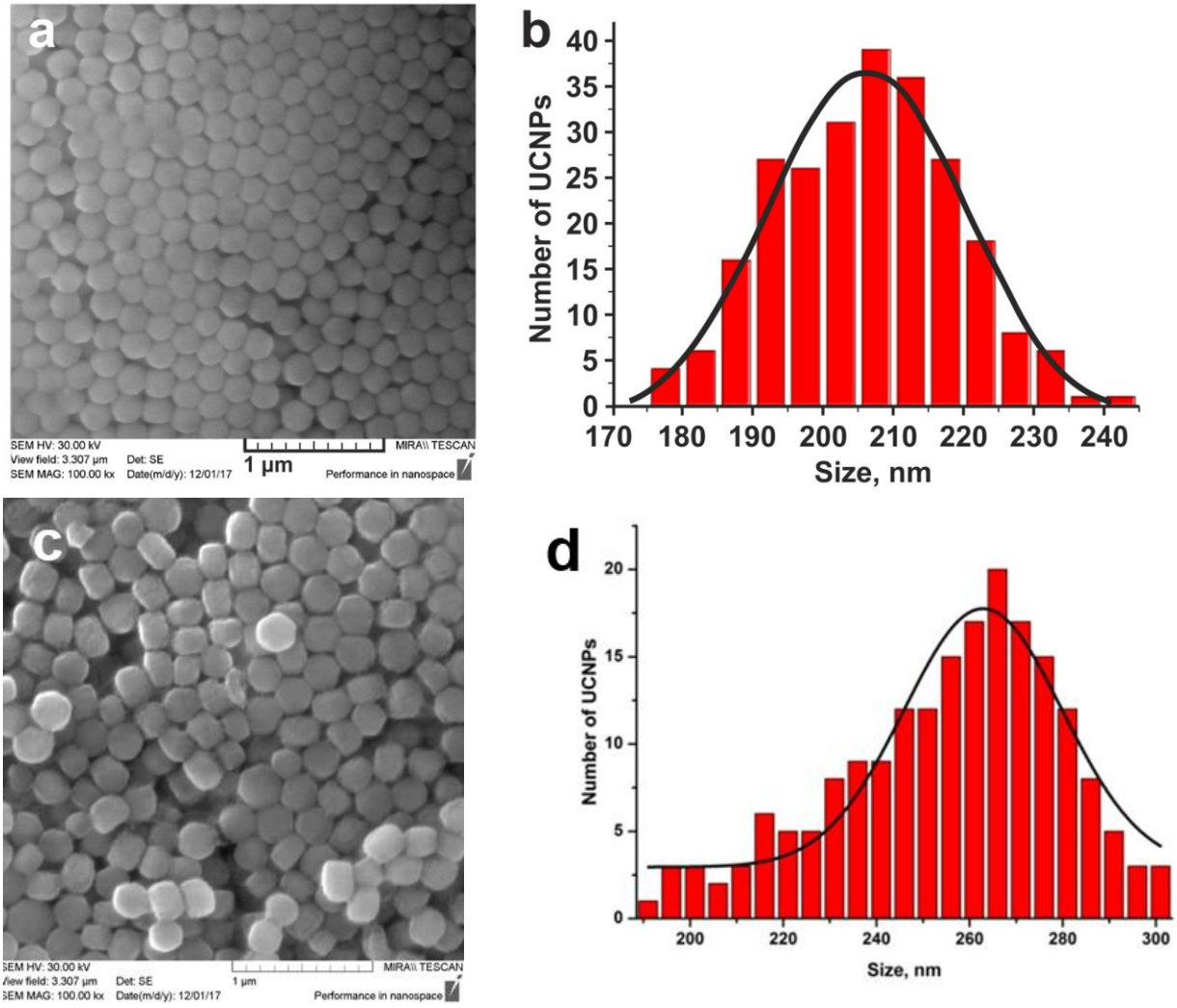


Fig. 1 (a) SEM image of the uncoated [$NaYF_4$:Yb^{3+}, Er^{3+}] UCNPs, (b) size distribution of uncoated UCNPs, (c) SEM image of the coated [$NaYF_4$:Yb^{3+}, Er^{3+}] UCNPs, (d) size distribution of coated UCNP.

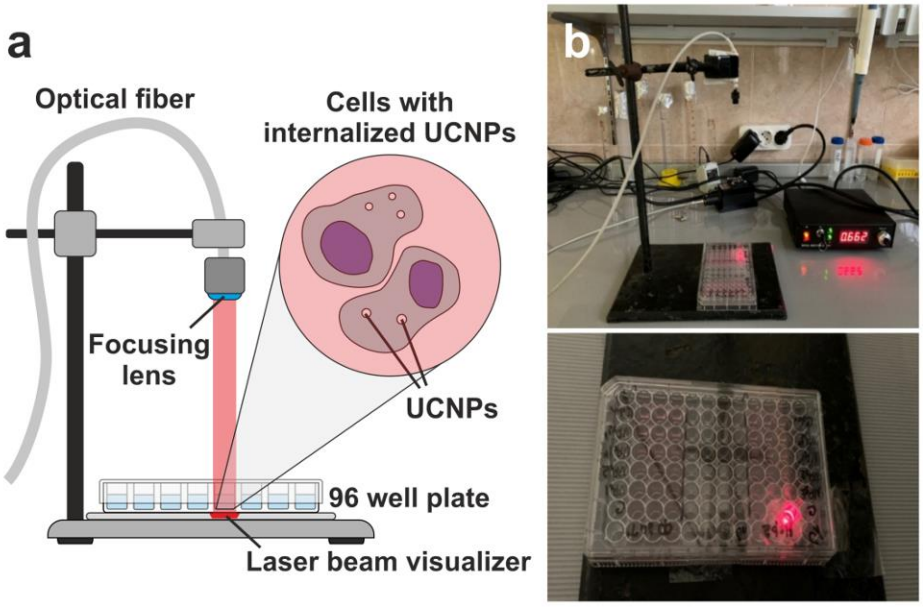


Fig. 2 (a) Scheme of the experimental setup and (b) photos of the setup with the 96 well plate under NIR light exposure.

2.2 Cell Cultures

Hep-2 and FLEH-104 cell lines were provided by the Department of Cell Engineering, Education and Research Institute of Nanostructures and Biosystems, Saratov State University, Russia. All cell lines were plated separately in tissue culture flasks and grown in Dulbecco's Modified Eagle Medium (DMEM) supplemented with 1% penicillin-streptomycin antibiotic antifungal cocktail, 2 mM of L-glutamine, and 10% fetal bovine serum (FBS), in the humidified atmosphere of 5% CO_2 in air at 37 °C. The media were replaced every three days. Cell cultures with 75–85% confluence were harvested using 0.25% trypsin and counted using a Countess automated cell counter (Thermo Fisher Scientific, USA).

2.3 Experimental Procedures

The scheme and photo of the experimental setup used for cells exposure are presented in Fig. 2(a, b). The cells were plated in a 96-well plate with a transparent bottom at 10^4 cells per well density and incubated overnight. After the incubation, uncoated and coated UCNPs were added to cells at a concentration of 10 mg/mL and incubated for 24 h. Then, each well except the control ones was irradiated by the 980 nm light source (0.5 W/cm^2 power density). The cell culture media was replaced by Dulbecco's Phosphate Buffered Saline (DPBS) for the duration of the light exposure. The 980 nm diode laser (laser's power: 108 mW) (LSR980NL-1000, Lasever, China) equipped with 600 μm optic fiber was used for UCNP excitation. The exposure time varied in the range from 5 to 45 min. IR imager IRISYS 4010 (InfraRed Integrated System Ltd, UK) located at a distance of 30 cm from the sample was used for non-contact measurement of the samples' surface temperature. The temperature of the cages did not increase during the experiment. Finally, cell viability was evaluated using resazurin-based Alamar Blue cell viability reagent. For this dye was added to each well at a concentration of 10% v/v and incubated for 4 h. The fluorescence intensity (Ex/Em: 560/590 nm) of the reduced form of dye (resorufin) was measured using the Synergy H1 multimode reader (BioTekInstruments, Inc., USA).

Acridine orange dye was used for the cell morphology assessment. Cells were stained by 400 nM final concentration dye solution for 10 min, then triply washed with PBS and investigated using the inverted IX 73 fluorescent microscope (Olympus America Inc., USA).

3 Results and Discussion

Synthesized [$NaYF_4$:Yb^{3+}, Er^{3+}] UCNPs possessed hexagonal-like shape with the average size 205 ± 10 nm (Fig. 1(a)). The size distribution of synthesized UCNPs is presented in Fig. 1(b). The synthesized particles are characterized by a narrow size distribution, indicating their monodispersity. UCNPs coated with a layer of SiO_2 (Fig. 1(c)) have a wider size distribution due to the heterogeneity of the shell thickness. The size of the coated UCNPs is 262 ± 21 nm.

Cells exposure with NIR light was performed using the setup depicted in Fig. 2(a, b). The laser beam size was adjusted to cover only a single well of the 96-well plate to prevent the overexposure of cells in the adjacent wells by direct laser light. It enabled us to control the exposure time for all experimental groups. The guidance of the NIR laser spot on the well center was performed using the laser beam visualizer fixed under the bottom of the transparent 96-well plate.

The assessment of the metabolic activity of model cell lines after their 24 h co-incubation with elaborated uncoated/coated UCNPs without NIR exposure did not reveal a statistically significant decrease in cell viability.

The irradiation of cells after the period of co-incubation with all types of particles, in turn, negatively affected the cell viability (Fig. 3). So, an increase in the irradiation duration resulted in the mitigation of cell viability. Also, we found that the susceptibility of the Hep-2 cell line to the uncoated/coated UCNPs action under the NIR exposure was lower than for FLEH-104. The probable reason for this is the difference in cell line morphology. Fibroblasts are characterized by larger surface area if compared with epidermoid carcinoma cells. Therefore, the probability of malignant cell interaction with added uncoated/coated UCNPs is lower if compared with such for fibroblasts, which may be a reason for lower particle internalization efficiency. The laser irradiation dose obtained for 5 min did not induce a decrease in cells' metabolic activity for both cell lines, while the cells' irradiation for 10 min caused a statistically significant decrease in their viability.

Fig. 4 shows images of Hep-2 and FLEH-104 cell cultures after different types of exposure under fluorescence microscopy, where living cells were stained with acridine orange. Autophagy and apoptosis are observed in some cases.

In control samples of Hep-2, cells form contacts and connections. The cells are round or polygonal. They vary widely in size. The nucleus is rounded. Nucleoli are present. Mitotic figures are present. There are no signs of apoptosis and individual autophagosomes are seen in the cytoplasm (Fig. 4(a)). When uncoated with SiO_2 shell UCNPs are added to the cells, a decrease in cell density is observed. However, the cells remain in contact.

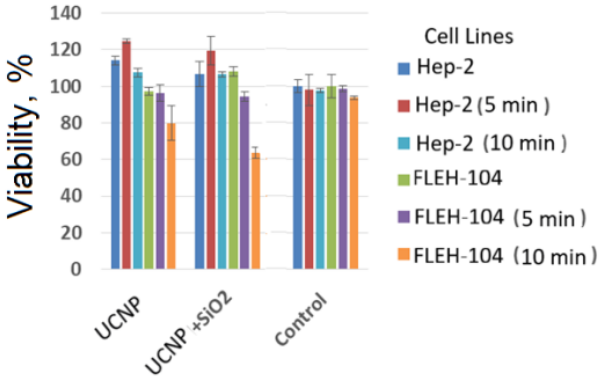


Fig. 3 The viability of Hep-2 and FLEH-104 cell lines after 24 h of incubation with uncoated/coated UCNPs at 10 mg/mL particle concentration, depending on the particles' type and the exposure time (5 and 10 min).

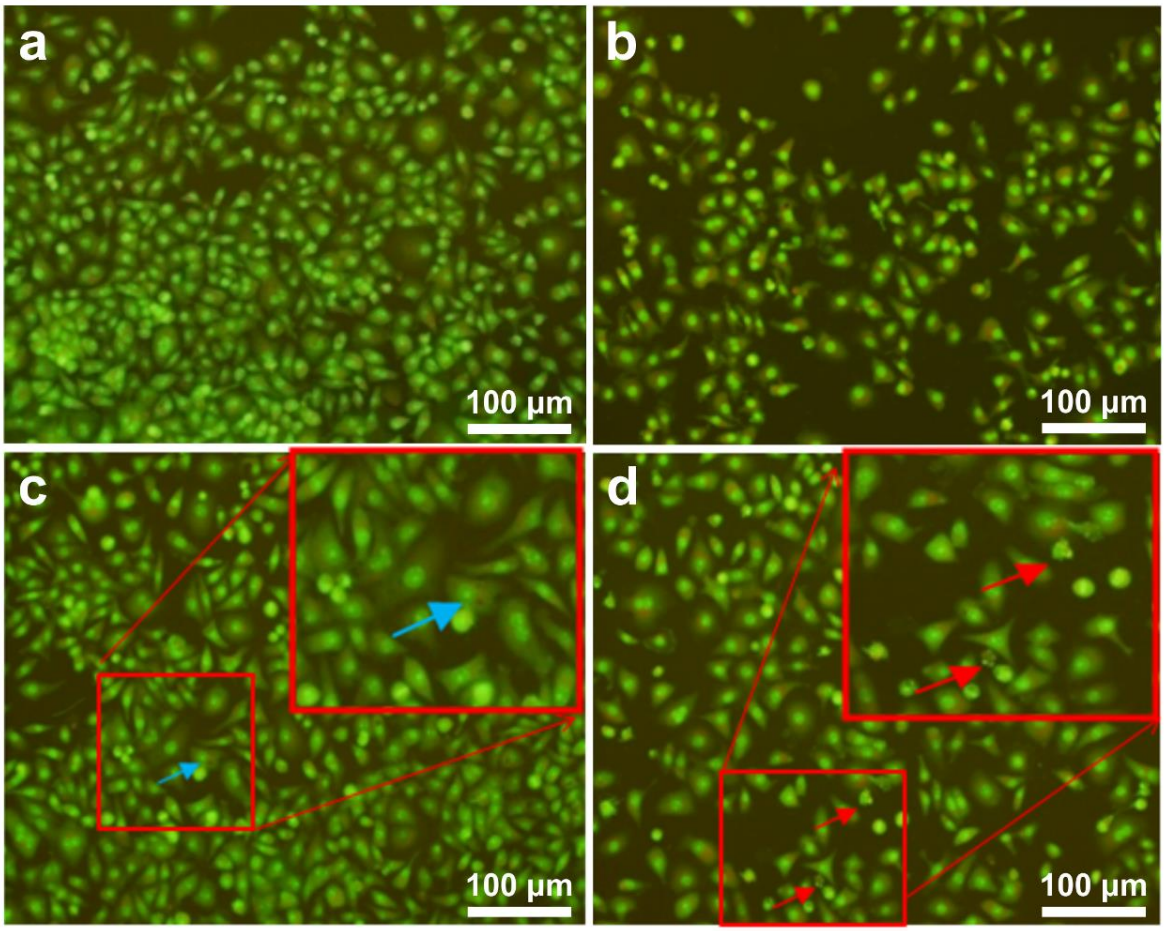


Fig. 4 Fluorescent images of Hep-2 cells stained with acridine orange: (a) control − cells incubated in the absence of uncoated with SiO_2 shell UCNPs, (b−d) cells incubated with uncoated UCNPs for 24 h and exposed by NIR-irradiation for (b) 5 min, (c) 15 min, and (d) 45 min. Cells containing autophagosomes are marked by the blue arrows; apoptotic cells are indicated by red arrows.

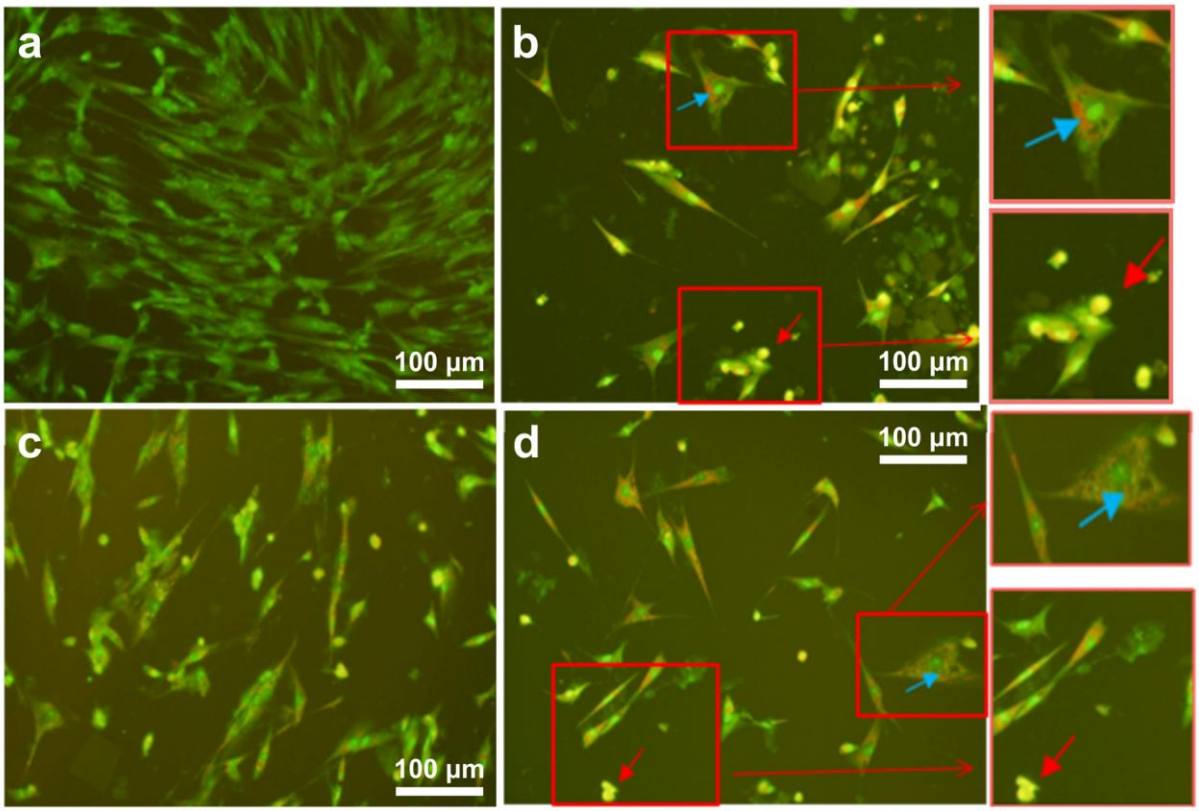


Fig. 5 Fluorescent images of FLEH-104 cells stained with acridine orange: (a) control − cells incubated in the absence of uncoated with SiO_2 shell UCNPs, (b−d) cells incubated with uncoated UCNPs for 24 h and exposed by NIR-irradiation for (b) 5 min, (c) 15 min, and (d) 45 min. Cells containing autophagosomes are marked by the blue arrows; apoptotic cells are indicated by red arrows.

A single pycnosis of the nuclei is observed. Apoptotic bodies are also detected. And in some cells there are single microautophages. The cell density is greatly reduced when irradiated for 5 min. Cells are more scattered. All nuclei are pyknotic and condensed. Many lysosomes appear, but autophagosomes are absent. However, despite the pronounced pycnosis, there are figures of mitosis, activation of proliferative activity, which explains the higher survival rate of this culture according to the previous test at 5 minutes of irradiation (Fig. 4(b)). After 15 min of irradiation, the cells maintained their contacts. Individual pycnosis and microautophagosomes, mitotic figures are present (Fig. 4(c)). At 30 min irradiation, pycnosis was observed with disappearance of cell cytoplasm, which is a morphological sign of the initial stage of apoptosis. At 45 min of irradiation, the cell density is greatly reduced. Cells are more elongated. Nuclei are hyperchromic and condensed. Many lysosomes and individual microautophagosomes appear. Nuclear pycnosis with disappearance of cytoplasm and apoptotic bodies were observed (Fig. 4(d)). After 60 min of irradiation, the cell density is reduced. Cells are more elongated. The nuclei are small, hyperchromic and condensed. Pycnosis of nuclei was registered - a sign of apoptosis. There are no autophagosomes in the cells.

In the control FLEH-104 cells, the cells form multiple contacts and connections, are sharply elongated, the nucleus is not expressed, the nucleoli are present. There are no signs of apoptosis and autophagy (Fig. 5(a)). When uncoated with SiO_2 shell UCNPs are added to the cells, a decrease in cellular activity is observed, but the cells retain contacts, a single pycnosis, increased granularity in the cells, and microautophages are observed. The viability of the fibroblasts was not affected by uncoated UCNPs. The data obtained are consistent with the results of the authors who showed that the use of particles in concentrations of 62.5−125 μg/mL does not lead to a violation of fibroblast viability [51]. After irradiation for 5 min, the cellular activity is greatly reduced, the cells are more elongated, the nuclei are hyperchromic, condensed, many lysosomes appear, there is cellular debris (remnants of destroyed cells). Morphological signs of autophagosomes (appearance of vacuoles surrounded by lysosomes) are present in cell cultures. Pycnosis of nuclei was registered − possibly apoptosis (Fig. 5(b)). At 15 min of irradiation, the cell activity of the culture is reduced, but the cells maintain contacts, there is a single pycnosis and microautophages, and the granularity in the cells is increased (Fig. 5(c)). After 30 min of irradiation, pycnosis predominates and signs of apoptosis are possible. At 45 min irradiation, cellular activity is greatly reduced, cells are more elongated, nuclei are hyperchromic and condensed, many lysosomes appear, cellular debris and autophagosomes are present. Pycnosis of nuclei was registered - signs of apoptosis are possible (Fig. 5(d)). After 60 min of irradiation, the activity of the cells is greatly reduced, the

cells are more elongated, the nuclei are hyperchromic and condensed, there are many lysosomes and autophagosomes, and there is cellular debris. Pycnosis of nuclei was registered − signs of apoptosis are possible.

4 Conclusion

UCNPs have been approved as a promising material for cancer diagnostics and treatment. Here we demonstrated the capability of [$NaYF_4$:Yb^{3+}, Er^{3+}] UCNPs to induce cell death through apoptosis under the NIR irradiation. The irradiation of cells, preliminary co-incubated with elaborated UCNPs (10 mg/mL) for 24 h, by 980 nm laser (power density: 0.5 W/cm^2) for 10 min was found sufficient to significantly decrease the viability of both model cell lines. The phototoxic effect of UCNPs on the fibroblast cell line was more pronounced than on the epidermoid carcinoma cells, possibly due to differences in particle internalization efficiency by these cell lines.

It has been shown the photocytotoxic and morphological comparison of FLEH-104 and Hep-2 cell lines responses to influence of uncoated and coated by SiO_2 shell UCNPs.

Cell viability is assessed for cytotoxic effects of UCNPs at light exposure (to demonstrate the direct phototoxic effects).

The addition of UCNPs has a negative effect on FLEH-104. This result may be due to the fact that fibroblasts have a different morphology (they are larger and elongated) than Hep-2, as a consequence their cell surface area is larger and when particles are added, they capture a greater amount. This means that after 5 min no toxic effect is observed, but after 10 min the fibroblasts begin to die (this number of UCNPs and the duration of exposure are sufficient to heat the cell and cause its death).

Morphological signs of autophagy (appearance of vacuoles surrounded by lysosomes) and apoptosis (pronounced pycnosis of the nucleus) are observed in some cases during irradiation of Hep-2 and FLEH-104 cells.

The results confirm the high activity of luminescent-uncoated UCNPs against Hep-2 cancer cells and show potential for theranostics, i.e. imaging and controlled thermal effects on pathological cells. The particles exhibited cytotoxic, cytostatic properties. By activating the photodynamic reaction in tumor cells, apoptosis is induced and tumor cell resistance is prevented by extending the irradiation time to 60 min by blocking autophagy. At the same time, maximum laser irradiation of FLEH-104 culture treated with luminescent coating UCNPs induces not only apoptosis but also autophagy, indicating that normal cells are less sensitive to the action of the particles. This makes these types of nanoparticles the most promising to study in experimental oncology. Thus, UCNPs are a promising alternative to conventional fluorescent labels for cell imaging and have great potential in biological and clinical applications.

Acknowledgements

The study was supported by a grant Russian Science Foundation No. 21-72-10057, https://rscf.ru/project/21-72-10057/.

Disclosures

All authors declare that there is no conflict of interests in this paper.

References

1. J. Ferlay, M. Colombet, I. Soerjomataram, D. M. Parkin, M. Piñeros, A. Znaor, and F. Bray, "Cancer statistics for the year 2020: An overview," International Journal of Cancer 149(4), 778−789 (2021).
2. Cancer, World Health Organization (accessed 15 September 2022). [https://www.who.int/news-room/fact-sheets/detail/cancer].
3. J. G. Hiller, N. J. Perry, G.Poulogiannis, B. Riedel, and E. K. Sloan,"Perioperative events influence cancer recurrence risk after surgery," Nature Reviews Clinical Oncology 15(4), 205−218 (2018).
4. Y. P. Liu, C. C. Zheng, Y. N. Huang, M. L. He, W. W. Xu, and B. Li, "Molecular mechanisms of chemo- and radiotherapy resistance and the potential implications for cancer treatment," MedComm 2(3), 315−340 (2021).
5. Y. Wu, Y. Song, R. Wang, and T. Wang, "Molecular mechanisms of tumor resistance to radiotherapy," Molecular Cancer 22(1), 96 (2023).
6. N. V. Polukonova, M. A. Baryshnikova, D. A. Khochankov, E. V. Stepanova, E. S. Solomko, A. V. Polukonova, D. A. Mudrak, A. M. Mylnikov, A. B. Bucharskaya, G. N. Maslyakova, and N. A. Navolokin, "Activation of Apoptosis and Autophagy by Gratiola Officinalis Extract in Human Tumor Cell Lines," Journal of Biomedical Photonics & Engineering 7(4), 040307 (2021).
7. H. Modjtahedi, S. Ali, and S. Essapen,"Therapeutic application of monoclonal antibodies in cancer: advances and challenges," British Medical Bulletin 104, 41−59 (2012).
8. V. M. Tolmachev, V. I. Chernov, and S. M. Deyev, "Targeted nuclear medicine. Seek and destroy," Russian Chemical Reviews 91(3), RCR5034 (2022).
9. N. Widmer, C. Bardin, E. Chatelut, A. Paci, J. Beijnen, D. Levêque, G. Veal, and A. Astier, "Review of therapeutic drug monitoring of anticancer drugs part two – Targeted therapies," European Journal of Cancer 50(12), 2020−2036 (2014).

10. E. Raschi, V. Vasina, M. G. Ursino, G. Boriani, A. Martoni, and F. De Ponti, "Anticancer drugs and cardiotoxicity: Insights and perspectives in the era of targeted therapy," Pharmacology & Therapeutics 125(2), 196−218 (2010).
11. T. A. Baudino, "Targeted Cancer Therapy: The Next Generation of Cancer Treatment," Current Drug Discovery Technologies 12(1), 3−20 (2015).
12. M. Kim, D. M. Kim, K. S. Kim, W. Jung, and D. E. Kim, "Applications of Cancer Cell-Specific Aptamers in Targeted Delivery of Anticancer Therapeutic Agents," Molecules 23(4), 830 (2018).
13. H. Sun, X. Zhu, P. Y. Lu, R. R. Rosato, W. Tan, and Y. Zu, "Oligonucleotide aptamers: new tools for targeted cancer therapy," Molecular Therapy-Nucleic Acids 3(8), e182 (2014).
14. M. C. Skala, J. M. Squirrell, K. M. Vrotsos, J. C. Eickhoff, A. Gendron-Fitzpatrick, K. W. Eliceiri, and N. Ramanujam, "Multiphoton microscopy of endogenous fluorescence differentiates normal, precancerous, and cancerous squamous epithelial tissues," Cancer Research 65(4), 1180−1186 (2005).
15. S. Maryam, M. S. Nogueira, R. Gautam, S. Krishnamoorthy, S. K. V. Sekar, K. W. Kho, H. Lu, R. N. Riordain, L. Feeley, P. Sheahan, R. Burke, and S. Andersson-Engels, "Label-Free Optical Spectroscopy for Early Detection of Oral Cancer," Diagnostics 12(12), 2896 (2022).
16. L. Yang, J. Park, M. Marjanovic, E. J. Chaney, D. R. Spillman Jr, H. Phillips, and S. A. Boppart, "Intraoperative Label-Free Multimodal Nonlinear Optical Imaging for Point-of-Procedure Cancer Diagnostics," IEEE Journal of Selected Topics in Quantum Electronics 27(4), 1−12 (2021).
17. S. Hernot, L. van Manen, P. Debie, J. S. D. Mieog, and A. L. Vahrmeijer, "Latest developments in molecular tracers for fluorescence image-guided cancer surgery," Lancet Oncology 20(7), e354-e367 (2019).
18. D. Musumeci, C. Platella, C. Riccardi, F. Moccia, and D. Montesarchio, "Fluorescence Sensing Using DNA Aptamers in Cancer Research and Clinical Diagnostics," Cancers 9(12), 174 (2017).
19. M. Gao, F. Yu, C. Lv, J. Choo, and L. Chen, "Fluorescent chemical probes for accurate tumor diagnosis and targeting therapy," Chemical Society Reviews 46(8), 2237−2271 (2017).
20. V. Shupletsov, K. Kandurova, V. Dremin, E. Potapova, M. Apanaykin, U. Legchenko, and A. Dunaev, "Fluorescence imaging system for biological tissues diagnosis: phantom and animal studies," Journal of Biomedical Photonics & Engineering 6(1), 010303 (2020).
21. V. Maryakhina, Y. Korneva, I. Chekurov, and O. Shisterova, "Fluorescent diagnostics of benign breast diseases and breast cancer," Journal of Biomedical Photonics & Engineering 3(4), 040306 (2017).
22. A. D. Mironova, Y. V. Kargina, Olga S. Pavlova, A. M. Perepukhov, I. O. Sobina, and V. Yu. Timoshenko, "Porous Silicon Nanoparticles with Rare Earth as Potential Contrast Agents for MRI and Luminescent Probes for Bioimaging," Journal of Biomedical Photonics & Engineering 8(2), 020304 (2022).
23. M. Albota, D. Beljonne, J. L. Brédas, J. E. Ehrlich, J.-Y. Fu, A. A. Heikal, S. E. Hess, T. Kogej, M. D. Levin, S. R. Marder, D. Mccord-Maughon, J. W. Perry, H. RöCkel, M. Rumi, G. Subramaniam, W. W. Webb, X.-L. Wu, and C. Xu, "Design of organic molecules with large two-photon absorption cross sections," Science 281(5383), 1653−1656 (1998).
24. D. R. Larson, W. R. Zipfel, R. M. Williams, S. W. Clark, M. P. Bruchez, F. W. Wise, and W. W. Webb, "Water-soluble quantum dots for multiphoton fluorescence imaging in vivo," Science 300(5624), 1434−1436 (2003).
25. R. A. Farrer, F. L. Butterfield, V. W. Chen, and J. T. Fourkas, "Highly efficient multiphoton-absorption-induced luminescence from gold nanoparticles," Nano Letters 5(6), 1139−1142 (2005).
26. C. Sönnichsen, A. P. Alivisatos, "Gold nanorods as novel nonbleaching plasmon-based orientation sensors for polarized single-particle microscopy," Nano Letters 5(2), 301−304 (2005).
27. H. Wang, T. B. Huff, D. A. Zweifel, W. He, P. S. Low, A. Wei, and J. X. Cheng, "In vitro and in vivo two-photon luminescence imaging of single gold nanorods," Proceedings of the National Academy of Sciences 102(44), 15752−15756 (2005).
28. D. Yelin, D. Oron, S. Thiberge, E. Moses, and Y. Silberberg, "Multiphoton plasmon-resonance microscopy," Optics Express 11(12), 1385−1391 (2003).
29. W. R. Zipfel, R. M. Williams, and W. W. Webb, "Nonlinear magic: multiphoton microscopy in the biosciences," Nature Biotechnology 21(11), 1369−1377 (2003).
30. B. Gidwani, V. Sahu, S. S. Shukla, R. Pandey, V. Joshi, V. K. Jain, and A. Vyas, "Quantum dots: Prospectives, toxicity, advances and applications," Journal of Drug Delivery Science and Technology 61, 102308 (2021).
31. M. J. Abrams, B. A. Murrer, "Metal compounds in therapy and diagnosis," Science 261(5122), 725−730 (1993).
32. Q. Fan, X. Cui, H. Guo, Y. Xu, G. Zhang, and B. Peng, "Application of rare earth-doped nanoparticles in biological imaging and tumor treatment," Journal of Biomaterials Applications 35(2), 237−263 (2020).
33. N. Zhou, J. Ni, and R. He, "Advances of Upconversion Nanoparticles for Molecular Imaging," Nano Biomedicine & Engineering 5(3), 131 (2013).
34. S. A. Hilderbrand, F. Shao, C. Salthouse, U. Mahmood, and R. Weissleder, "Upconverting luminescent nanomaterials: application to in vivo bioimaging," Chemical Communications (28), 4188−4190 (2009).
35. S. Andersson-Engels, H. Liu, C. T. Xu, P. Svenmarker, A. Gisselsson, P. Kjellman, L. Andersson, R. in't Zandt, F. Olsson, and S. Fredriksson, "In vivo luminescence imaging and tomography using upconverting nanoparticles as contrast agents," In 2012 Asia Communications and Photonics Conference (ACP), AS3E.2 (2012).

36. M. A. Syroeshkin, F. Kuriakose, E. A. Saverina, V. A. Timofeeva, M. P. Egorov, and I. V. Alabugin, "Upconversion of Reductants," Angewandte Chemie International Edition 58(17), 5532−5550 (2019).
37. S. Han, R. Deng, X. Xie, and X. Liu, "Enhancing luminescence in lanthanide-doped upconversion nanoparticles," Angewandte Chemie International Edition 53(44), 11702−11715 (2014).
38. P. P. Nampi, A. Vakurov, L. E. Mackenzie, N. S. Scrutton, P. A. Millner, G. Jose, and S. Saha, "Selective cellular imaging with lanthanide-based upconversion nanoparticles," Journal of Biophotonics 12, e201800256 (2019).
39. H. Li, Q. Chen, J. Zhao, and K. Urmila, "Fabricating upconversion fluorescent nanoparticles modified substrate for dynamical control of cancer cells and pathogenic bacteria," Journal of Biophotonics 10(8), 1034−1042 (2017).
40. A. K. S. Braz, D. S. Moura, A. S. L. Gomes, T. Y. Ohulchanskyy, G. Chen, M. Liu, J. Damasco, R. E. de Araujo, and P. N. Prasad, "TiO2 -coated fluoride nanoparticles for dental multimodal optical imaging," Journal of Biophotonics 11(4), e201700029 (2018).
41. Y. Yang, T. Zhang, and D. Xing, "Single 808 nm near-infrared-triggered multifunctional upconverting phototheranostic nanocomposite for imaging-guided high-efficiency treatment of tumors," Journal of Biophotonics 14 (9), e202100134 (2021).
42. Y. Hu, J. F. Honek, B. C. Wilson, and Q-B. Lu, "Design, synthesis and photocytotoxicity of upconversion nanoparticles: Potential applications for near-infrared photodynamic and photothermal therapy," Journal of Biophotonics 12, e201900129 (2019).
43. R. Liang, M. Wei, D. G. Evans, and X. Duan, "Inorganic nanomaterials for bioimaging, targeted drug delivery and therapeutics," Chemical Communications 50(91), 14071 (2014).
44. U. Kostiv, M. Šlouf, H. Macková, A. Zhigunov, H. Engstová, K. Smolková, P. Ježek, and D. Horák, "Silica-coated upconversion lanthanide nanoparticles: The influence of crystal design on morphology, structure and optical properties," Beilstein Journal of Nanotechnology 6, 2290−2299 (2015).
45. M. Tou, Z. Luo, S. Bai, F. Liu, Q. Chai, S. Li, and Z. Li, "Sequentially coating upconversion NaYF4:Yb,Tm nanocrystals with SiO2 and ZnO layers for NIR-driven photocatalytic and antibacterial applications," Materials Science and Engineering: C 70, 1141−1148 (2017).
46. T. Jang, M. J. Kim, and S. H. Sohn, "Silica nanoparticle coating of NaYF4:(Yb3+, Er3+) upconversion phosphor," Journal of Nanomaterials 2022, 8961362 (2022).
47. P. Kowalik, D. Elbaum, J. Mikulski, et al., "Upconversion fluorescence imaging of HeLa cells using ROS-generating SiO2-coated lanthanide-doped NaYF4nanoconstructs," RSC Advances 7(48), 30262−30273 (2017).
48. R. A. Verkhovskii, R. A. Anisimov, M. V. Lomova, D. K. Tuchina, E. N. Lazareva, A. A. Doronkina, A. M. Mylnikov, N. A. Navolokin, V. I. Kochubey, and I. Yu. Yanina, "Cytotoxicity of various types of coated upconversion nanoparticles. Overview," Izvestiya of Saratov University. Physics 22(4), 357–373 (2022). [in Russian].
49. I. Yu. Yanina, E. A. Sagaidachnaya, I. V. Vidyasheva, N. A. Navolokin, V. I. Kochubey, and V. V. Tuchin, "Phototoxicity and luminescence of the upconversion nanoparticles embedded in the cells," Proceedings of SPIE 10877, 108770Y (2019).
50. E. A. Sagaidachnaya, J. G. Konyukhova, N. I. Kazadaeva, A. A. Doronkina, I. Yu. Yanina, A. A. Skaptsov, A. B. Pravdin, and V. I. Kochubey, "Effect of hydrothermal synthesis conditions on up-conversion luminescence intensity of β-NaYF4 : Er3+, Yb3+ particles," Quantum Electronics 50(2), 109–113 (2020).
51. A. E. Guller, A. N. Generalova, E. V. Petersen, A. V. Nechaev, I. A. Trusova, N. N. Landyshev, A. Nadort, E. A. Grebenik, S. M. Deyev, A. B. Shekhter, and A. V. Zvyagin, "Cytotoxicity and non-specific cellular uptake of bare and surface-modified upconversion nanoparticles in human skin cells," Nano Research 8, 1546−1562 (2015).